To the Graduate Council:

I am submitting herewith a thesis written by Hernán R. Menéndez-Fernández entitled "Determination of Fiber Orientation of Composites Using Wide Angle X-Ray Diffraction." I have examined the final copy of this thesis for form and content and recommend that it be accepted in partial fulfillment of the requirements for the degree of Master of Science, with a major in Polymer Engineering.

James L. White, Major Professor

We have read this thesis and recommend its acceptance:

Donald C. Bogue

J. E. Spruiell

Edward S. Clark

Accepted for the Council:

L. Evans Haak
Vice Chancellor
Graduate Studies and Research

DETERMINATION OF FIBER ORIENTATION OF COMPOSITES USING WIDE ANGLE X-RAY DIFFRACTION

A Thesis

Presented for the

Master of Science

Degree

The University of Tennessee, Knoxville

Hernán R. Menéndez-Fernández

December 1982

DEDICATION

This work is dedicated to my parents, Hernán and Maricela, who have always given me love, support and guidance.

It is also dedicated to my sister Nora and my brother Ruy, who have encouraged me to look for new horizons without reserve.

Finally, and very specially, it is dedicated to my wife Anita, who shared the hard times and gave me love and understanding.

ACKNOWLEDGMENTS

The author is very indebted to Professor James L. White for his guidance and encouragement during the course of this research.

Appreciation is extended to Professor Joseph E. Spruiell for his helpful comments and suggestions regarding x-ray diffraction procedures.

Appreciation is also extended to Mukerrem Cakmak for many enlightening discussions during the long hours in the laboratory.

Financial support was provided by the National Science Foundation and by a Teaching Assistantship in the Department of Chemical, Metallurgical and Polymer Engineering.

Appreciation is expressed to E. I. du Pont de Nemours and Company and to Rohm and Haas Company for supplying the materials used in this research.

ABSTRACT

Studies of both rheological properties and fiber orientation development due to flow of short fiber filled thermoplastic systems are described. These composite systems are mechanical mixtures of an amorphous polymethylmethacrylate (PMMA) matrix with short crystalline aramid (Kevlar 49) reinforcing fibers in a proportion 80/20 in volume. Rheological measurements only cover the shear viscosity (η) in the high shear rate range due to flow instabilities and experimental difficulties which did not permit carrying out any other rheological measurements. Fiber orientation development due to flow was investigated in systems having different fiber aspect ration. Qualitative studies involved the use of x-ray flat-film techniques and scanning electron microscopy (SEM). Quantitative evaluations of fiber orientation as represented by Herman-Stein orientation functions were carried out in extrudate and frozen in situ specimens by means of a wide angle x-ray technique proposed in this research.

Addition of aramid fibers increases the viscosity but does not affect the basic character of the viscosity shear rate behavior of the polymer melt. A little change in viscosity is observed with fiber length at high rates of deformation, but a significant increase can be expected at low shear rates with longer fiber length distributions.

Pressure effects observed in the system filled with fibers having a modal length larger than the diameter of the capillaries used in its characterization are associated with this fact.

Studies of fiber orientation carried out in composite specimens prepared by capillary extrusion using the proposed x-ray technique showed that the orientation function values obtained are dependent in both shear rate and die swell at constant processing geometry. Analysis of composite specimens from material frozen inside the rheometer barrel and the capillary die showed that the fiber orientation development took place along the capillary die and was greatly affected by the die swell effect in the extrudate. Reduced die swell effects were observed in all composite samples as compared to that observed in the unfilled melt.

TABLE OF CONTENTS

CHAPTER PAGE

LIST OF TABLES

LIST OF FIGURES

FIGURE PAGE

CHAPTER I

INTRODUCTION

Reinforced thermoplastics constitute an active sector of the thermoplastic industry, growing in importance both commercially and technically. The addition of reinforcing short fibers to thermoplastic polymers has produced a distinct type of engineering materials which may be processed by conventional and economic methods such as injection molding and extrusion. These materials exhibit improved mechanical properties relative to those of the unfilled thermoplastics.

It is well known that mechanical properties depend strongly on the processing history and on several parameters such as fiber length and content, fiber orientation and geometry, fiber-matrix adhesion, and the properties of the matrix. Fiber aspect ratio and orientation are influenced very strongly by the compounding and processing methods.

Besides the complex patterns of orientation that fibers can adopt during processing, their presence in the molten polymer has a great influence on both the rheological properties of the melt and its processability.

Although much well founded practical knowledge is available on the production, mechanical properties and application of reinforced thermoplastics, there is as yet

no unified basic theory of the structure and properties of these materials. The considerable volume of available fundamental information still represents a rather fragmented picture containing areas which are still rather diffuse.

Most of the studies concerning fiber orientation development in the flow of polymer melts emphasize experimental methods and the data obtained are generally qualitative.

It is the purpose of this thesis to quantitatively study the flow induced orientation of short reinforcing fibers suspended in a polymer melt as a result of processing conditions and geometry. Developed is a quantitative method of evaluation of fiber orientation in the solid reinforced material which is based upon the use of wide angle x-ray diffraction (WAXS) techniques.

CHAPTER II

BACKGROUND AND LITERATURE SEARCH

A. FIBER REINFORCED THERMOPLASTICS

General

In a thermoplastic composite material, the reinforcing fibers are dispersed in a polymer matrix. The latter is of low strength, fairly tough and extensible, of lower density and higher coefficient of thermal expansion as compared with the reinforcing fibers which are generally strong, stiff and brittle. Therefore, it is the reinforcing material which should, ideally, bear as much as possible of any load or stress applied to the composite, while the polymer matrix should efficiently transmit the load to the reinforcing fibers.

Glass fibers are the most common reinforcing material in thermoplastic composites. However, this kind of composite has a number of disadvantages. Glass fibers, as a reinforcement, have high density, show low adhesion to the polymer matrix, and degrade to small aspect ratios during compounding. Besides, glass reinforced thermoplastics produce considerable abrasive wear during their processing and mechanical working, and the associated embrittlement of the material, especially if the polymeric matrix is ductile, often limits the application of these composites. Work has

been done in order to understand the mechanism and parameters governing the impact strength of glass reinforced thermoplastics (94) and to evaluate the material and the development of design procedures (104).

Work on reinforcing thermoplastics with synthetic polymer fibers has produced encouraging results (59). While synthetic fibers such as cellulose (e.g., Monsanto Santoweb) and nylon prove adequate for elastometers because of the same low modulus, only Kevlar aramid fibers have a high enough modulus for glassy and crystalline thermoplastic matrices.

Synthetic polymer fibers show many advantages over glass ones as a reinforcing material. They ensure excellent wettability of the fiber surface with respect to the polymer and yield high fiber-matrix adhesion. Also, synthetic fibers are more elastic, show a greater resistance to abrasion without being abrasive to the processing equipment, and have less tendency to break down to lower aspect ratios during processing (113).

Elastic Properties

Theoretical analysis of the composite system becomes complicated because fiber length and ratio become factors, as well as fiber orientation effects. The latter in particular can give rise to anisotropy of properties in the composite. The simplest theoretical approach is based on a simple law of mixtures (58) which yields a relationship

valid for an elastic matrix reinforced by a uniaxially aligned continuous fiber and tested in the direction of orientation as follows:

$$E_c = E_f\phi_f + E_m(1 - \phi_f) \qquad [II\text{-}1]$$

where E_c, E_m and E_f = moduli of, respectively, the composite, matrix polymer and reinforcing fibers. In the case of misaligned fibers or any difference between the direction of testing and the fiber axis, the given equation is modified by introducing alignment factors.

Theories of the elastic modulus of composites containing oriented fibers have been the object of several studies. Generally, one writes

$$\sigma_{ij} = \sum_{k}\sum_{l} G_{ijkl}\,\varepsilon_{kl} \qquad [II\text{-}2]$$

where σ_{ij} represents the stress components; ε_{kl}, the strain components; and G_{ijkl}, the components of the modulus tensor. Brody and Ward (8) have proposed a theoretical model for calculating the elastic moduli G_{ijkl} of a partially oriented short fiber reinforced composite. In this model, it is assumed that the composite consists of an aggregate of sub-units, each sub-unit possessing the elastic properties of a reinforced composite in which the fibers are continuous and fully aligned. The elastic moduli of the composite can be calculated from those of the sub-units by either of two averaging procedures. The Reuss average assumes uniform

stress and consists of averaging the compliance constants for a partially oriented composite (112). The Voigt average assumes uniform strain and is obtained from the corresponding equations for the stiffness constants (112). In both cases, the elastic constants of the composite are given as a function of both the elastic constants of the sub-units and the fourth-moment orientation functions defined by the following equations:

$$I_1 = \overline{\sin^4\theta} \qquad \text{[II-3a]}$$

$$I_2 = \overline{\cos^4\theta} \qquad \text{[II-3b]}$$

$$I_3 = \overline{\sin^2\theta \cos^2\theta} \qquad \text{[II-3c]}$$

$$I_4 = \overline{\sin^2\theta} \qquad \text{[II-3d]}$$

$$I_5 = \overline{\cos^2\theta} \qquad \text{[II-3e]}$$

where θ is the angle between the symmetry axis of the sub-unit and the symmetry axis of the composite. The values of these orientation functions can be determined in terms of the draw ratio for a partially oriented composite.

Moghe (77) has developed a simple mathematical model to predict the directional properties of elastomers mixed with uniaxially oriented short fibers. The model is based upon describing a distribution function for the fibers and then the composite properties. The distribution function depends upon a single parameter which is called the

orientation strain. The proposed theory is showed to be in good agreement with the experimental results regarding the directional modulus of short fiber reinforced composites.

Coran et al. (20) have studied the mechanical behavior of short fiber elastomer composites. They found that the measured elastic and strength properties of angle-ply laminates of short fibers and rubber depend on test piece geometry. Once the effects of test piece geometry are taken into account, elastic properties can be calculated as functions of the properties of a single ply. The influence of matrix orientation in composites is described by Patel and Bogue (90).

Ultimate Behavior

Considering the simplest case of an elastic matrix reinforced by a uniaxially aligned continuous fiber, the ultimate tensile strength in the direction of the fibers is also given by a simple law of mixtures (58) as shown in Equation II-4

$$\sigma_{uc} = \sigma_{uf}\,\phi_f \quad \sigma_m'(1 - \phi_f) \qquad [II\text{-}4]$$

where σ_{uc}, σ_{uf} = ultimate strength of the composite and the reinforcing fiber, respectively; σ_m' = stress in matrix at fiber failure strain; ε_{mc} = the ultimate stress of the composite; and ϕ_f = the volume fraction of the fiber. As in the case of Equation II-1, alignment factors are also introduced in Equation II-4 to account for fiber

misalignment or differences between the direction of testing and the fiber axis.

The above approach has been extended to include the case of discontinuous reinforcing fibers of finite length (16, 26). If the fibers are discontinuous, then the fiber may carry stress only by a shear transfer process at the interface, and both the actual fiber length and interfacial adhesion between fiber and matrix become important parameters.

Chen (16) has derived a formula for calculating the strength of randomly oriented discontinuous fiber composites given by:

$$\sigma_\theta = \frac{2\tau_m}{\pi} \left(2 + \ln \frac{\xi \sigma_c' \sigma_m}{\tau_m}\right) \qquad [II\text{-}5]$$

where σ_θ = strength of the randomly-oriented fiber composite; τ_m = shear strength of the material at the weakest interface; ξ = strength efficiency factor (= 1 for continuous fiber composites), σ_c = longitudinal strength of a continuous fiber composite; and σ_m = strength of the matrix material. The influence of the fiber content on the physical properties of different thermoplastic materials has been studied by Loveless and McWilliams (68). They found that some effects in reinforced thermoplastics are simple functions of the volume fraction of the reinforcing fibers.

The shear transfer mechanism of stress from the matrix to the fiber when the latter is of finite length has already been mentioned. This leads to the concept of critical fiber length, which is the length necessary for the maximum stress in the fiber to reach the value of tensile fracture stress (7).

Usually a wide range of fiber lengths are present in thermoplastic composites. Bowyer and Bader (7) have derived a mathematical relationship for the stress-strain curve of moulded test pieces. They considered the spectrum of fiber lengths in the composite to be divided into sub-fractions whose length is shorter or larger than the critical fiber length. The mathematical model is as follows:

$$\sigma_c = C[\Sigma\frac{\tau L_i \phi_i}{2r} + \Sigma E_f \varepsilon_c (1 - \frac{E_f \varepsilon_c r}{2L_j \tau} \phi_j)] + E_m \varepsilon_c (1 - \phi_f) \quad [II\text{-}6]$$

where C = orientation factor whose value may be between 1 (perfect alignment) and 0.165 (random composite) (21); τ = shear strength of the fiber matrix bond; L_i = fiber length for the subcritical fiber fraction; L_j = fiber length for the supercritical fiber fraction; ϕ_i = volume fraction of subcritical fibers; ϕ_j = volume fraction of supercritical fibers; ϕ_f = total volume fraction of fiber; r = fiber radius; and ε_c = strain in composite. In practical systems, the terms E_m, E_f, and r can be readily obtained and the

relationships between σ_c and ε_c may be obtained from a tensile test. However, C and τ are generally not known, but the fiber length distribution can be determined. Assuming that C is independent of strain and is the same for all fiber lengths at least at small strains, then this model allows both C and τ to be determined from tensile test data.

As already mentioned, good interfacial adhesion is a condition for effecrive transfer of stress. In its absence, even long fibers will pull out of the matrix without breaking, which affects the reinforcing effect (13). Most interfacial adhesion studies in fiber filled thermoplastics have been carried out with concern for the improvement of short- and long-term mechanical properties of the composites as a result of pretreatment of the reinforcing fibers with coupling agents to promote adhesion to the polymer matrix in glass reinforced polyolefines (12, 13, 94).

Positive chemical bonding at the interface and chemical compatibility permitting intimate contact and operation of secondary forces are also factors. Other factors take into account the microconfiguration and frictional properties of the fiber surface and the geometrical effect of the area of contact which depends on the diameter and aspect ratio of the reinforcement (26). The influence of matrix orientation is considered by Patel and Bogue (90).

B. THEORY OF FLOW OF FIBER FILLED FLUIDS

Although the study of the rheology of suspensions began in 1906 with the work of Einstein (30) who investigated the case of dilute suspensions of spherical particles in Newtonian fluids, research on the rheology of suspensions of fiber has been limited and is of a more recent date. In 1922 Jeffery (54) considered the motions and viscosity of a suspension of ellipsoids in a classical theoretical study.

Batchelor (5) has developed a theory for the stress generated in a non-dilute suspension of elongated particles in a Newtonian fluid by pure straining motion. He considered each particle being free to translate and rotate with the surrounding fluid, and being so small that the effect of inertia forces in the relative motion near it was negligible.

In these circumstances, the contribution to the bulk or average stress due to the presence of the particles is given by:

$$\Sigma_{ij}^{(P)} = \frac{1}{V} \Sigma \int \sigma_{ik} \, x_j \, n_k \, dA \qquad [II-7]$$

where the integral is taken over the surface A_o of a particle and the summation is over the many particles contained in the averaging volume V in which the statistical properties of the suspension are stationary; $\sigma_{ik} \, n_k$ is the force per unit area exerted on the parricle surface by the

ambient fluid, at a point where the unit normal is $\underset{\sim}{n}$, and is to be determined as a property of the relative motion of the surrounding fluid near to the particle.

For an elongated particle of length 2 l whose surface is at a distance of order b from the particle "axis," where $b \ll 1$, Equation II-7 becomes

$$\int_{A_o} \sigma_{ik} x_j n_k \, dA = - P_j l^2 \int_{-1}^{1} F_i \, sds + O(b/l) \qquad [II-8]$$

where sl denotes distance along the particle axis from its center, $\underset{\sim}{P}$ is a unit vector parallel to the axis, and $\underset{\sim}{F}$ is the force per unit length exerted by the particle on the ambient fluid at position s. Considering that the component of $\underset{\sim}{F}$ normal to the particle makes no contribution to the integral for a particle on which no external force or couple acts. Batchelor gives the approximate relation

$$\Sigma_{ij}^{(P)} = -\frac{1}{V} \Sigma \, P_i \, P_j \, l^2 \int_{-1}^{1} \underset{\sim}{P} \cdot \underset{\sim}{F} \, sds \qquad [II-9]$$

for a suspension of elongated particles.

When the effect of the bulk motion causes each particle to take up the same preferred orientation, Equation II-9 becomes

$$\Sigma_{ij}^{(P)} = - \frac{P_i P_j}{V} \Sigma \, l^2 \int_{-1}^{1} \underset{\sim}{P} \cdot \underset{\sim}{F} \, sds \qquad [II-10]$$

which represents a particle stress system which is symmetrical about the common direction $\underset{\sim}{P}$ of the particle axis. Furthermore, only the deviatoric part of the expression II-9 or II-10 for the particle stress tensor is significant and the factor P_iP_j is replaced by $(P_iP_j - 1/3\ \delta_{ij})$ where δ_{ij} is the unit tensor. Thus, the complete expression for the bulk stress in a suspension of parallel particles in a Newtonian fluid of viscosity η and in a bulk pure straining motion represented by the rate of deformation tensor d_{ij} is

$$\sigma_{ij} = - p\delta_{ij} + 2\eta d_{ij} + (\frac{1}{3}\ \delta_{ij} - P_iP_j)\ \frac{1}{V}\ \Sigma\ 1^2 \int_{-1}^{1} \underset{\sim}{P}\cdot\underset{\sim}{F}\ sds \qquad [II\text{-}11]$$

where $p = - \frac{1}{3}\ \sigma_{jj}$ is the bulk pressure.

Bark and Tinoco (4) have used the equation given by Batchelor (II-11) to model the rheological properties of a dilute suspension of rigid fibers in plane Poiseuille flow. In this model, the direction of the suspended fibers is described by a vector field $\underset{\sim}{P}(\underset{\sim}{x},t)$, where $\underset{\sim}{x}$ is the position vector and t is the time. The stress tensor, in Cortesion coordinates, is given in terms of the vector field $\underset{\sim}{P}(\underset{\sim}{x},t)$ and the velocity field $\underset{\sim}{V}(x,t)$ by:

$$\sigma_{ij} = - p\delta_{ij} + 2\eta d_{ij} + \frac{\eta\phi r^2}{\ln 2r - 3/2}\ P_iP_jP_kP_l\ d_{kl} \qquad [II\text{-}12]$$

Batchelor (5) has also analyzed the elongational flow of concentrated fiber suspensions. In elongational flow of oriented glass fiber suspensions, shearing motions are set up between the fibers which result in increased resistance to elongational flow. Batchelor developed this view for a Newtonian fluid and found

$$\frac{x(\phi)}{3\eta_o(0)} = 1 + \frac{4}{9}\frac{R^2}{1_n\pi/\phi} \qquad [II\text{-}13]$$

where R is the aspect ratio and η_o is the Newtonian viscosity of the fluid. Goddard (39, 40, 41) has extended this analysis to suspensions of oriented rigid fibers in non-linear materials exhibiting fluidlike power law shear behavior. Goddard modified the above equation to obtain

$$x(\phi,\dot{E}) = x(0,\dot{E})\ \{1 + \frac{2}{9}R^{n+1}\phi[\frac{\frac{1-n}{n}}{1-(\pi/\phi)^{n-1/2_n}}]^n B\} \qquad [II\text{-}14]$$

where $B = \frac{9}{2+n}\frac{\eta(\dot{E})}{x(\dot{E})}$ and $\dot{E}$ is the elongational rate.

C. RHEOLOGICAL CHARACTERIZATION OF FIBER FILLED POLYMER MELTS

Zero Shear Viscosity of Pure Melts

It is well known that the rheological properties of polymer melts are strongly influenced by the molecular weight, molecular weight distribution, and degree of branching. Fox and Flory (36, 37) were the first to show

that the zero shear viscosity (η_o) of concentrated polymer solutions, and melts of linear polymers, it proportional to the molecular weight below a critical value, whereas above this critical value, it increases and becomes dependent on the 3.4 power of weight average molecular weight.

The dependence of the rheological behavior of polymeric materials on the molecular weight distribution (also called polydispersity) has been the subject of considerable investigation. Vinogradov and Malkin (111) have plotted a relative viscosity (η/η_o versus a relative shear stress ($\eta_o\dot{\gamma}$) for different polymer melts. Minoshima et al. (76) found that the relative viscosity (η/η_o) of PP melts is only a function of the relative shear stress ($\eta_o\dot{\gamma}$) and the molecular weight distribution, not the molecular weight or temperature. Middleman (75) proposed a method of constructing master viscosity curves with polydispersity as a parameter, by extending the Bueche theory. Another method for constructing master curves was suggested by Graessley and Segal (47) by using the molecular entanglement theory. In each study is found that broadening the molecular weight distribution produces a decrease in the melt viscosity.

Linear Viscoelastic Behavior of Pure Melts

Elastic recovery (recoil) has long been considered a useful parameter for determining fluid elasticity. It is often referred to as a measure of stored elastic energy and

it is characterized by the recoil per unit stress which is known as the steady state compliance J_e (18). The influence of molecular weight and molecular weight distribution on the steady state compliance has been studied by Masuda, Onogi, and Kitagawa (73, 86). Endo et al. (31) have observed the dependence of the steady state compliance on the shear rate for both narrow and broad molecular weight distribution polymers. J_e is roughly independent of molecular weight but broadening molecular weight distribution greatly increases J_e. An important rheological property, the relaxation spectrum, has been the subject of extensive measurements by rheologists (34, 109). The effects of molecular weight and molecular weight distribution on the relaxation spectrum of polymer melts have been investigated by Masuda, Kitagawa, Inoue and Onogi (73). Increasing absolute molecular weight increases the maximum relaxation time. Broad molecular weight distribution samples generally have much greater memory than would be expected from their weight average molecular weight.

Non-Newtonian Viscosity

A review of early experimental studies os simple shear flow of concentrated fiber suspensions was published by Maschmeyer and Hill (71). They also carried out one of the few studies of the rheology of concentrated suspensions of fibers in tube flow using glass fibers in high viscosity silicone oil (72).

Research on the rheology of fiber filled polymer melts has also been limited and it only dates from the middle 1960's. Charrier and Rieger (15), Chan, White and Oyanagi (14) and Knutsson, White and Abbes (62) describe consistent shear experimental viscosity data obtained on glass fiber melt suspensions in different instruments. The data are similar to those of the pure melt except for a higher viscosity value caused by the added fibers. Czarnecki and White (24) correlated viscosity shear rate data in a reduced form for suspensions of glass, aramid, and cellulose (Westvaco Pinnacle pulp) fiber in PS melts with very good results. Crowson and Folkes (22) have studied the effect of fiber concentration, fiber length and temperature on the shear viscosity of several glass fiber reinforced PP and nylon 6,6 melts. They proposed a qualitative explanation in terms of the fiber orientation study reported in a previous paper (23). White, Czarnecki and Tanaka (114) found that PS melt filled with small inorganic fibers (Franklin) exhibited the expected yield values in both shear and uniaxial extension.

Normal Stresses

Pollet (93) was the first who reported normal stress experiments in polymer melts. Recent studies of normal stress differences in polymer melts have been made by Han (48); Lee and White (67); Oda, White and Clark (85); and by Minoshima, White and Spruiell (76). Lee and White (67)

show that the principal normal stress difference N_1 is larger than the second normal stress difference N_2. Han (48) and Oda, White and Clark (85) found that the principal normal stress difference, N_1, in commercial polystyrene melts is a unique function of shear stress, σ_{12}, independent of temperature and molecular weight. Oda et al. (85) also developed an empirical power law expression to represent the relationship between normal stress difference and shear stress which increases with the breadth of the molecular weight distribution. Minoshima, White and Spruiell (76) found that broadening of the molecular weight distribution of polypropylene increases the non-Newtonian character of the shear viscosity function and increases the principal normal stress difference at fixed shear stress. They developed correlations for these properties in terms of molecular structure.

Shear flow normal stresses in fiber filled melts have been determined by Chan et al. (14); Czarnecki and White (24); and Knutsson, White and Abbas (62). These investigators found that shear flow normal stresses are increased by the presence of fibers in the polymer melt. Czarnecki and White (24) have also correlated the principal normal stress difference (N_1) for the glass-, aramid-, and cellulose-fiber filled polymer melts as a function of shear stress (σ_{12}). Their plots are of great interest because they show the relative influence of the fibers on the

principal normal stress difference and the shear stress and not the influence of N_i alone. The mechanism for the large normal stresses in fiber filled polymer melts is proposed by Chan et al. (14) to be due to the additive (perhaps synergistic) effect of normal stress effects induced by the viscoelastic continuous phase and the fiber induced phenomena described by Nawab and Mason (80), and others (71, 74) for suspensions of fibers in Newtonian fluids.

Elongational Flow

The elongational viscosity of fiber filled polymer melts has been studied by Chan et al. (14). The observed that (i) fibers substantially decrease the elongation to break of the filaments, and (ii) large elongational viscosities which show a strong decrease with elongational rate. The former result was confirmed by Patel and Bogue (90). The latter behavior was explained by using the model developed by Batchelor (5) and Goddard (39). In a more recent paper (41) Goddard found that quantitative agreement between the data of Chan et al. (14) and the Batchelor-Goddard theory (5, 39) was not good. White and Czarnecki (115) have discussed these results and they have suggested that the problem may exist in the actual fiber length distribution.

D. FLOW INDUCED ORIENTATION OF REINFORCING FIBERS IN THERMOPLASTIC PROCESSING

Utilization of high strength discontinuous fibers for reinforcing thermoplastics has produced a new class of commercially important engineering composites. These materials show improved physical properties relative to those of the unfilled material. It is well known that mechanical properties of composite systems depend strongly on the orientation of the reinforcing particles. During processing of thermoplastic composites, usually by extrusion, injection molding or similar processes, the fibers adopt complex patterns of orientation and these are retained in the final product. This will influence the mechanical properties of the composite which may show anisotropy caused by the flow induced orientation of the reinforcing fibers in a preferred direction.

Basic Hydrodynamic Studies and Model Systems

The first theoretical studies of particle motion in flowing liquids were achieved by Jeffrey (54) in 1922. In his work, Jeffery analyzed the motion of a prolate spheroid in shearing flow and developed equations to predict the orbit described by the particle in motion. However, after Jeffery's work, very little was done on the subject of particle motions in flow. At the beginning of the 1950's, Trevelyan and Mason (110) studied the motion of rigid

spheres and cylinders in simple shear flow using a coaxial cylinder apparatus. Thenceforth, S. G. Mason and his coworkers continued the study of the motion of particles of varying shapes in both dilute and concentrate suspensions (35, 46, 56, 38).

Forgacs and Mason (35) studied the motion of threadlike particles in Couette flow between coaxial cylinders. They analyzed the influence of the applied stress field on the fibers. Flexible filaments were observed to buckle during flow which they interpreted using Euler's theory of buckling of columns. The laminar viscous flow of suspensions of single spheres, rods and discs through tubes was investigated by Goldsmith and Mason (46). With the exception of effects due to interaction with the wall and neglect of particle size, the angular rotation of the spheres, rods and discs was in good agreement with the theory of Jeffery.

The behavior of rigid and deformable particles suspended in viscoelastic polymer solutions undergoing slow Couette and Poiseuille flow was studied experimentally by Karnis and Mason (56). They compared their results with similar observations in Newtonian suspending media, and suggested that the difference in behavior was due to normal stress effects. Gauthier, Goldsmith and Mason (38) investigated the behavior of rigid and deformable particles suspended in viscoelastic liquids (polymer solutions) undergoing slow Couette flow. They observed a steady drift

in the Jeffery orbits of rods towards an asymptotic orientation perhaps corresponding to minimum energy dissipation in the flow.

Hydrodynamic analysis of the slow motion of rod-like particles in a second order viscoelastic fluid (17) have been presented by Leal (64, 65) and Brunn (9). They have considered both shear flow and translation in a stagnant fluid.

Thermoplastic Composites

A number of patents have been developed concerning the subject of fiber orientation due to flow in polymer melts. Donald (27) has proposed an annular cylindrical die in which both core and outer annulus rotate. Cessna (11) has patented an annular conical die with a rotating core. Both die designs are intended to produce tubing with a circumferential orientation of the reinforcing fibers.

Most of the studies concerning the orientation due to flow of fiber suspensions have been made with molding compounds. The research has been achieved regarding experimental methods and the data obtained are generally qualitative. Thus, Bell (6) studied photographically the flow behavior of 50 percent by volume of glass fibers in an epoxy resin. He found that the fibers which were perpendicular to the flow direction in the region above the constriction region become aligned in the direction of flow

in the constriction region, with no further change in orientation as the fibers left the alignment slit.

Goettler and Lambright (44, 45) patented a process for controlling orientation of discontinuous reinforcing fibers in a composite formed by extrusion. They proposed a varying cross section annular die along its length for orienting the fibers from the axial direction. Later, they also proposed other diverging die designs to produce radial orientation in annular extrudates (45).

Another experimental approach to investigate the alignment of short fibers contained in suspension during flow of the suspension through a convergent channel has been made by Murty and Modlen (79). They obtained and analyzed flow patterns for suspensions of various fiber concentrations. Owen, Thomas and Found (87) have presented predictive rules for fiber orientation behind the flow front in molding polyester BMC. Lee and George (66) have studied the flow fields of suspended glass fibers in eposy resins flowing in transparent convergent channels. They used tracer fibers where position was recorded by motion pictures, and developed a data reduction technique to study the kinematics of the fiber suspension.

Darlington and McGinley (25) examined fiber orientation distribution in a glass-fiber reinforced nylon 66 specimen by the use of the contact microradiography (CMR) technique. Emphasis is given on the details of the

experimental technique which is then applied to obtain a qualitative estimation of the fiber orientation distribution in an injection molding tensile bar specimen. Crowson, Folkes and Bright (23) have made a study of the fiber orientation in short glass filled thermoplastics resulting from converging, diverging and shear flow. Using methods such as contact microradiography and direct observation of steel tracer fibers, they concluded that converging flow produces a high alignment of the fibers in the flow direction, diverging flow causes a 90° rotation of previsouly aligned fibers, and shear flow has the effect of partially disorienting the fibers.

Few studies have considered a quantitative approach to the fiber orientation due to flow. Goettler has developed a method for describing the complex orientation distribution of 3 mm long glass bundles in an epoxy molding compound (42), and showed that the degree of orientation produced in transfer or plunger molding of short fiber filled epoxy compounds can be controlled by mold design processing, conditions and formulation, as well as by part design (43). A quantitative relationship is found to exist between three-dimensional fiber orientation distribution and tensile modulus of the moldings.

Yoshida, Budinam, Okayama and Kitao (120) have used wide angle x-ray diffraction to study the orientation of polystyrene-graphite fiber composite. Series of composites

were prepared by extruding a mechanical mixture of 90 percent weight atactic PS and 10 percent weight of graphite fiber. The orientation degree of both components was determined as a function of processing conditions and geometry by two methods. The degree of orientation of distributing graphite fibers was evaluated by using x-ray diffraction, while that of matrix polystyrene was determined by a thermal retraction at a temperature above T_g. They found that the orientation of filler obtained from the intensity distribution curve for the azimuthal scanning of the (020) reflection, was at least 80 percent for all samples, whereas the polystyrene matrix was almost randomly oriented in all cases.

E. ORIENTATION

Uniaxial Orientation

Methods to specify quantitatively the uniaxial molecular orientation were first developed by P. H. Hermans and coworkers (50, 51, 52). This work has been further extended by Muller (78), Taylor and Darin (105), Stein (100, 101), Sack (98), Roe and Krigbaum (95, 96, 97) and McBrierty and Ward (69). An orientation function concept was developed in terms of the anisotropy of the polarizability tensor for a system with cylindrical fiber symmetry. Such an orientation function for a one-phase system was given as (78):

$$f^H = \frac{\overline{\alpha_{zz} - \alpha_{rr}}}{\alpha_1 - \frac{\alpha_2 + \alpha_3}{2}} = \frac{3\,\overline{\cos^2\phi} - 1}{2} \qquad [II\text{-}15]$$

where α_1, α_2, and α_3 are the principal polarizabilities, $\overline{\alpha_{zz} - \alpha_{rr}}$ is the mean value of the difference between the axial and radial polarizability, and $\overline{\cos^2\phi}$ is the mean square cosine of the angle between the chain axis (1) and the fiber axis, which is taken as the reference direction.

Herman's method to specify uniaxial orientation has been generalized by several investigators in different approaches. Roe and Krigbaum (96, 97) and McBrierty and Ward (69) have represented uniaxial orientation in terms of series of spherical harmonics in which the Herman's function is the first term.

Stein (101) has introduced orientation functions to specify the degree of orientation of each of the crystallographic axis in a crystalline polymer. These orientation functions are defined in the same form as Herman's factor as follows:

$$f_j = \frac{3\,\overline{\cos^2\phi_j} - 1}{2} \qquad [II\text{-}16]$$

where j stands for any of the crystallographic axis a, b, or c. Figure II-1 shows the geometry involved in the determination of the Herman-Stein uniaxial orientation factors, f_j, and Table II-1 shows the range of values that

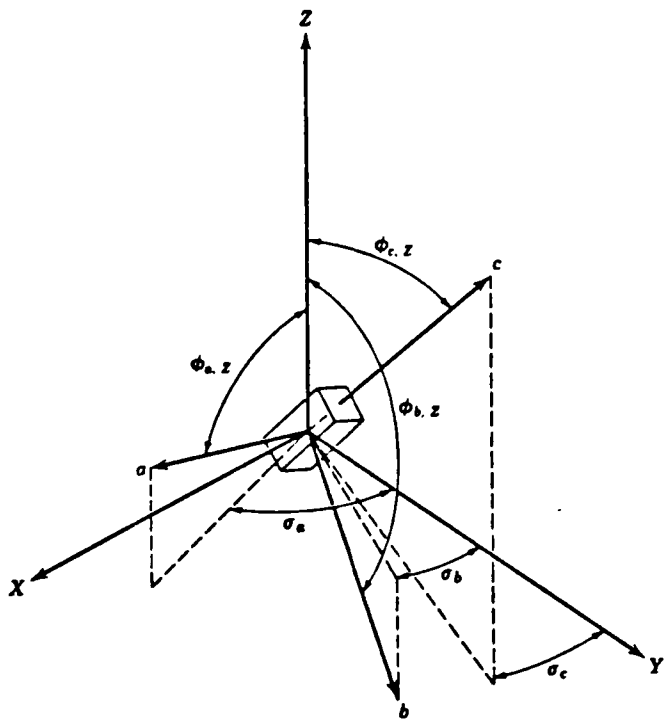

Figure II-1. Stein's coordinate system for specifying orientation modes in orthorhombic polymers [after Stein (101)].

these factors assume for different types of orientation distribution.

Table II-1

Values of $\cos^2\phi$ and f for Three States of Orientation

	Orientation with Respect to Reference Direction Z		
Parameter	Parallel	Random	Perpendicular
$\cos^2\phi$	1	1/3	0
f	1	0	-1/2

When the crystallographic axes are orthogonal, the equation is

$$\cos^2\phi_{a,1} + \cos^2\phi_{b,1} + \cos^2\phi_{c,1} = 1 \qquad [II-17]$$

and

$$f_1 + f_b + f_c = 0 \qquad [II-18]$$

Thus, only two of the orientation factors are independent and therefore a ternary diagram can be used to represent the orientation. Figure II-2 shows the graphical representation of the orientation factors as suggested by Stein (101).

Biaxial Orientation

Stein was the first who considered the problem of biaxial orientation in orthorhombic polymers (102, 103). He defined a new set of three biaxial orientation factors

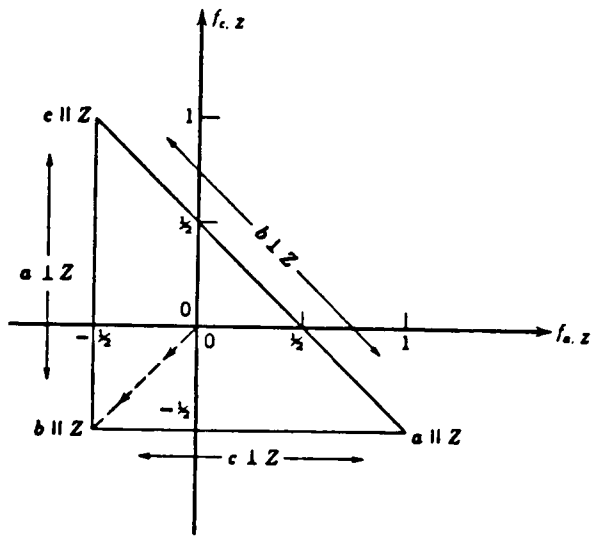

Figure II-2. Representation of uniaxial orientation [after Stein (101)].

for polymeric films based upon the aximuthal (Euler's) angles for each of the crystallographic axes. Stein's biaxial orientation factors are given by

$$f_{\psi_j} = 2\,\overline{\cos^2\psi_j} - 1 \qquad \text{[II-19]}$$

where ψ_j represents the Eulerian longitude angle between a given crystallographic axis and an axis in the plane of the film. Stein's biaxial orientation factors can assume values between +1 and -1 for each crystallographic axis. Wilchinsky (117) suggested the use of $\overline{\cos^2\phi_{hkl,j}}$, where hkl stand for the Miller indices of the crystallographic plane being considered, as a representation of multiaxial orientation.

Analytical representation of biaxial orientation factors in terms of spherical harmonics and expansion of associated Legendre polynomials has been considered by Roe (95) and by Nomura et al. (81-83). However, as the Stein's biaxial orientation factors, these representations are also in terms of Euler's angles for the crystallographic axes and are, therefore, referred to a single specific direction in the processed material. White and Spruiell (116) have proposed a set of biaxial orientation factors based upon the angles between the polymer chain and the machine and transverse direction as shown in Figure II-3. This leads to the definition of two biaxial orientation

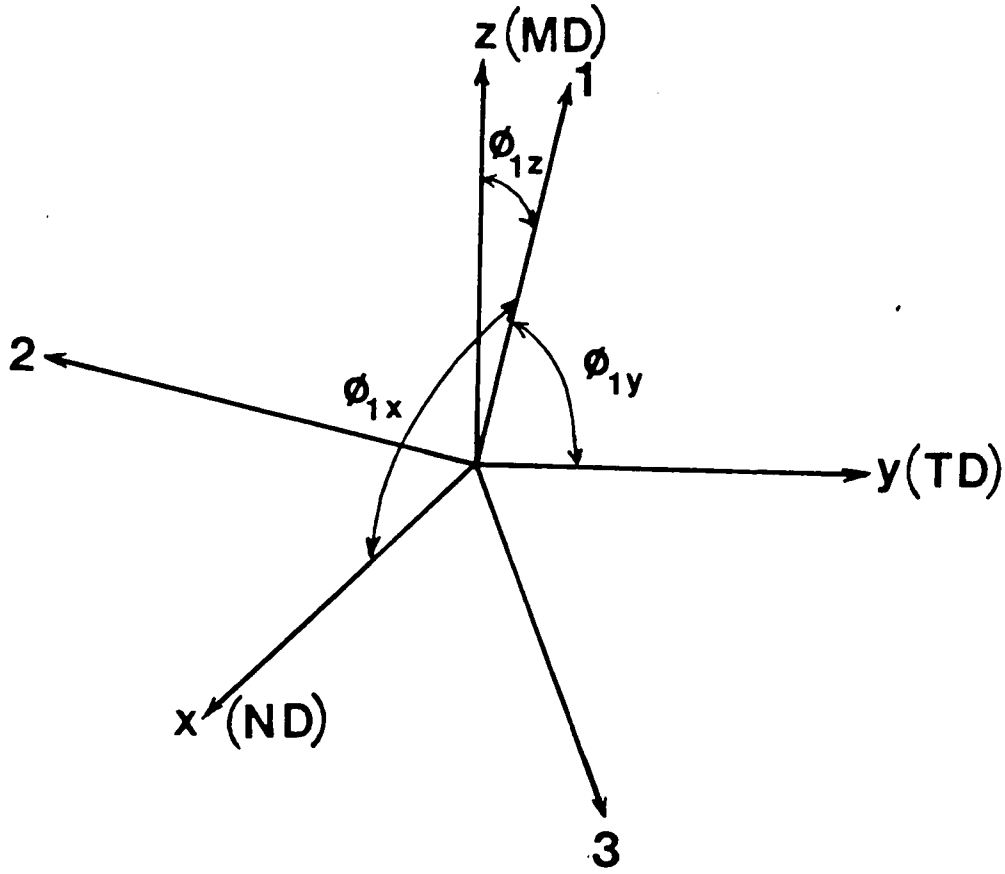

Figure II-3. White-Spruiell coordinate system, x,y,z, axes of film, 1,2,3, axes of the polymer molecule.

factors for the chain orientation as

$$f_z^B = 2\,\overline{\cos^2\phi_{1z}} + \overline{\cos^2\phi_{1y}} - 1 \qquad \text{[II-20a]}$$

$$f_z^B = 2\,\overline{\cos^2\phi_{1y}} + \overline{\cos^2\phi_{1z}} - 1 \qquad \text{[II-20b]}$$

where 1 refers to the chain direction and z and y stand for the reference directions.

The orientation factors defined by Equations II-20a and II-20b can be generalized to include all three crystallographic axes in orthorhombic crystals. Thus, the following expressions are obtained:

$$f_{za}^B = 2\,\overline{\cos^2\phi_{az}} + \overline{\cos^2\phi_{aj}} - 1 \qquad \text{[II-21a]}$$

$$f_{ya}^B = 2\,\overline{\cos^2\phi_{ay}} + \overline{\cos^2\phi_{az}} - 1 \qquad \text{[II-21b]}$$

$$f_{zb}^B = 2\,\overline{\cos^2\phi_{bz}} + \overline{\cos^2\phi_{by}} - 1 \qquad \text{[II-21c]}$$

$$f_{yb}^B = 2\,\overline{\cos^2\phi_{by}} + \overline{\cos^2\phi_{bz}} - 1 \qquad \text{[II-21d]}$$

$$f_{zc}^B = 2\,\overline{\cos^2\phi_{cz}} + \overline{\cos^2\phi_{cy}} - 1 \qquad \text{[II-21e]}$$

$$f_{yz}^B = 2\,\overline{\cos^2\phi_{cy}} + \overline{\cos^2\phi_{cz}} - 1 \qquad \text{[II-21f]}$$

From the orthogonality of the crystallographic axes, it follows that only four of the six White-Spruiell orientation factors are independent. It should be also noted that in the uniaxial case, these orientation factors reduce to the Herman's orientation factor.

A graphical representation of the White-Spruiel orientation factors is possible by means of an isosceles triangle with an isotropic system located at the origin as shown in Figure II-4.

F. CHARACTERIZATION OF ORIENTATION

A knowledge of the fiber orientation distribution is essential in order to predict the mechanical behavior of short fiber reinforced thermoplastics. Several methods (1, 32, 55, 108) have been applied, developed or modified to investigate the variation of fiber orientation distribution in fabricated short fiber reinforced parts. Some techniques are limited to a qualitative information regarding the fiber orientation distribution, others require that the system under study meet specific characteristics in order to be applied and, in general, there is not an absolute technique capable of producing quantitative results and having general application. Techniques such as scanning electron microscopy (SEM) (108), contact microradiography (CMR) (32), and wide angle x-ray diffraction (1, 55) have been applied with more or less success to the determination of fiber orientation distribution in short fiber reinforced thermoplastics (23, 25, 89, 120).

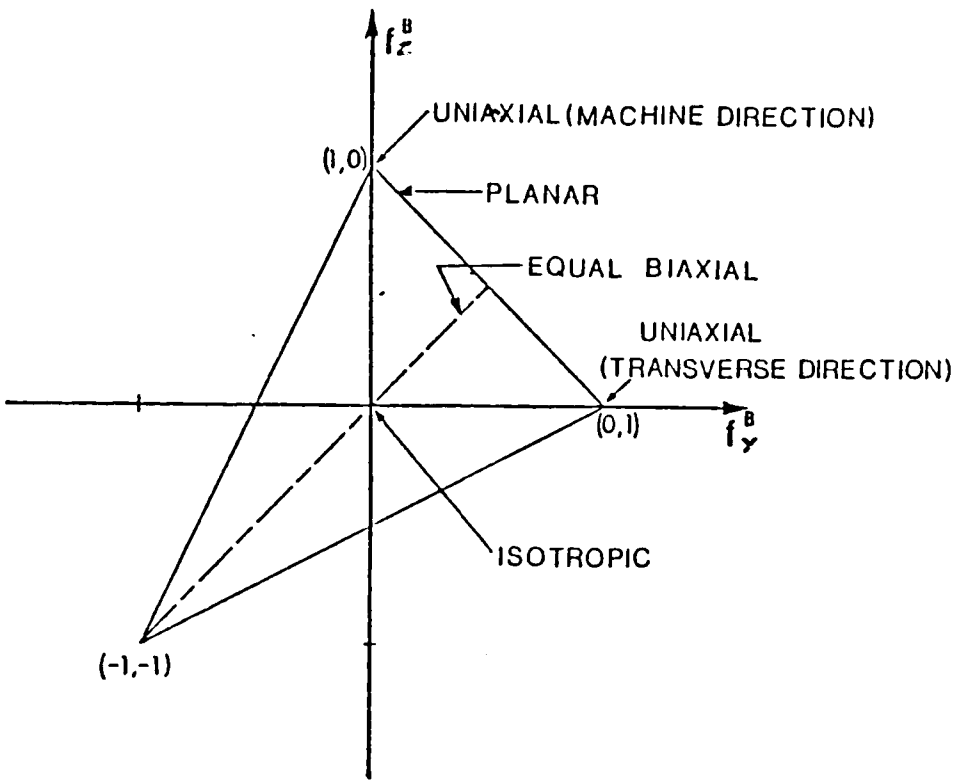

Figure II-4. Graphical representation of orientation, the orientation triangle diagram [White and Spruiell (116)].

Scanning Electron Microscope (SEM) Technique

This technique, of great importance in studying surface characteristics of polymeric materials, has also been applied to the determination of fiber orientation distribution in short fiber reinforced thermoplastics (89).

In the scanning electron microcope (108), electron lenses are used to demagnify the image of a source and produce a focused spot on the sample under investigation. The spot scans the area to be examined in a manner similar to a TV camera, and secondary or reflected electrons are collected by means of a suitable detector; the signal is amplified and displayed on a cathode-ray tube which is synchronized with the deflector system.

The scanning microscope can also be used with detectors set to receive x-rays excited by the specimen. Figure II-5 shows a schematic arrangement of a scanning electron microscope.

An estimate of teh fiber orientation distribution in short fiber reinforced plastics (89) can be made by looking at specimen cross-sections under the scanning electron microscope. The procedure is shown in Figure II-6, and use is made of the following equation (89):

$$\theta = \cos^{-1} \left(\frac{d_1}{d_2}\right) \qquad [II-22]$$

This technique, however, requires a laborious preparation of the specimen by polishing and etching in order

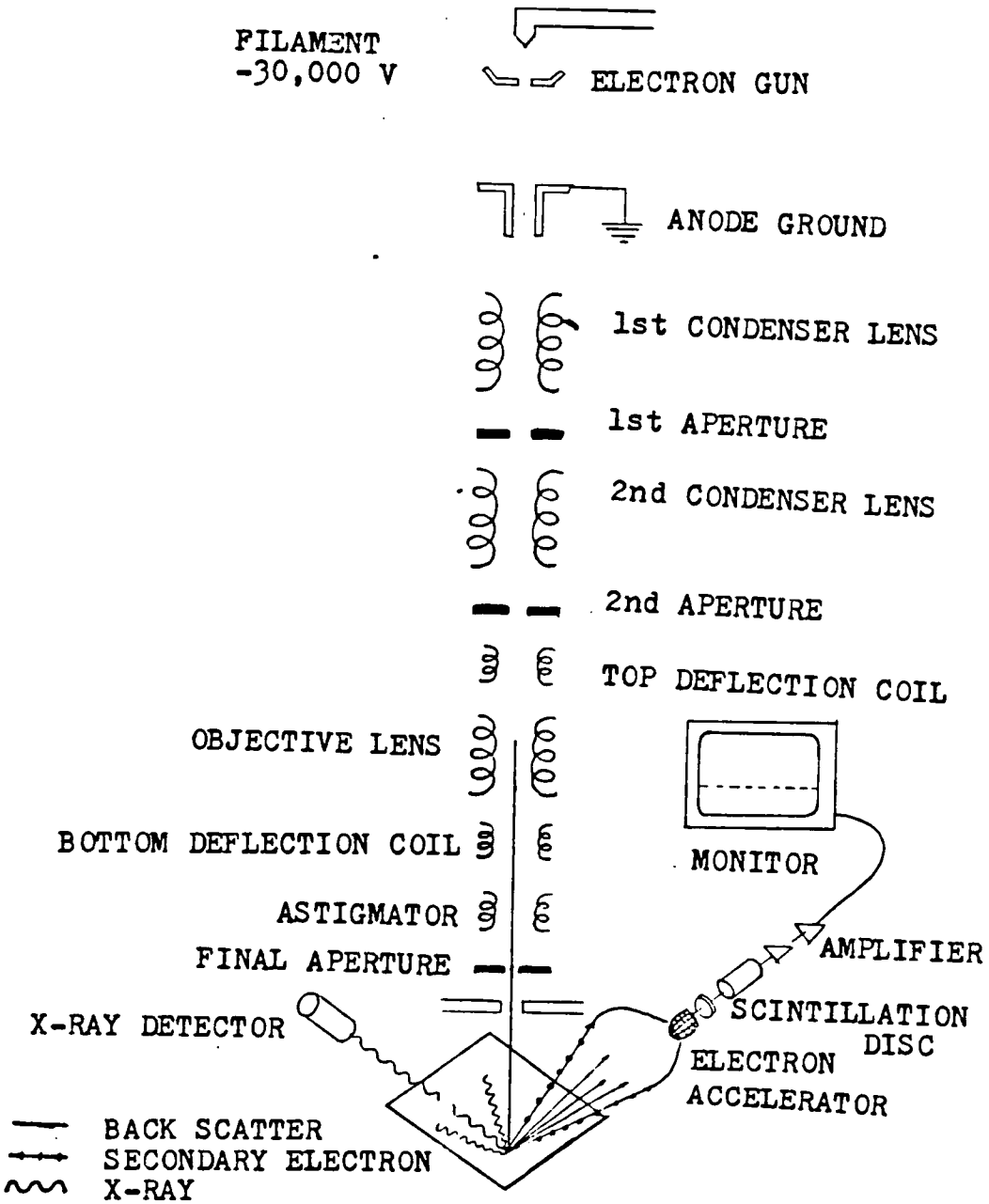

Figure II-5. Schematic arrangement of a scanning electron microscope.

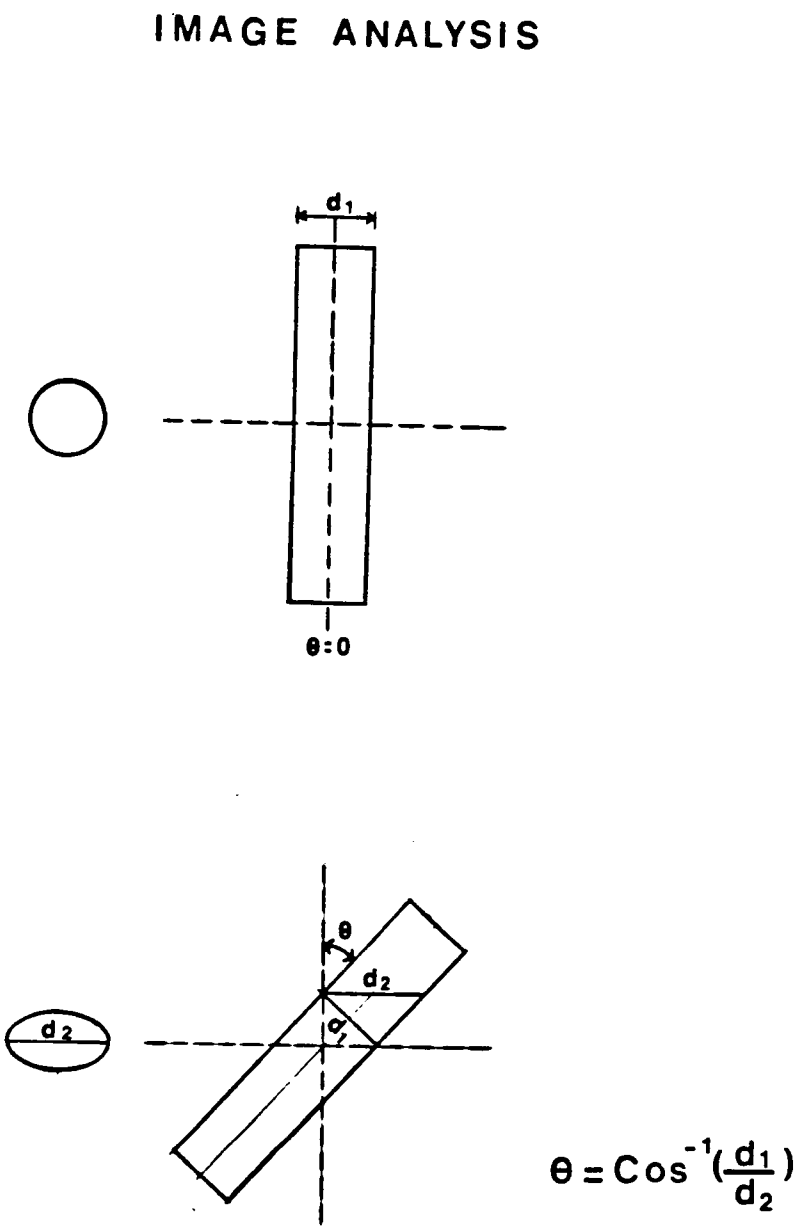

Figure II-6. Method for evaluation of fiber orientation.

to ensure an adequate contrast between the fiber and matrix (89).

Contact Microradiography (CMR) Technique

The difficulties involved in the specimen preparation for the SEM technique can be eliminated by the use of the contact microradiography (CMR) technique (32). This technique, extensively applied to biological research for many years, has also been used to study the fiber orientation distribution in short fiber reinforced thermoplastics (23, 25).

In this technique, the specimen thickness is reduced in order that the number of images cast does not confuse the overall picture. The specimen is then placed as close to the photographic emulsion as possible. The microradiographic image is thus virtually the same size as the specimen.

In studies involving short fiber reinforced plastics carried out by Darlington and McGinley (25) and by Crowson, Folkes and Bright (23), the contrast between the image of the fiber (glass) and the background matrix (nylon 66 and PP) depends on the thickness of the fiber along the x-ray beam path and the difference between the x-ray absorption coefficients (μ [=] cm^{-1}) of the fiber and matrix. Since this difference increases with x-ray wavelength, the softer radiation is more suitable.

Although very useful for examining the through-thickness fiber orientation distribution in short fiber reinforced plastics parts, this technique does not provide quantitative information.

X-Ray Diffraction Techniques

Although there are several well-standardized diffraction techniques used for polymer analysis, the special importance of the flat film transmission technique in analyzing polymeric materials should be emphasized. Practically, complete diffraction patterns of unoriented and uniaxially oriented polymers can be recorded in flat films.

X-ray photographic techniques are specially important in the characterization of fiber structure for crystallizing fibers. General reviews of these techniques are given in monographs by Alexander (1), Kakudo and Kasai (55), Klug and Alexander (61) and Samuels (99) among others. The geometry involved in the flat film technique (normal beam transmission mode) is depicted in Figure II-7.

The optimum thickness of the specimen which will produce the maximum diffracted intensity is given by

$$T = \frac{1}{\mu} \qquad [II-23]$$

where μ is the linear absorption coefficient of the specimen for the x-ray wavelength used.

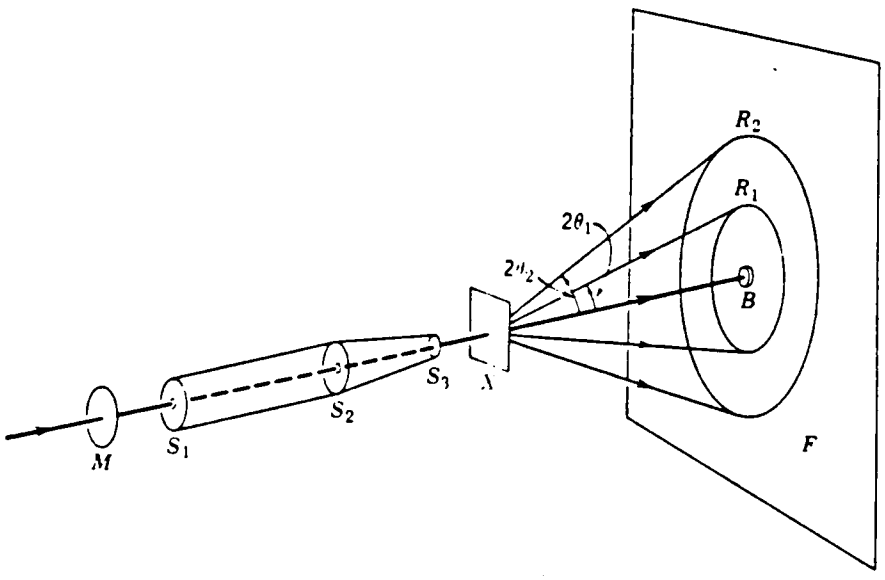

Figure II-7. Flat-film technique arrangement. M, Filter; S_1, S_2 and S_3, Collimator apertures; X, Sample; B, Beam stop; F, Film.

A convenient means to describe and represent the degree of preferred orientation of the crystallites in textured specimens is the stereographic projection known as pole figure. This is derived from a spherical projection and shows the density of crystallographic poles of a given set of planes as a function of orientation. In the absence of crystalline orientation, the poles will be distributed all over the stereographic projection. However, if orientation is present, the poles will tend to be concentrated in certain areas within the stereographic projection.

The Bragg angle θ corresponding to any transmission ring or spot in a flat film is found from the following relationship:

$$\text{Tan } 2\theta = \frac{r_1}{R_f} \qquad \text{[II-24]}$$

where r_1 = distance of ring or spot from the center of the film, and R_f = specimen-to-film distance.

The molecular orientation present in the polymer specimen can be determined from measurements of the azimuthal intensity of the Debye rings in a flat-film pattern by means of a microphotometer. Figure II-8 shows the angular coordinates α (longitude), β (latitude) and $\phi = 90° - \beta$ (colatitude) of a pole on a spherical projection.

The principal advantage of modern counter diffractometer techniques is the high degree of accuracy with which x-ray intensities can be measured. In studies of

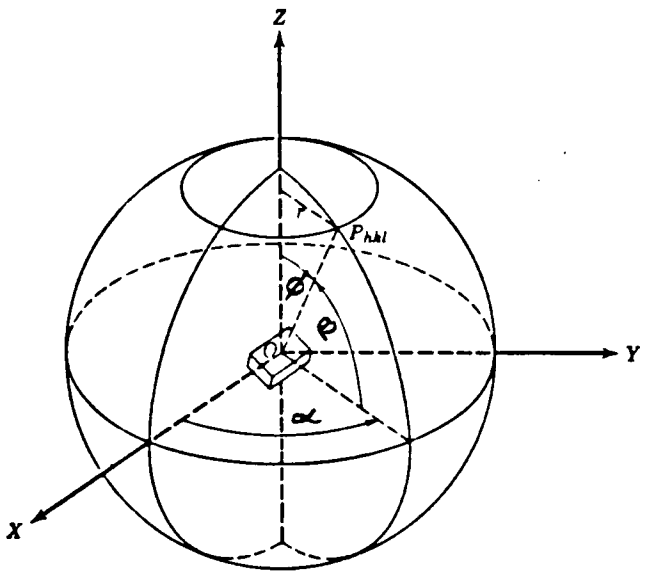

Figure II-8. Angular coordinates of a pole on a spherical projection.

polymers using the wide technique ($5° \leq 2\theta \leq 90°$) unmodified instruments allow the specimen to be mounted in two symmetrical arrangements: symmetrical-transmission and symmetrical-reflection. The symmetrical-transmission mode is the most suitable for the study of polymeric materials with fiber symmetry. Details of these arrangements and selected references regarding the application of diffractometer techniques to polymeric materials can be found in the excellent monographs by Alexander (1), Kakudo and Kasai (55) and Klug and Alexander (61). A study involving the use of wide angle diffractometer techniques to determine the fiber orientation distribution in a polystyrene-graphite composite has been carried out by Yoshida et al. (120). They prepared a series of composites by extruding a mechanical mixture of 90 weight percent atactic polystyrene and 10 weight percent graphite fiber. The orientation degree of both components were determined as a function of processing temperature and geometry. The degree of orientation of distributing graphite fiber was evaluated by means of x-ray diffraction, while that of matrix polystyrene was determined by a thermal retraction at a temperature above T_g. From the intensity distribution curve for the azimuthal scanning of (020) reflection, the orientation of filler was determined to be at least 80 percent for all samples. Matrix polystyrene turned out to be almost randomly oriented in all composite samples.

Figure II-9 shows the schematic of the geometry of an x-ray diffractometer. When studying the preferred orientation in materials, the standard specimen holder can be replaced by an Eulerian full circle goniometer. The coordinate geometry for orienting the specimen is based upon the Eulerian coordinate system and is shown in Figure II-10.

When using the orientation functions described in the preceeding section to specify quantitatively the preferred orientation in a given specimen, the numerical values of the mean-squares cosines can be determined from the fully corrected intensity distribution $I(\phi,\alpha)$ averaged over the entire surface of the orientation sphere. This requires weighing $I(\phi,\alpha)$ by $\sin\phi$. Thus, the equation (1, 55):

$$\overline{\cos^2\phi_{hkl,z}} = \frac{\int_0^{\pi}\int_0^{2\pi} I(\phi,\alpha)\cos^2\phi\sin\phi\, d\alpha d\phi}{\int_0^{\pi}\int_0^{2\pi} I(\phi,\alpha)\sin\phi\, d\alpha d\phi} \qquad [II\text{-}25]$$

Also,

$$I(\phi) = \int_0^{2\pi} I(\phi,\alpha)\, d\alpha \qquad [II\text{-}26]$$

Therefore,

$$\overline{\cos^2\phi_{hkl,z}} = \frac{\int_0^{\pi} I(\phi)\cos^2\phi\sin\phi\, d\phi}{\int_0^{\pi} I(\phi)\sin\phi\, d\phi} \qquad [II\text{-}27]$$

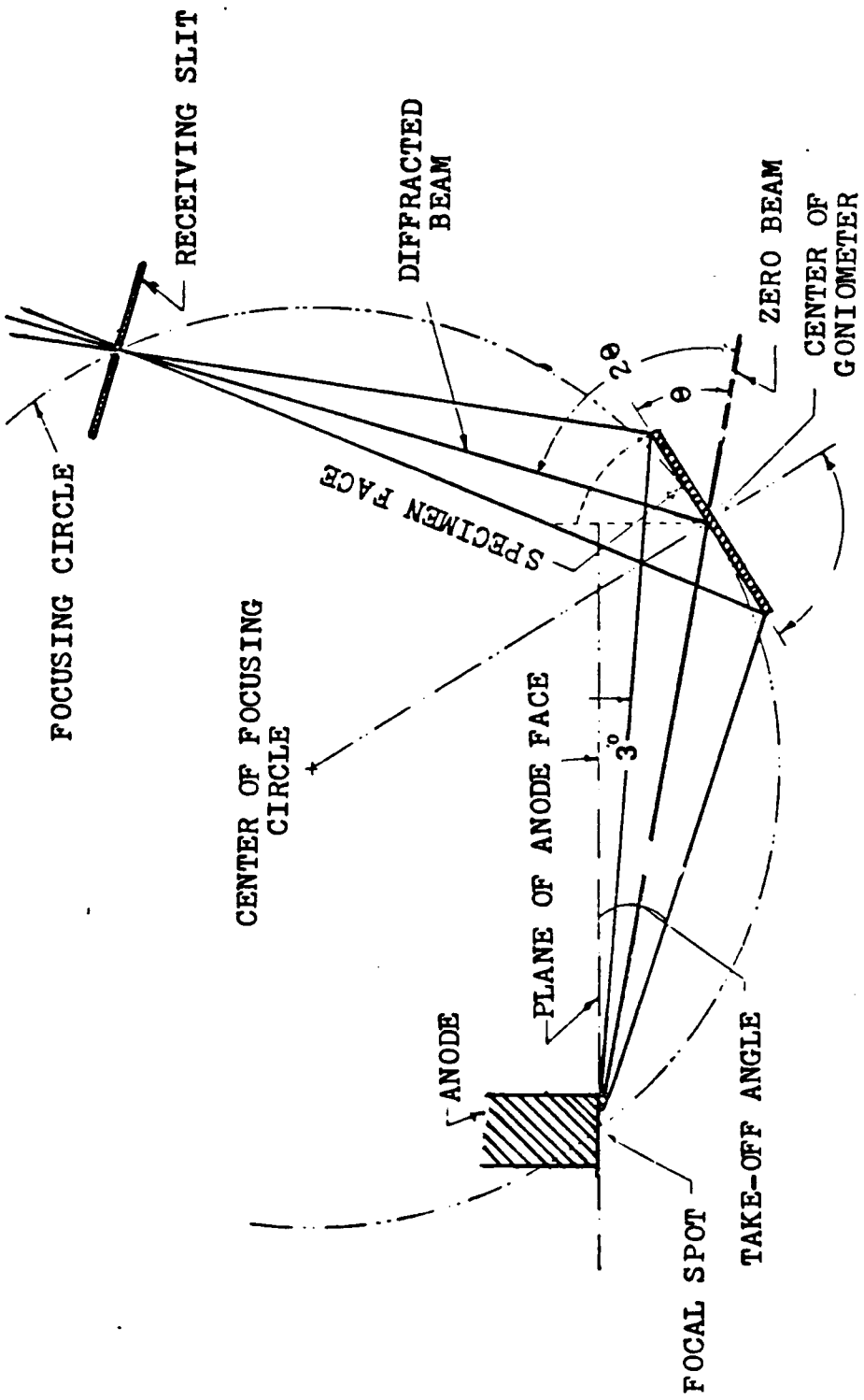

Figure II-9. Schematic arrangement of an x-ray diffractometer.

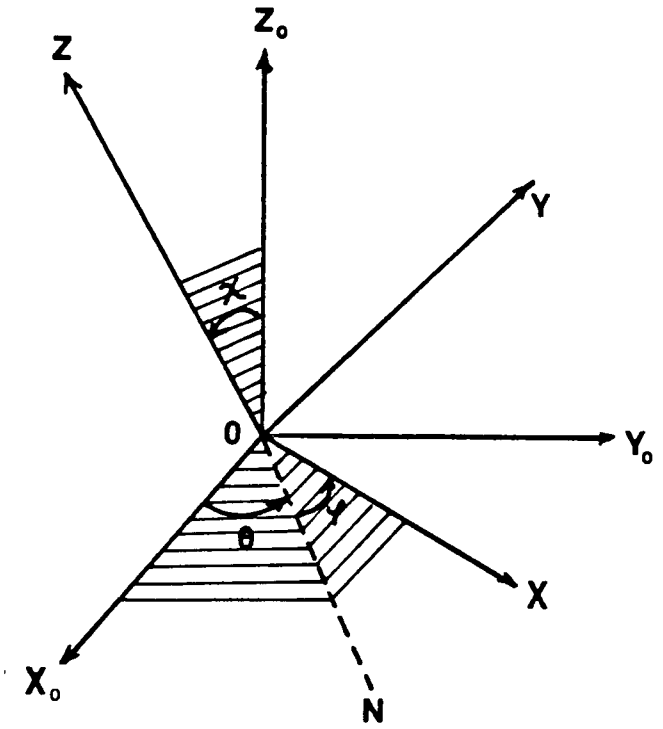

Figure II-10. Coordinate system for orienting the specimen in an Eulerian circle goniometer.
N, Normal to vertical circle (Axis of Chi);
Z, Axis of Phi circle (crystallographic direction);
Z_o, Main axis of the goniometer and diffractometer;
xY, reciprocal lattice plane;
x_oY_o, Diffractometer plane;
x_o, Direction of the x-ray beam;
0, Specimen.

In the case of axially oriented specimens (fiber symmetry), the diffracted intensities are independent of α, and only integration (II-27) needs to be calculated.

CHAPTER III

MATERIALS AND EXPERIMENTAL PROCEDURES

A. MATERIALS

General

Since the purpose of this research is to study the flow induced orientation of short reinforcing fibers suspended in a polymer melt as a result of varying processing conditions and geometry by means of wide angle x-ray diffraction techniques, it is necessary for the materials to have specific characteristics which allow a reliable identification of each component in the mixture using x-ray radiation. Furthermore, it is also required that the fiber orientation distribution in the composite be determined quantitatively by the same technique. These requirements and the special ability of x-ray diffraction to distinguish ordered from disordered states suggest the choice of a system fiber-matrix with components having different structural order. From these considerations, it is reasonable to think of an amorphous (disordered) polymer matrix and highly crystalline (ordered) reinforcing fibers as a suitable system for our purpose.

Reinforcing Fibers

The choice of reinforcing fibers having a high degree of crystallinity (order) has to be done paying special attention to the physical characteristics of the selected materials. Advantages of synthetic polymer fibers as compared to inorganic ones in reinforcing thermoplastic materials (59) need also to be considered. The mixing procedure used to prepare the composite and the processing of the composite in itself requires that the fiber structure remain stable at the working temperatures. Furthermore, a good resistance to mechanical damage is highly desirable to preserve the fiber structure free of possible alterations during the mixing and processing steps. At this point, a preliminary decision is made in the selection process towards the use of synthetic polymer fibers as reinforcing material in the system. Possible materials were carbon aramid (Kevlar) and nylon 66 fibers.

Results of fiber damage studies during mixing and mastication of aramid-fiber reinforced polystyrene melts carried out by Czarnecki and White (24), technical information (manufacturer) about the thermal stability of the materials, and preliminary flat-film patterns of the fiber samples available, led us to make a final selection favorable to the aramid fibers as the most suitable crystalline reinforcing material for our system.

The specific selected material was Kevlar 49, an aramid staple fiber provided by E. I. du Pont de Nemours and Company. Kevlar 49 continuous yarn was also supplied in order to carry out proper studies of orientation in the pure fiber.

Polymer Matrix

An amorphous polymer matrix has to be selected at this stage. Chemical stability in the polymer matrix has to be also considered during the selection process in order to obtain a suitable material for our purpose.

Although in amorphous materials there is no short- or long-range order of a truly crystalline nature (1), there is still present a minimal kind of short-range order consisting of the most probable distance between neighboring atoms. These modes of short-range order are responsible for the interference halos observed in the diffraction patterns of disordered polymers. It is highly desirable to avoid interference (overlapping) of the amorphous halos of the matrix with the crystalline reflections of the reinforcing fibers because of the difficulties involved in resolving the crystalline and amorphous scattering. From this, a preliminary choice of two amorphous matrices was made, allowing for the difference in the Bragg angle (θ) corresponding to the principal amorphous halo. The selected materials were polystyrene (PS) and

polymethylmethacrylate (PMMA), having their principal amorphous halos located at 2θ values of 18.4° and 13.5°, respectively.

A final selection was made in favor of the PMMA matrix, after observing the x-ray scattering curves of composite samples as a function of the Bragg angle. The principal amorphous halo of the PS matrix overlapped the main equatorial reflections of the Kevlar fibers.

The specific selected material was Plexiglas V-811, a medium molecular weight acrylic resin having a maximum heat resistance and suitable for injection molding and extrusion processes. This material was supplied by Rohm and Haas Company. Table III-1 shows the physical characteristics of selected materials.

B. PREPARATION OF MATERIALS

Fibers

The aramid staple fiber commercially available with a nominal length of 1/4 in (6.35 mm) was originally intended to be the only fiber length involved in this study. However, a second system was also considered. In this system, the mean fiber length was made smaller than the diameter of capillaries used to characterize the rheological behavior of the system, in order to compare the effect of fiber length on the flow properties and development of fiber orientation due to flow. This required a supply of short

Table III-1

Physical Characteristics of Materials

	Kevlar 49 Aramid Yarn	Kevlar 49* Aramid Staple	Plexiglas V-811** PMMA Pellets
Linear Density, Decitex	1270	-	-
Density, gm/cm^3	1.44	1.44	1.19
Diameter, mm	-	0.0122	-
Length, mm	-	6.35	-
$\bar{M}w$	-	-	1.09×10^5***
$\bar{M}n$	-	-	4.38×10^5***
$\bar{M}w/\bar{M}n$	-	-	2.49***

*E. I. du Pont de Nemours and Company

**Rohm and Haas Company.

***Sample characterization supplied by the manufacturer.

aramid fibers having a length of less than 2 mm (the largest diameter of available capillaries) and with a narrow length distribution. The difficulties involved in cutting aramid fibers are well known; however, after winding the continuous aramid yarn around a piece of cardboard (28 x 10 cm), tying a piece of thread to it, andthen pulling it through a plastic drinking straw, it was possible to cut the fibers with a very sharp knife. The length of the fibers so obtained was very uniform and the mean length, determined from the drinking straw length (25 cm) and the number of cuts done, turned out to be 1.18 mm (average of 4033 cuts with a standard deviation of 0.035).

Drying

Polymethylmethacrylate pellets were dried in a vacuum oven for four hours at 94°C. These drying conditions were based upon technical information given by the manufacturer.

Mixing

The aramid fibers were dispersed using a combination of a two-roll mill and a 1.9 cm (diameter) Brabender screw extruder. The system PMMA-V811-K49 with a composition 80/20 in volume was massed in the laboratory mill having 7.6 x 17.8 cm rolls for a period of 45 minutes at 180°C and 20 RPM. The gap between the rolls had a nominal set of 3.25 mm, and was opened periodically during the mixing period in order to ensure a homogeneous distribution of

the reinforcing fibers in the PMMA matrix. The system was then extruded at 190°C with a screw speed of 30 RPM. The extrudate was cut with a pair of scissors as it was coming out of the die (L/D = 5, D = 3.18 mm) in order to obtain pellets similar to those of the pure PMMA matrix.

Table III-2 summarizes the characteristics of the systems investigated in this study, and Figure III-1 shows the procedure followed to prepare these systems for rheological characterization.

C. EXPERIMENTAL PROCEDURES

Shear Flow Measurements

Rheological measurements in the low shear rate region were made on a Mechanical Spectrometer (manufactured by Rheometrics, Inc., Union, New Jersey). A cone and plate geometry was used to measure the shear stress (σ_{12}), and the principal normal stress difference (N_1).

The shear stress was measured through the torque T, and the principal stress difference through the thrust F, using the following equations (19):

$$\sigma_{12} = \frac{3T}{2\pi R^3} \qquad [III-1]$$

$$N_1 = \sigma_{11} - \sigma_{22} = \frac{2F}{\pi R^2} \qquad [III-2]$$

$$\dot{\gamma} = \frac{\Omega}{\alpha} \qquad [III-3]$$

Table III-2

Characteristics of the Systems Investigated

	Fiber	Length	Loading %* Weight W	Volume ϕ
1.	Aramid (Kevlar 49)	6.35 mm	0	0
	Staple		25.3	20
2.	Aramid (Kevlar 49)	1.18 mm	0	0
	Short fibers cut from continuous yarn		25.3	20

* $$\phi = \frac{\frac{W_F}{\rho_F}}{\frac{W_F}{\rho_F} + \left[\frac{(1 - W_F)}{\rho_P}\right]}$$

where F = Fiber, P = Polymer and ρ = density.

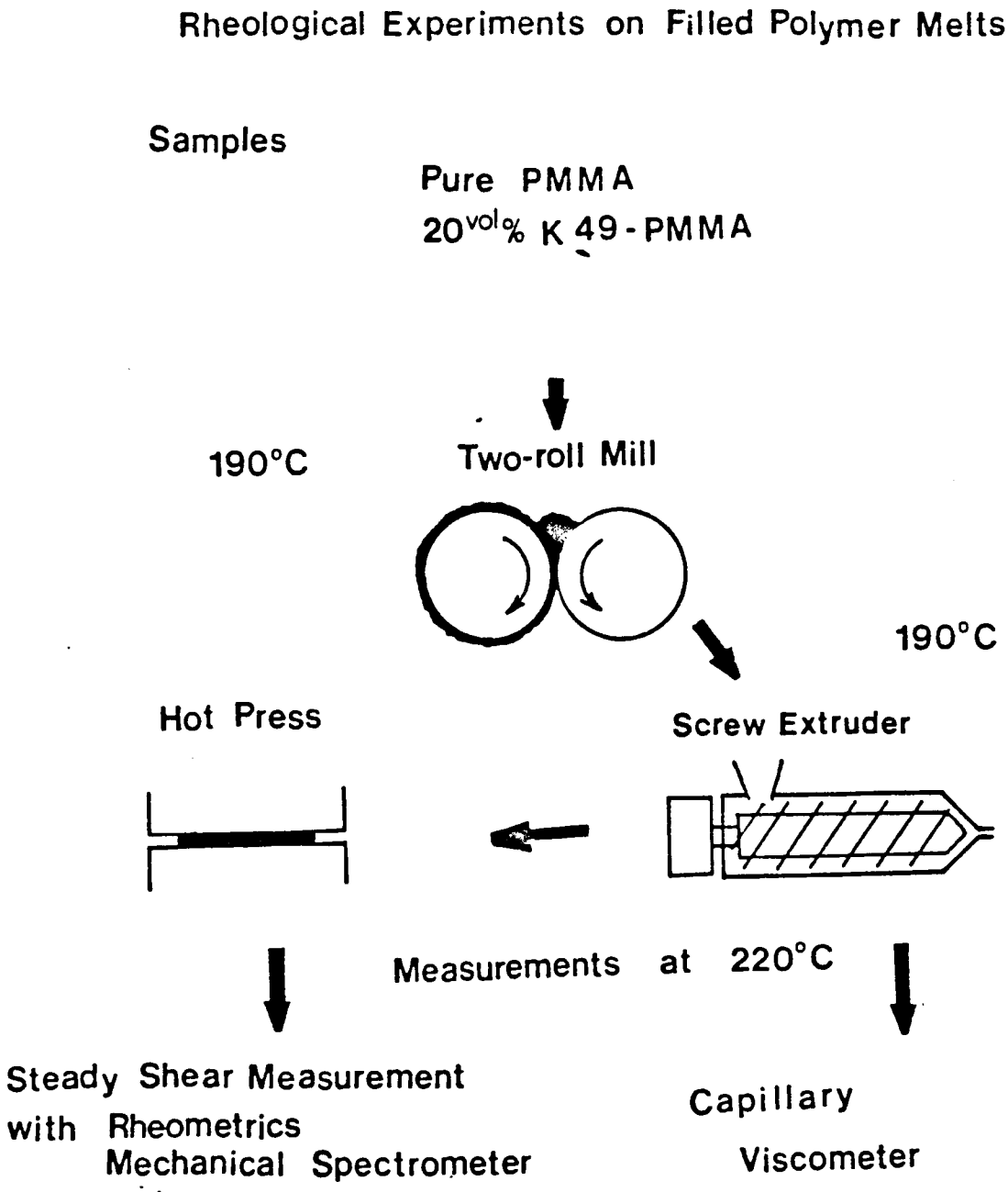

Figure III-1. Preparation of composites.

where R is the cone radius; Ω is the angular velocity; and α is the cone angle. A cone diameter of 2.5 cm with an angle of 0.1 rad was used in these studies. Sheet samples prepared by compression on a hot press at 220°C were placed in the gap and measurements carried out at 220°C. Figure III-2 shows the geometry of the cone and plate instrument attached to the Rheometrics mechanical spectrometer.

The flow behavior in the high shear rate region was studied by means of a capillary rheometer (Instron Corporation, Canton, Massachusetts). The instrument consists of a rod-like plunger driven by an Instron tensile tester crosshead, a heated barrel (915 mm in diameter), and a precision bore capillary die mounted in its lower end. The plunger is connected to an Instron load cell which measures the load required to force the melt contained in the barrel through the capillary die. The plunger constant velocity is also recorded. From these data, a total pressure drop and volumetric flow rate are obtained. Figure III-3 shows the geometry of a capillary viscometer.

The shear stress exerted by the melt on the capillary wall ($\sigma_{12,w}$) is easily obtained by means of a force balance (19).

$$\sigma_{12,w} = \frac{D\Delta P_{die}}{4L} \qquad [III-4]$$

where D = die diameter, ΔP = pressure drop required to extrude the melt through the die, and L = die length. As

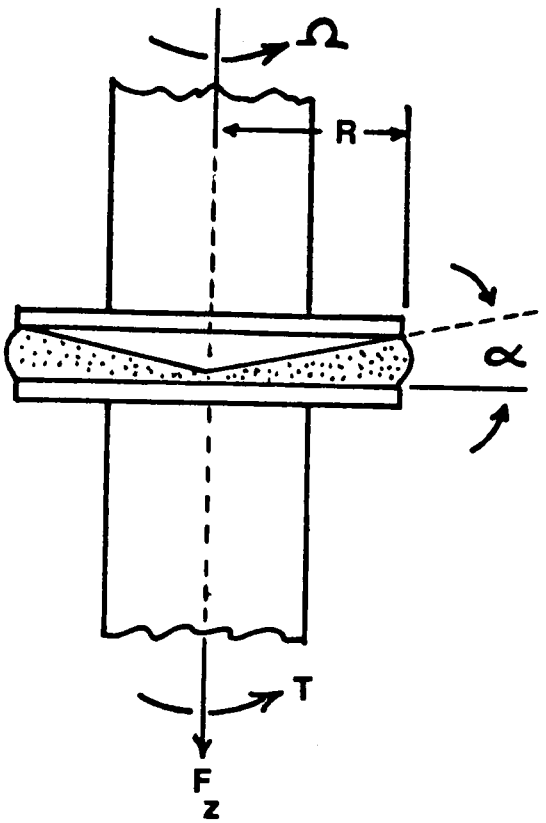

Figure III-2. Cone and plate viscometer geometry.
R = cone radius
α = cone angle
Ω = angular velocity
F_Z = thrust
T = torque

CAPILLARY VISCOMETER

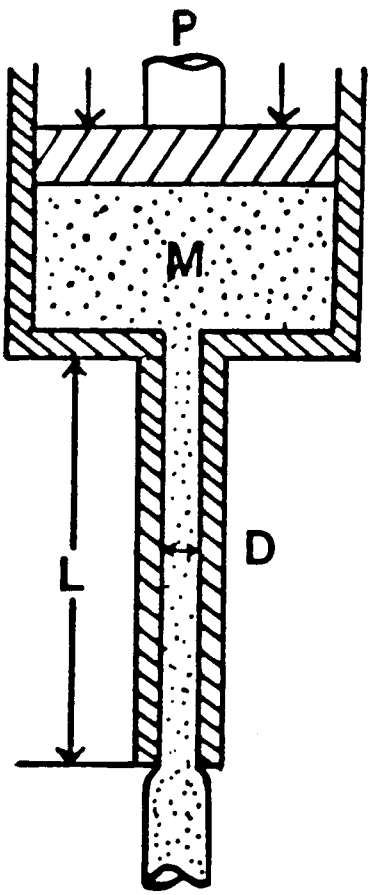

Figure III-3. Capillary viscometer.
P = Plunger
B = Barrel
M = Melt
D = Capillary diameter
L = Capillary length

pointed out by Bagley (2, 3), large "ends" pressure losses are involved in the process, and the effective length of a capillary die is greater than its true length. Thus, we have

$$\Delta P_{total} = \Delta P_{ends} + 4\sigma_{12,w} \frac{L}{D} \qquad [III-5]$$

Therefore, in order to determine $\sigma_{12,w}$, one must obtain data at several L/D ratios and determine it from the slope of a ΔP_{total} versus L/D plot (Bagley Plot).

The shear rate at the capillary wall is given by the Weissenberg equation (29).

$$\dot{\gamma}_w = \frac{32Q}{\pi D^3} \left(\frac{3n' + 1}{4n'}\right) \qquad [III-6]$$

where

$$n' = \frac{d \ ln \ (\sigma_{12,w}}{d \ ln \ (32Q/\pi D^3} \qquad [III-7]$$

and Q = flow rate; L = capillary length; and D = capillary diameter. Two sets of capillaries were used in our studies to measure the total pressure drop. One set had D = 1.47 mm and L/D ratios of 8.7, 20.0, 30.3 and 40.0. The other had D = 2.00 mm and L/D ratios of 10.0, 15.4, 25.7 and 41.0.

Scanning Electron Microscope (SEM) Technique

Scanning electron microscope was used as an auxiliary technique to obtain a qualitative picture of the fiber orientation distribution and possible flow pattern in the

systems investigated. In studying the samples under the scanning electron microscope, use was made of the devices and procedure developed by Patel (89) with minor modifications. The samples were mounted in standard aluminum SEM sample holders by means of a epoxy resin (a 3M epoxy-resin quick set kit was found suitable for our purposes). To ensure that the cross-sectional area of the specimen was perpendicular to the machine direction, a Teflon block was used as a base. This Teflon block had holes drilled in it in such a way that SEM sample holders were allowed to rest inside the block and well below its upper surface. This was done to provide a "mold cavity" where enough epoxy resin could be poured in to hold the specimen in place. Specimens so mounted were allowed to cure for two hours at room temperature and then for another two hours at 80°C to harden the epoxy matrix. The cured specimens were mounted on a SYNTRON (SYNTRON Company, Homer City, PA) polishing wheel sample holder. They were first polished by hand using different grades of sand paper and a polishing wheel with a 9.5-micron slurry. They were then polished on the centron using a 0.06-micron slurry for a period of 12 hours. After polishing, the samples were cleaned in an ultrasonic bath (water and detergent) to remove any polishing compound left on them. Cleaned and rinsed samples were etched with methylene chloride for three minutes under continuous agitation to obtain the contrast between fibers

and matrix. SEM pictures were taken from these samples utilizing an AMR model 900 high resolution scanning electron microscope (Advanced Metals Research Corporation, Burlington, MA). A gold-palladium alloy was used on the specimens to eliminate charging in the electron beam. Figure III-4 shows the kit used to prepare the speciments.

X-Ray Flat-Film Technique

Wide angle x-ray diffraction in the flat-film mode was used to obtain the diffraction pattern of the reinforcing Kevlar 49 fibers, in order to identify and index the reflections observed. This technique was also applied to the composite specimens in order to obtain a qualitative evaluation of the degree of fiber and matrix orientation, if any, developed as a result of the processing conditions and geometry.

Being the purpose of this study to attempt a quantitative evaluation of the degree of fiber orientation in the processed material by means of wide angle x-ray scattering (WAXS) techniques, a reliable and accurate fiber pattern was essential to characterize the reinforcing fibers properly. In order to obtain such a diffraction pattern, use was made of the available continuous Kevlar 49 yarn to prepare a fiber sample as perfect as possible. To do so, the continuous yarn was wound by hand in a large aluminum frame (30 x 30 cm). Each turn was carefully laid next to the previous one, keeping the yarn smooth and under

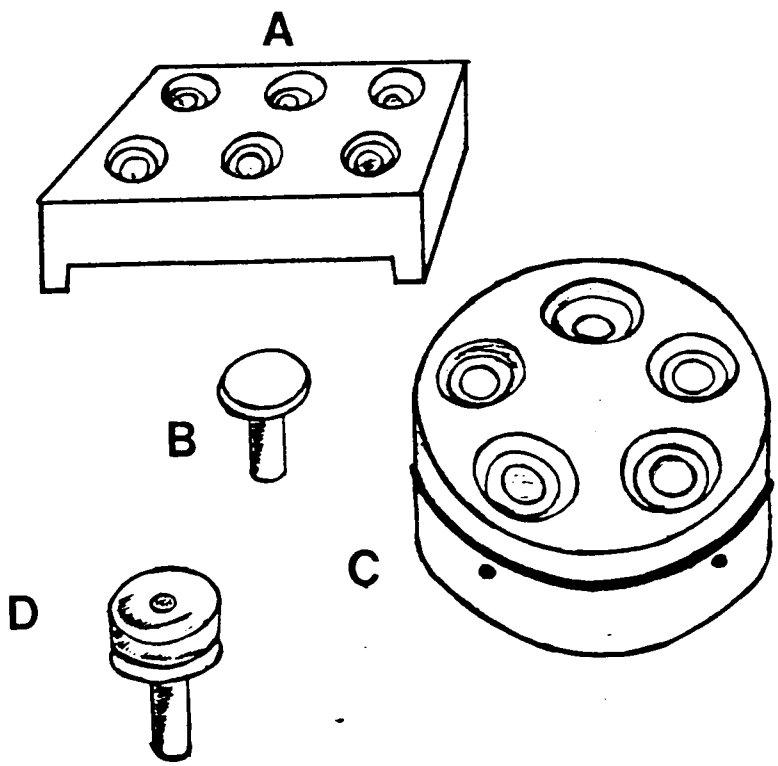

Figure III-4. SEM sample preparation kit.
A, Teflon block
B, SEM sample holder
C, SYNTRON polishing wheel sample holder
D, finished specimen

continuous tension. This procedure was continued until a parallel fiber bundle, about 1.4 cm wide and 0.1 cm in thickness, was obtained. Then, the bundle was brushed with a soft toothbrush to further align the fibers. Finally, a square sample holder (3 x 3 cm), having screws at each corner and a circular aperture (1.6 cm in diameter) in the center, was fixed to the central portion of the fiber bundle and tightened. Epoxy glue was then added to the bundle outside the sample holder, and allowed to cure for a period of eight hours. The bundle was cut along the sample holder edges, yielding an excellent specimen for x-ray diffraction studies of the Kevlar 49 reinforcing fibers. Details of this procedure are shown in Figure III-5. Composite specimens for x-ray flat-film analysis were taken from the processed material with no further preparation.

All x-ray flat-film patterns were obtained using a Philips Norelco x-ray generator and a Statton general purpose camera (W. H. Warhus Company, Wilmington, Delaware). Sample to film distances of 3 and 5 cm were used. Filtered copper radiation ($K\alpha$, λ = 1.5418 Å) was obtained operating the x-ray generator at 30 KV and 20 mA. Exposure times were varied in order to obtain similar film blackening with different specimen thicknesses.

X-Ray Diffractometer Technique

Our main concern in this study has been the development of an x-ray diffractometer procedure to obtain a quantitative

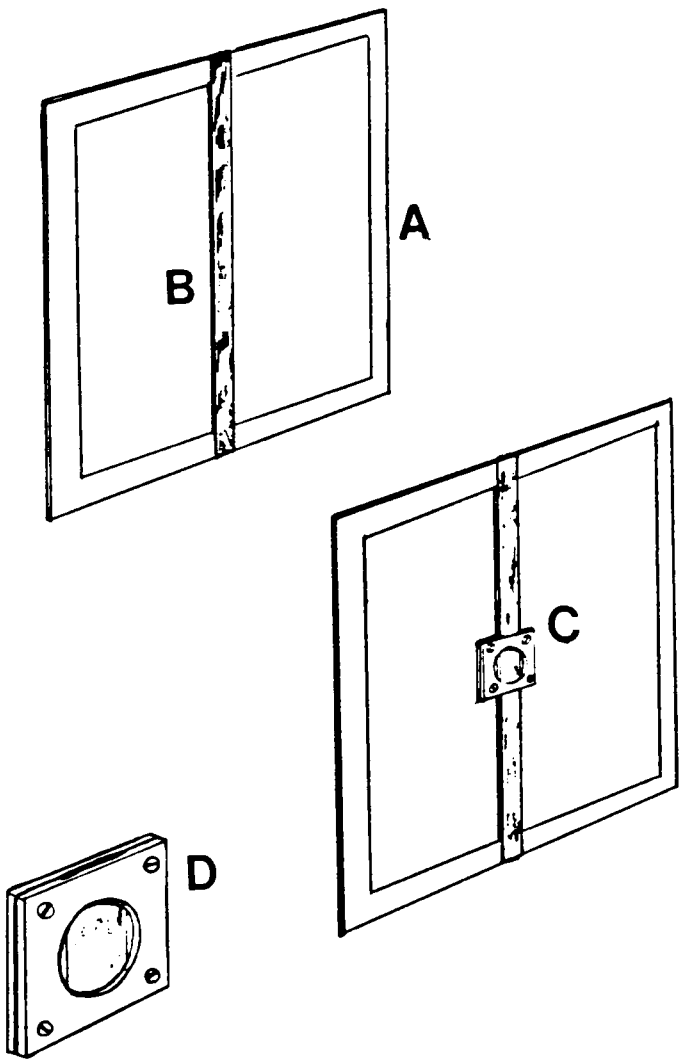

Figure III-5. X-ray fiber pattern sample preparation.
A, Aluminum frame
B, Kevlar 49 fiber bundle
C, Stainless steel fiber sample holder
D, Finished sample (detail).

evaluation of the fiber orientation distribution in a short-crystalline-fiber reinforced amorphous thermoplastic. Such a procedure, as a first approach, is intended to be applied to composite specimens assumed to have radial (fiber) symmetry. Furthermore, it should be reliable enough to obtain a quantitative measure of the fiber orientation distribution in the composite (uniaxial orientation factors) without being too complex for being applied in routine analysis.

Obviously, the main difficulties are those related to the amorphous matrix background which has to be subtracted from the total reflected intensity, as a first step in the calculation of any orientation function. The reliability of any procedure to evaluate the fiber orientation distribution will be affected by the accuracy in removing the amorphous contribution from the total reflected intensity. The approach attempted in this study is based upon the use of amorphous reference standards, whose fully corrected intensity in a unit volume basis is subtracted from the total fully corrected intensity of the composite sample, also in a unit volume basis, in an amount proportional to the volume of amorphous matrix in the composite specimen. The difference so obtained is assumed to represent the total contribution to the reflected intensity due to the reinforcing fibers. Corrections due to fiber background are then applied to these intensity differences, and the

resulting values are used to calculate uniaxial orientation factors as outlined in Chapter II.

Equipment. Two different x-ray diffractometers were used in the development of this study. This was due to limitations on the area of the specimen being irradiated and the necessity of carrying out intensity corrections due to air scattering. However, far from being an inconvenience, this gives interesting results because it allowed a comparison of the effect of instrumental factors in the accuracy of the proposed method. Table III-3 described the characteristics of the x-ray equipment used in this study.

Sample preparation. The fiber standard was that used in the flat-film technique, whose preparation has been described elsewhere. Amorphous PMMA sheet standards were prepared in a hot press. Dried PMMA pellets were pressed at 220°C into 1 mm thick sheets. Square samples (2.54 x 2.54 cm) were cut from the sheets and annealed in an oven at 94°C for four hours. Selected samples were used to determine x-ray linear absorption coefficients of the matrix, μ_p; as reference standard to monitor the intensity fluctuations of the x-ray beam in both diffractometers; and as amorphous layers in a perfect aligned sample prepared with the fiber sample and used to establish the feasibility of the proposed procedure.

Table III-3

X-Ray Equipment Characteristics

Norelco Diffractometer with Pole Figure Device (Philips Electronic Instruments)	Single Crystal Orienter (General Electric Company)
Tube: Cu Filter: N_i	Tube: Cu Filter: N_i
T. O. Angle: 6° KV = 35 μA = 15	T. O. Angle: 6° KV = 40 μA = 15
Monochromator:----------	Monochromator: LiF (Incident beam)
Gon. Radius: 180 mm R.S. Width: 2mm	Gon. Radius: 145.5 mm R.S. Width: 2mm
X-Ray Bean*:	X-Ray Beam*:
2Rα = 1.27 mm 2Rβ = 2 mm y = ------	2Rα = 3 mm 2Rβ = 2 mm y = 4 mm
Detector: Scintillation $N_aI(Tl)$	Detector: Scintillation $N_aI(Tl)$
Voltage: 1140 V	Voltage: 1140 V
P. H. Analyzer:	P. H. Analyzer:
L. L. = 2.5 V H. L. = 7.0 V	L. L. = 1.60 V H. L. = 9.50 V
Amplifier:	Amplifier:
F. Gain = 5.5 C. Gain = 8.0	F. Gain = 5.0 C. Gain - 32

*At the specimen site.

Composite pellets were also hot-press-molded to obtain samples used in determining the x-ray linear absorption coefficient, μ_c, of the composite material. Because of the necessity of carrying out intensity absorption corrections in the symmetrical-transmission geometry and the radial symmetry of processed composite specimens, spherical shaped specimens were required. These samples were prepared as follows:

(a) Extrudate samples. Samples were prepared by grinding the extrudates mounted in an electrically rotated holder under a magnifying glass. In each case, the extrudate diameter became the diameter of the spherical sample. Reference amorphous specimens were obtained from pure PMMA extrudates processed under similar conditions and geometry as those of the composite specimens. All extrudate spherical samples were prepared paying especial attention to match as accurately as possible the shape and dimensions of each couple of samples (composite-amorphous standard) including the mounting procedure for x-ray analysis.

(b) Samples from material frozen inside the die. A special set of samples was prepared from material frozen inside the die after cooling down the capillary rheometer. The frozen material inside the die was carefully removed and divided into three segments. Then, a spherical sample was prepared from the central part of each segment as described for the extrudate samples. Reference amorphous

standards were also prepared from pure PMMA frozen inside the die in an analogous manner.

(c) Samples from material frozen inside the rheometer barrel. Frozen material inside the rheometer barrel was carefully extracted using the plunger and a low cross-head speed (2.5 mm/min). A sample was prepared from this material at approximately 1 cm above the die entrance. The diameter of the sample matched that of the extrudate specimen obtained under the same flow conditions. Considerable grinding was required to prepare this sample because of the initial diameter (9.5 mm). A similar procedure was followed to prepare the reference amorphous sample. Details of the preparation and mounting of the spherical samples for x-ray analysis are shown in Figure III-6.

Intensity measurements. All intensity measurements were recorded on a teletype attached to the electronic circuit panel of the x-ray generator. In order to measure the total intensity with statistical accuracy, enough pulses were counted to keep the standard deviation within less than 1 percent. In no case was a total count of less than 10^4 pulses registered, and average values were as much as four times this amount.

When events are occurring randomly in time sequence, the standard deviation, σ, of the number of events observed N from the true average number N_o is given by (61)

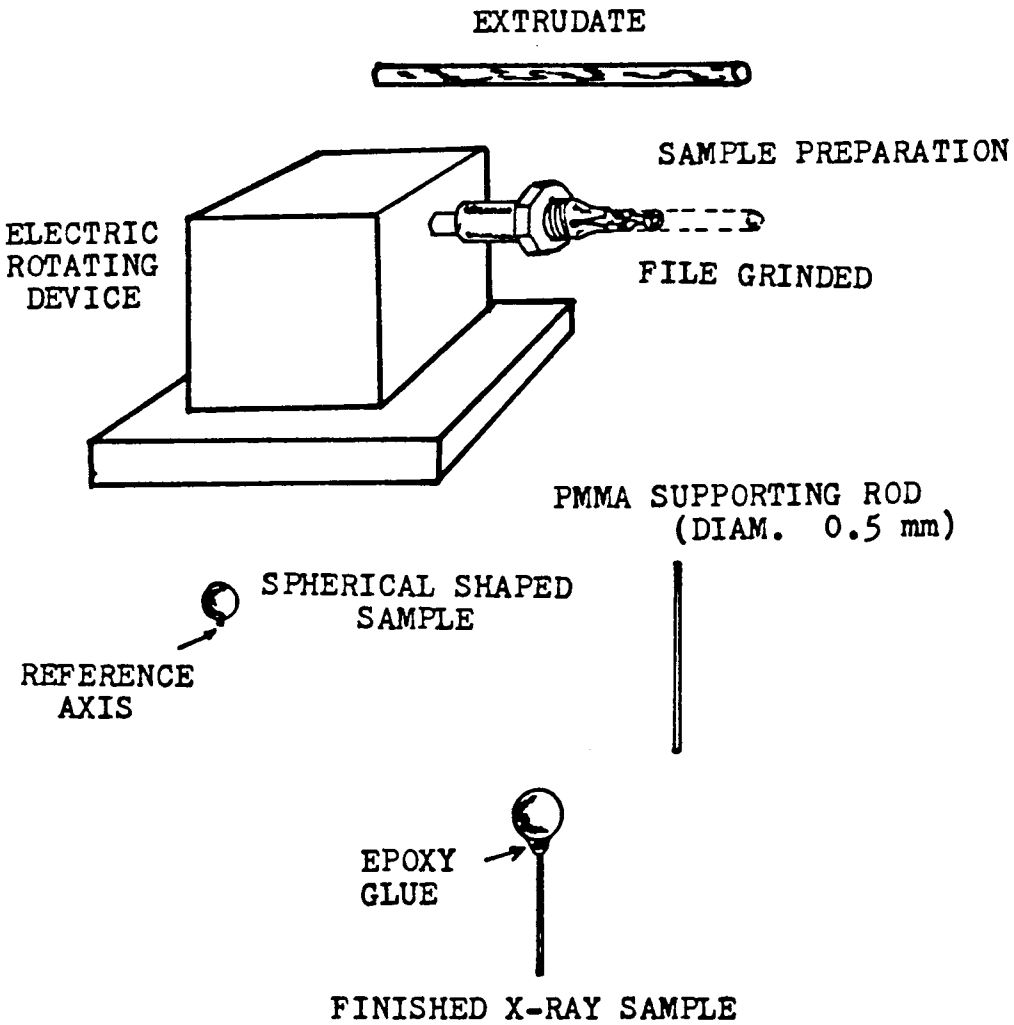

Figure III-6. Spherical sample preparation and mounting.

$$\sigma_N = N^{1/2} \qquad [III-8]$$

and the relative standard deviation is

$$\sigma_{N(rel)} = \frac{N^{1/2}}{N} = N^{-1/2} \qquad [III-9]$$

Thus, a total count averaging 4×10^4 pulses keeps the relative standard deviation at a value of 0.005.

Reduction of intensity data. The corrections applied to the intensity diffracted by each sample and recorded in the teletype include all the following: a) cosmic x-ray background, b) x-ray energy fluctuations, c) air scattering, d) sample absorption, and e) Lorentz-Polarization effects. No correction was applied for incoherent radiation or temperature fluctuations in the specimens.

(a) Cosmic background. Before and after each sample analysis, a 500-600 sec count was carried out with the x-ray shutter closed to find the average cosmic background count per unit time (sec). The respective value of background intensity was then subtracted from the recorded intensity of each sample as the first correction.

(b) X-ray tube fluctuations. A standard sample of amorphous PMMA, mounted in a special sample holder and carefully marked to be located at exactly the same position with respect to the x-ray beam, was utilized to monitor the main beam at the beginning and end of each run. A 2θ value

of 13.5°, corresponding to the setting for the principal amorphous halo, was set in the diffractometer. Counts of 500-600 sec were accumulated to obtain the average intensity of the x-ray during each run. The first average determined during the evaluation of the air scattering was taken as reference, and subsequent averages were compared to it to determine an intensity correction factor (K) to be applied to the recorded intensities in each run. This factor is defined as follows:

$$K = \frac{I^{\circ}_{av}}{I^{n}_{av}} \qquad \text{[III-10]}$$

where I°_{av} = first intensity average recorded during air scattering determination, I^{n}_{av} = intensity average recorded for run n.

(c) Air scattering. For this correction, we followed the treatment given by Ergun (33) for the case of a flat speciment of thickness T in symmetrical-transmission geometry. Figure III-7 shows the geometry involved in the analysis, which leads to the following relationship:

$$At_f = \left(\frac{T \sin \theta}{R\beta}\right) \exp\left(\frac{-\mu T}{\cos \theta}\right) \qquad \text{[III-11]}$$

where At_f = ratio of the scattered intensity received with and without the flat sample in place, R = goniometer radius, 2β = equatorial angle (in radians) subtended at the specimen by the receiving slit (see Figure III-7).

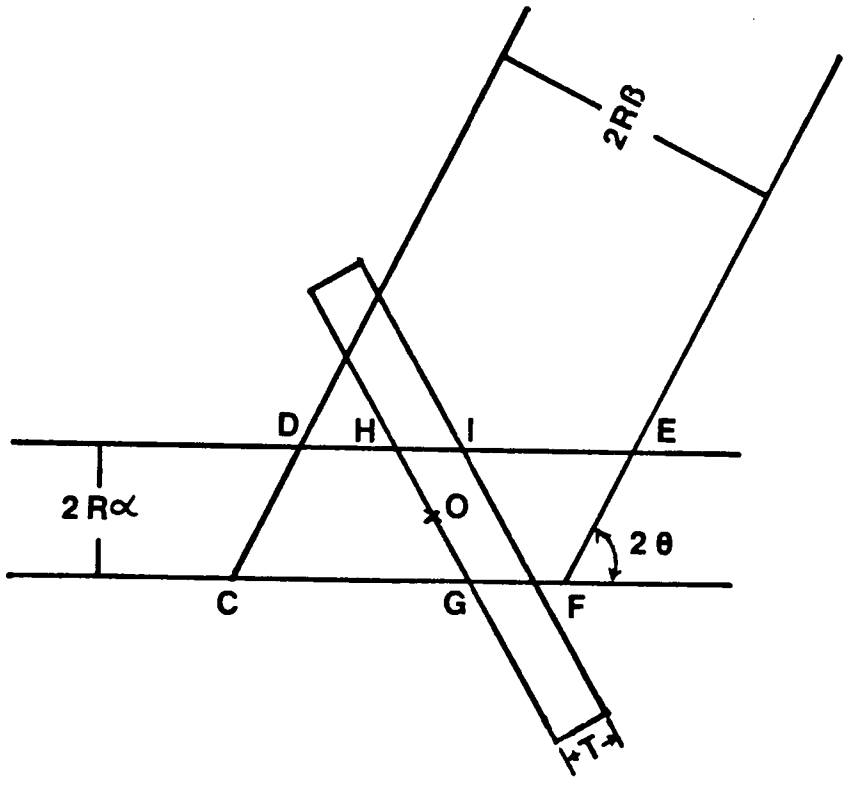

Figure III-7. Cross section of the scattering air volume and the sample. Symmetrical-transmission geometry [after Ergun (33)].

In the case of a spherical sample in symmetrical-transmission geometry, Equation III-11 has been modified as follows:

$$At_S = \left[1 - \frac{V_S \sin 2\theta}{(2R\alpha)(2R\beta)y}\right] \left[\frac{1}{V} \int \exp[-\mu(p + q)]\, dV\right]_{2\theta} \qquad [III\text{-}12a]$$

or

$$At_S = \left[1 - \frac{V_S \sin 2\theta}{R^2(2\alpha)(2\beta)y}\right] A_{2\theta} \qquad [III\text{-}12b]$$

where At_S = ratio of the scattered intensity received with and without the spherical sample in place, R = goniometer radius, 2α = equatorial divergence (in radians) of the x-ray beam at the specimen, 2β = equatorial angle (in radians) subtended at the specimen by the receiving slit, y = actual height of the beam at the specimen, V_S = volume of the spherical sample contained within the receiving slit width, and $A_{2\theta}$ = transmission factor for a sphere bathed by a uniform x-ray beam (53). Equations III-12a and III-12b can be easily derived following Ergun's reasoning in deriving Equation III-11 for a flat sample.

The magnitude of the air scattering with the specimen in place is obtained by measuring the air scattering in the absence of the specimen and then multiplying the result by Equations III-11 or III-12a,b.

(d) Correction for absorption by the sample. For symmetrical-transmission geometry with a flat specimen, the

following correction is to be applied (98, 101, 104) to all intensities measured at $2\theta > 0°$.

$$\frac{I_{o°}}{I_{2\theta}} = \frac{\exp[-\mu T(1 - \sec\theta)]}{\sec\theta} \qquad \text{[III-13]}$$

For spherical samples in symmetrical-transmission geometry, the absorption correction is given by

$$\frac{I_{o°}}{I_{2\theta}} = \frac{[1/V \int \exp[-(p + q)\mu]\, dV]_{2\theta=0}}{[1/V \int \exp[-(p + q)\mu]\, dV]_{2\theta=0°}} = \frac{A_{o°}}{A_{2\theta}} \qquad \text{[III-14]}$$

where $A_{o°}$ and $A_{2\theta}$ are tabulated in the literature (104).

(e) Lorentz-Polarization effects. The x-rays emitted by an x-ray tube are considered to be unpolarized. However, interaction of the x-ray beam with the specimen yields a diffracted beam which is plane polarized to a degree that is a function of the Bragg angle θ (1, 61). Thus, the polarization factor for a randomly polarized incident beam is

$$P = \frac{1 + \cos^2 2\theta}{2} \qquad \text{[III-15]}$$

When use is made of crystal-monochromatized radiation, the polarization factor becomes

$$P = \frac{1 + \cos^2 2\theta' \cos^2 2\theta}{1 + \cos^2 2\theta'} \qquad \text{[III-16]}$$

where θ' = Bragg angle for the reflecting planes of the monochromator.

The Lorentz factor corrects the diffracted intensity for chromacity and divergence effects of the x-ray beam, and for any motion imparted to the sample affecting the reflecting time or ability to reflect of the reflecting planes (61). Given the composite nature of the specimens, we have followed the practice of applying the Lorentz factor in the form

$$L = \frac{1}{\sin \theta \cos \theta} \qquad \text{[III-17]}$$

Equations III-15 and III-16 can be combined with Equation III-17 to give the so-called Lorentz-Polarization factor for each type of x-ray radiation. Thus, we can write

$$L - P = \frac{1 + \cos^2 2\theta}{\sin 2\theta} \qquad \text{[III-18]}$$

for a randomly polarized incident beam, and

$$L - P = \frac{1 + \cos^2 \theta' \cos^2 2\theta}{(1 + \cos^2 \theta')(\sin \theta \cos \theta)} \qquad \text{[III-19]}$$

for a crystal monochromatized incident beam.

All recorded intensities are normalized to the reference level by multiplying them by the reciprocal of Equation III-18 or III-19.

The final expression for the corrected intensities after applying all of the above corrections to the recorded intensities is given by

$$I_C = [(I_R - I_{CB})\ K - I_{air}]\ (\frac{I_{o^\circ}}{I_{2\theta}})(\frac{1}{L - P}) \qquad [III-20]$$

where I_R = recorded intensity, I_{CB} = average cosmic-background intensity, I_{air} = intensity of air scattering obtained from the instrument air-scattering curve and Equation III-11 or III-12a,b.

Procedure for evaluating amorphous PMMA contribution to the corrected intensities. The corrected intensities as given by Equation III-20 are referred to $2\theta = 0°$ by the absorption correction $I_{o^\circ}/I_{2\theta}$. Furthermore, all corrected intensities for the same Bragg angle will depend only on the azimuthal angle θ (or χ) because of radial symmetry. Therefore, it is reasonable to represent the total intensity diffracted by a sample at the same Bragg angle as

$$I_{C_\phi} = I_{o_\phi}\ V \exp(-\mu T) \qquad [III-21]$$

for a flat specimen, and

$$I_{C_\phi} = I_{o_\phi}\ VA_{o^\circ} \qquad [III-22]$$

for a spherical specimen.

In Equations III-21 and III-22, I_{o_ϕ} represents the intensity diffracted by unit volume of the specimen at the angle ϕ under the hypothetical case of no absorption. In the case of a composite specimen, this intensity will be given by the contributions of each one of the components

making up the specimen. Such a contribution will be dependent on the volume fraction of each specimen being present and on the intensities per unit volume diffracted by each of them. Thus, it is reasonable to assume I_{o_ϕ} as given by

$$I_{o_{\phi 1}} \bar{V}_1 + I_{o_{\phi 2}} \bar{V}_2 = I_{o_\phi} \qquad \text{[III-23]}$$

where $I_{o_{\phi 1}}$ and $I_{o_{\phi 2}}$ are the intensities diffracted per unit volume of component 1 and component 2 making up the specimen, and $\bar{V}_1$ and $\bar{V}_2$ are their respective volume fractions.

Equation III-23 can be recast as

$$I_{o_{\phi 1}} V_1 + I_{o_{\phi 2}} V_2 = I_{o_\phi} V \qquad \text{[III-24]}$$

where V_1 and V_2 are the respective volumes of each component in the sample.

It is known that the mass absorption coefficient (μ/ρ) for a compound of known composition can be calculated from the expression (1)

$$\frac{\mu}{\rho} = \sum_i \bar{M}_i \left(\frac{\mu}{\rho}\right)_i \qquad \text{[III-25]}$$

where $\bar{M}_i$ and $(\mu/\rho)_i$ are the mass fraction and the mass absorption coefficient, respectively, of component i.

From Equation III-25 and the definition of density $(\rho = M/V)$, it follows that

$$\mu V = \mu_1 V_1 + \mu_2 V_2 \qquad \text{[III-26a]}$$

and

$$\mu T = \mu_1 T_1 + \mu_2 T_2 \qquad \text{[III-26b]}$$

for a component compound.

Now, substituting Equations III-24 and III-26a into Equation III-21 gives for a flat specimen

$$(I C_\phi)_{comp} = (I_{o\phi 1} V_1 + I_{o\phi 2} V_2) \exp -(\mu T_1 + \mu T_2) \qquad \text{[III-27]}$$

This equation gives the relationship between the actual corrected diffracted intensity of a composite specimen, $(I C_\phi)_{comp}$, and the diffracted intensities per unit volume of each of its components under the theoretical condition of no absorption ($I_{o\phi 1}$ and $I_{o\phi 2}$).

Assuming $I_{o\phi 1}$ and $I_{o\phi 2}$ being independent of each other, they can be related to the respectives corrected diffracted intensities of each component by

$$(I C_\phi)_1 = I_{o\phi 1} V_1 \exp(-\mu_1 T_1) \qquad \text{[III-28a]}$$

$$(I C_\phi)_2 = I_{o\phi 2} V_2 \exp(-\mu_2 T_2) \qquad \text{[III-28b]}$$

Solving Equations III-28a and III-28b for $I_{o\phi 1}$ and $I_{o\phi 2}$, respectively, substituting into Equation III-27 and rearranging yields

$$\frac{(I C_\phi)_{comp}}{\exp(-\mu T)} = \frac{(I C_\phi)_1}{\exp(-\mu_1 T_1)} + \frac{(I C_\phi)_2}{\exp(-\mu_2 T_2)} \qquad \text{[III-29]}$$

where $(I_{C_\phi})_1$ and $(I_{C_\phi})_2$ are the corrected diffracted intensities which would be obtained from the pure components having volumes V_1 and V_2, respectively.

When a pure component specimen has an irradiated volume different from that present in the composite, the resulting corrected diffracted intensity has to be multiplied by the respective volumetric ratio in order to satisfy Equation III-29.

In this study, the amorphous PMMA contribution to the total corrected diffracted intensity from the composite is taken to be equal to the corrected diffracted intensity from a PMMA specimen processed under the same conditions and having the same volume as the composite specimen, times the volume fraction of the PMMA content in the composite. The crystalline fiber contribution is then obtained from Equation III-29 as

$$\frac{(I_{C_\phi})_F}{\exp(-\mu T)_F} = \frac{(I_{C_\phi})_{comp}}{\exp(-\mu T)_{comp}} - \frac{(I_{C_\phi})_{PMMA}}{\exp(-\mu T)_{PMMA}} \bar{V}_{PMMA} \qquad [III-30]$$

$(I_{C_\phi})_F/\exp(-\mu T)_F$ values for the azimuthal range (0-90°) at proper 2θ values are then treated as the corrected diffracted intensities for the pure fiber which, after correction for fiber background, are used to calculate the fiber orientation factors.

In case of the spherical samples, the exponential transmission factors which appear as denominator in each

term of Equation III-30 are substituted by the respective transmission factors $(A_o°)_{comp}$, $(A_o°)_F$, or $(A_o°)_{PMMA}$ for spherical samples (53).

Experimental results of the use and reliability of Equation III-30 in our study will be treated in the following chapter.

CHAPTER IV

FLOW PROPERTIES

Results of rheological studies carried out in both the pure and fiber-filled melts are summarized in this chapter. The shear viscosity (η), the first normal stress difference and the influence of fiber length on the flow behavior of the fiber-filled melt are discussed.

A. SHEAR FLOW MEASUREMENTS

Shear flow measusements at high shear rates were carried out in an Instron Capillary Rheometer and at low shear rates in a Mechanical Spectrometer. The range of measurable shear rates in each instrument is limited. Lower shear rate limits are due to the sensitivity of the load transducer utilized. Upper limits are established by the development of flow instabilities in the melt such as extrudate distortion, secondary flow and edge failure.

End Effects

The contribution of the end of the capillary to the total pressure drop (ΔP_{total}) may be large and it is very important to use a reliable method to correct these effects.

In each system investigated, measurements of the total pressure drop at different volume flow rates were carried out for a set of four dies having the same diameter (D) but

different L/D ratios. For each system, ΔP_{total} values were plotted against L/D ratios (Bagley plots) as shown in Figures IV-1, IV-2 and IV-3. It should be noted that there was no evidence of melt fracture for any of the systems investigated in the shear rate range covered in the capillary rheometer.

Figure IV-1 shows the Bagley plot for the pure PMMA melt at 220°C, using capillaries having a diameter of 1.47 mm and L/D ratios of 8.7, 20.0, 30.3 and 40.0, respectively. All data points were taken having the same height of material in the rheometer barrel and using a new load every time. Plotted data are averages of at least two different runs. Reproducibility of data values was very good, usually within a ±5 percent. A slight departure from linearity can be observed for the higher shear rates in this plot.

Figure IV-2 shows the respective Bagley plot for the system reinforced with the commercially available Kevlar 49 staple fiber (6.35 mm in length) with the same set of capillaries and under the same experimental conditions as those described for the pure PMMA melt. In this case, the non-linear behavior is more evident at the higher shear rates, decreases with the rate of shear and, finally, becomes linear at the lower shear rates.

The corresponding Bagley plot for the system reinforced with the short Kevlar 49 fibers cut out of the yarn (mean

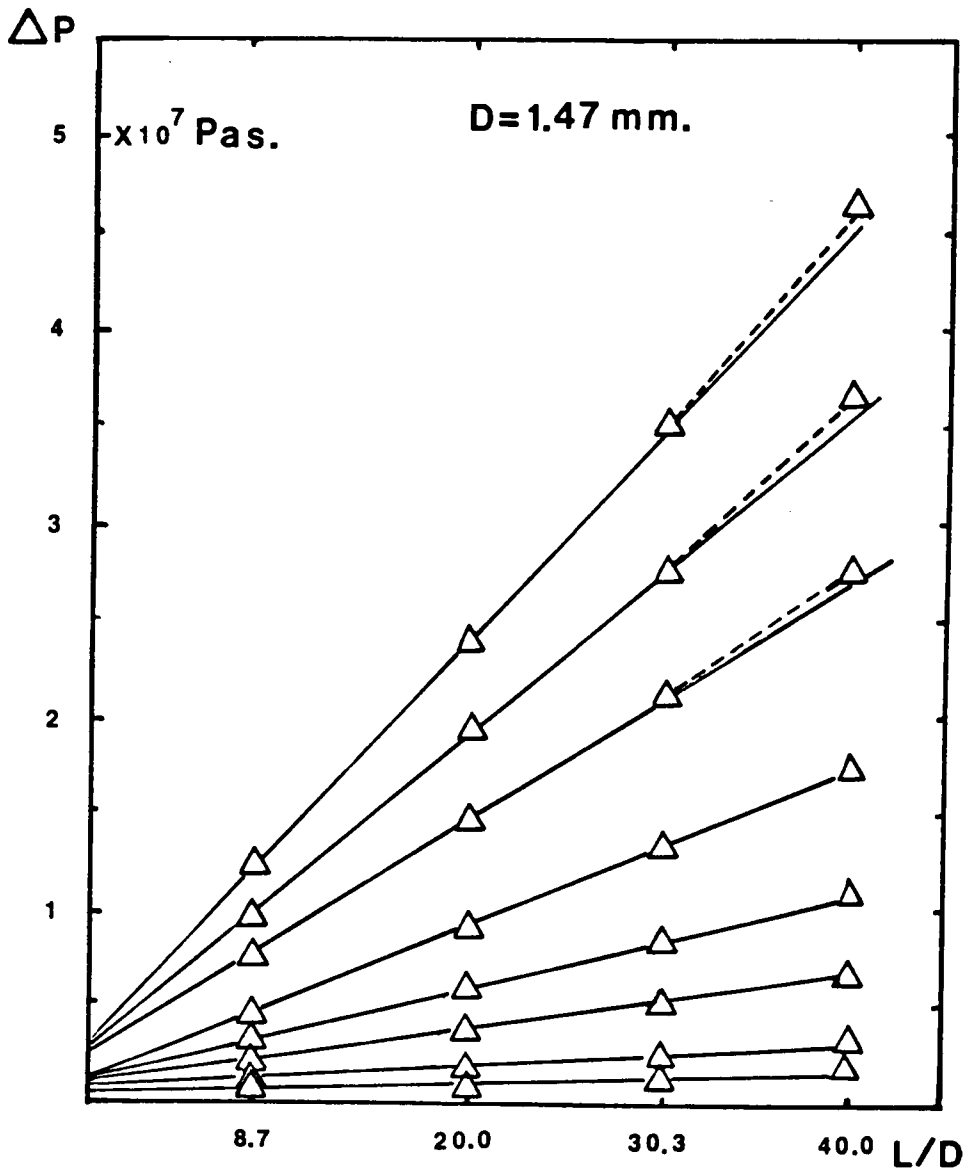

Figure IV-1. Bagley plot for the pure PMMA melt.

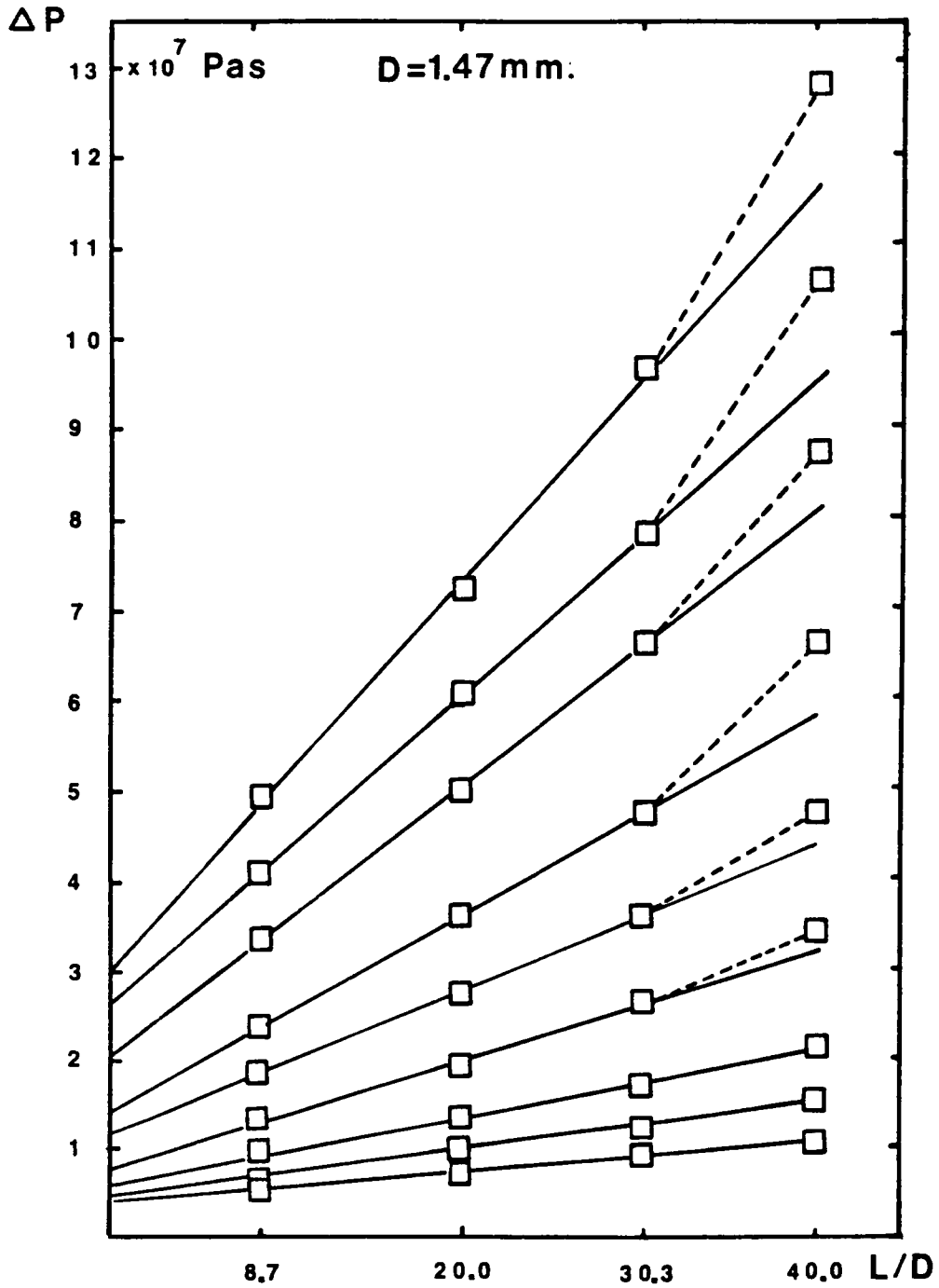

Figure IV-2. Bagley plot for the PMMA melt filled with the commerical Kevlar 49 staple fiber.

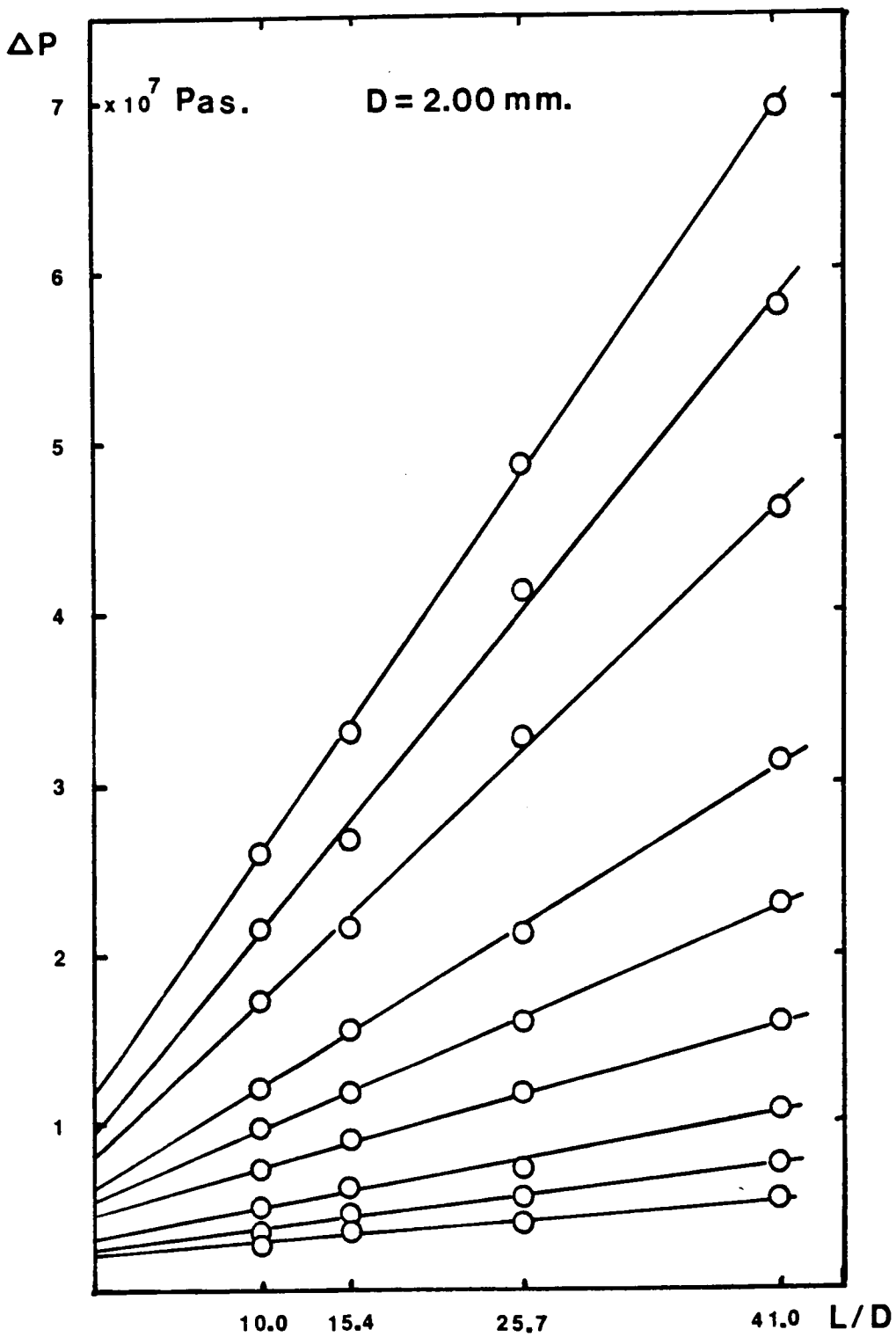

Figure IV-3. Bagley plot for the PMMA melt filled with the short Kevlar 49 fibers obtained from the continuous yarn.

fiber length = 1.18 mm) is shown in Figure IV-3. In this case, a set of capillaries having a diameter of 2.00 mm and L/D ratios of 10.0, 15.4, 25.7 and 41.0 was used. All other experimental conditions are the same as those for the pure PMMA melt. A linear behavior is observed throughout the whole range of shear rates measured with this system.

Shear Viscosity

Figure IV-4 shows the shear viscosity (η) as a function of the shear rate for the three systems described above. Data on the low shear range for the pure PMMA melt were obtained using the cone and plate geometry. Low shear viscosity data for the two fiber-filled systems were not possible to obtain. Attempts were made in both cone and plate and parallel plate geometries without success. Flow instabilities kept the sample coming out of the gap between the stationary plate and the rotating cone (or plate) even at very low shear rates. The system filled with the commercial staple fiber showed higher instability than that filled with the shorter fibers cut out of the continuous yarn.

From Figure IV-4, it is seen that the aramid fibers increase the level of the shear viscosity, with greater increases occurring at lower shear rates. It is also observed that the system filled with the commercial staple fiber exhibits a higher shear viscosity than the system filled with the short fibers from the yarn. This increase

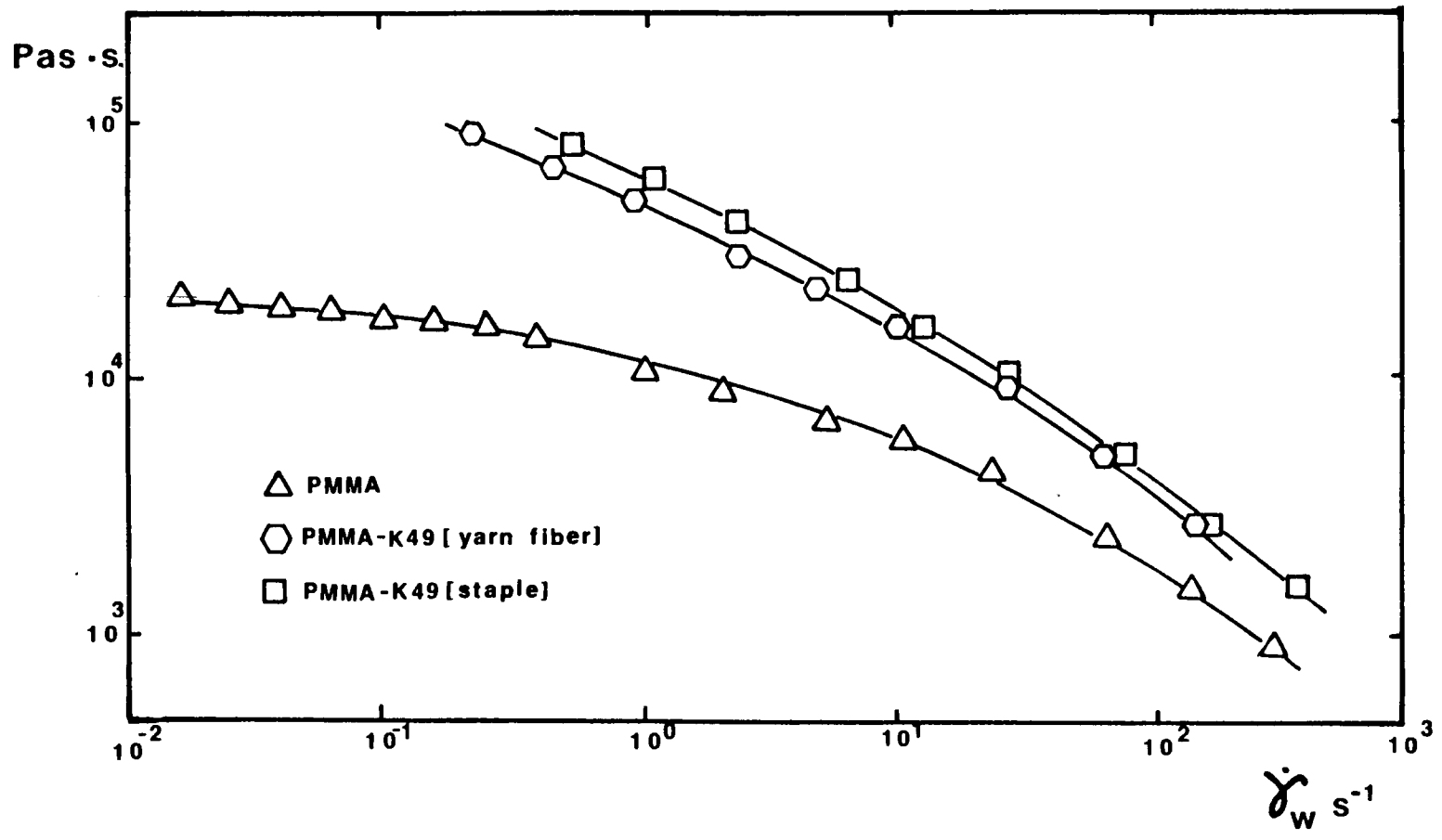

Figure IV-4. Shear viscosity (η) as a function of shear rate ($\dot{\gamma}$) for the three systems investigated at 220°C.

in viscosity with differences in fiber length increases towards the low shear rate range. It should be mentioned that in all measurements where the fiber length exceeded the capillary diameter pressure fluctuations were observed during flow. In these cases, the mean values of pressure drop were determined from the area under the force curve in the recorder chart using a planimeter.

Principal Normal Stress Difference

In spite of our efforts to obtain flow measurements in the low shear region for the fiber filled systems using the Mechanical Spectrometer, that was not possible. It should be noted that in the case of the system filled with the commercial staple fiber, all attempts to measure the normal force were accompanied by a continuous increase in the magnitude of the normal force during the initial part of the experiment. As this progressed, the increase in normal force was counterbalanced by the amount of material coming out of the gap between cone and plate without reaching a staple condition. This behavior could be possibly due to the large aspect ratio of the reinforcing fibers which led to fiber entanglement in the sheared material and increased the thrust being measured. This assumption is supported by the fact that the continuous increase in normal force was not observed in the system filled with the short fibers obtained from the continuous yarn, where flow instabilities other than physical

entanglement of the reinforcing fibers were the factors affecting the low shear measurements.

Figure IV-5 shows the principal normal stress difference N_1 as a function of shear stress for the pure PMMA melt. These data points were calculated from the mean values of the normal force determined by integration of the area under the normal force curve in the recorder chart, because of force fluctuations observed in the pure melt.

B. DISCUSSION OF RESULTS

End Effects

Different explanations have been given to account for the non-linearity of Bagley plots in pure polymer melts (28, 69, 107).

Duvdevani and Klein (28) and Thomas and Hagan (107) have interpreted the non-linearity of their Bagley plots as an effect of pressure dependent viscosity. Based upon this approach, an increase on L/D ratio requires a larger pressure in order to produce a given shear rate. This increase in pressure can lead to an increase in viscosity, so that the polymer melt in the entrance region of a capillary having a large L/D ratio will be larger than that in a capillary having a small L/D value at the same volume flow rate. Penwell and Porter (10, 91, 92) have used the WLF equation, derived from the Doolittle free volume theory, and the shifting of the glass transition temperature, T_g,

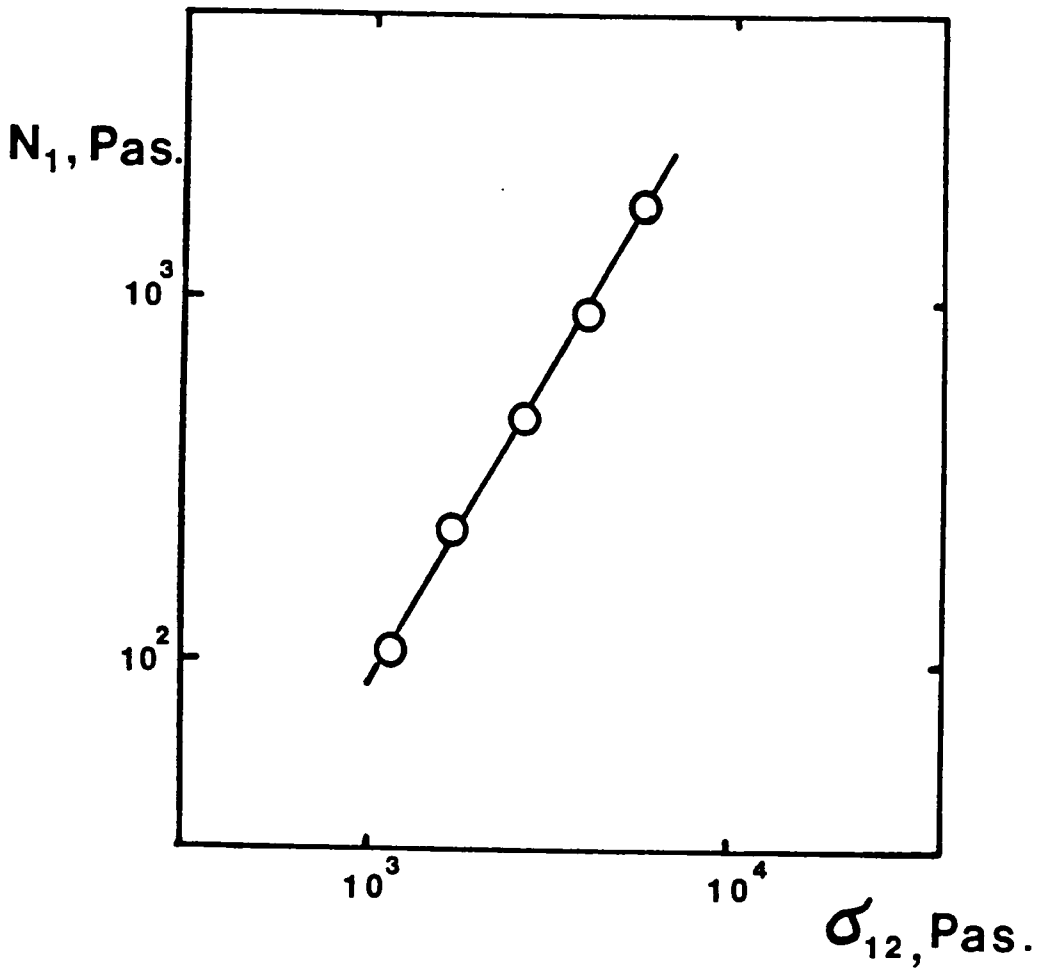

Figure IV-5. Principal normal stress difference N_1 as a function of shear stress σ_{12} for the PMMA melt.

with increasing pressure to correct their experimental data for the pressure effect. They have produced linear Bagley plots for polystyrene (92) and polymethylmethacrylate (10) near their T_g's.

A different approach has been suggested by McLuckie and Rogers (70). They considered the dimensionless number N in the Bagley equation (2) to be constituted of both a geometrical end correction and a second component equal to half of the recoverable shear strain at the capillary wall. Die swell was used as a measure of the recoverable shear strain in their studies.

Chan et al. (14) have reported a fundamental study of the rheological properties of glass-fiber filled high-density polyethylene and polystyrene melts. They have used Bagley plots to determine shear stresses at the capillary wall in their systems without observing any anomalous behavior. However, Crowson, Folkes and Bright (23) have observed non-linear Bagley plots, under some conditions, during their rheological measurements involving pure and short glass-fiber reinforced polypropylene melts. The non-linearity observed in both the pure and filled PP melts is analyzed in the light of the interpretations suggested above. Since the fiber filled and unfilled polypropylene melts showed die swells of a very different magnitude, and since both materials exhibit non-linear Bagley plots in their results, Crowson et al. do not consider the approach

given by McLuckie and Rogers (70) to be appropriate for their materials. Also, because of the non-linear Bagley plots in both materials, they do not consider fiber orientation effects to be responsible for this behavior. Therefore, they consider as more reasonable to explain their data in terms of a pressure dependent viscosity.

A slightly non-linear behavior in our Bagley plots for the unfilled PMMA matrix at the higher shear rates was observed. Because of the absence of melt fracture effects and considering the approaches suggested above, it is reasonable to consider the pressure effect as an explanation of the non-linear behavior observed in our data for the unfilled melt.

In the case of filled PMMA melts, our results show two different behaviors. Bagley plots for the melt filled with the commercial fibers are non-linear except at the very low shear rates. On the other hand, linear Bagley plots are obtained for the melt reinforced with the short fibers cut out of the continuous yarn. No melt fracture effects were observed in any case. To explain these results, it is necessary to consider our experimental conditions in detail. Pressure effects on the pure PMMA melt are very small, only observed at the higher shear rates and detected as a result of careful experimental conditions with the set of capillaries used to characterize the unfilled melt. As can be seen from Figure IV-5, the higher shear

rates measured in the pure melt are larger than those measured in the short-fiber filled melt, which, together with the considerations above, accounts for the absence of non-linear behavior in the short-fiber filled PMMA melt. Furthermore, the modal length of the reinforcing fibers in this material is 1.18 mm, which is well below the 2.00 mm diameter of the capillaries used to characterize the material. Thus, it can be seen, that the presence of fibers does not produce non-linear Bagley plots when the fiber modal length is smaller than the diameter of capillaries used to characterize the material rheologically.

The non-linear behavior of the commercial-staple-fiber filled PMMA melt can be explained as a result of the reinforcing fibers. This can be seen if we consider again the details in the experiments. Pressure effects in the pure melt are too small to account for the fairly large effects observed in the filled melt at the same shear rates (see Figures IV-1 and IV-2, pp. 85, 86). Thus, these effects are due to the presence of fibers in the material. In this system, the modal fiber length is 6.35 mm, which is far in excess of the 1.47 mm diameter of the set of capillaries used to study the material. Therefore, unless the fibers are almost perfectly aligned in the flow direction at the capillary entrance, an additional pressure will be required to force the filled melt into and through the capillary. Orientation development studies carried out in

this system (see Chapter VI) showed a high degree of fiber disorder in capillary flow, which supports the suggested approach given above. This fiber-induced pressure effect increases with increasing shear rates and, obviously, it also depends on the length of the capillaries used in the rheological characterization of the material.

Shear Viscosity

The behavior of the PMMA melt shown in Figure IV-4 (p. 89) is typical, with the viscosity practically constant at low shear rates (Newtonian behavior) and then decreasing at higher shear rates (pseudoplastic behavior). The general shape of the viscosity function for the fiber filled melts is similar to that obtained by different investigators in short glass fiber polymer melts (14, 15, 22, 88, 106). The increase in viscosity due to the added fibers is larger at low shear rates than at high deformation rates. The non-Newtonian behavior is also increased by the presence of fibers. The results in the high shear rate range measured show an analogous behavior to that reproted by Czarnecki and White (24) for polystyrene melts filled with cellulose-, aramid-, and glass fibers, respectively, in the low shear rate range. They observed that the addition of fibers to a polymer melt increases the viscosity in the same manner as a reduction in temperature and viscosity data may be superposed by reduced plotting. This supported the idea that the enhanced viscosity is due to

increased viscous dissipation in the matrix and that particle-particle interaction is not significant. Although experimental difficulties did not allow the study of our filled systems in the low shear rate range, similarities in composition and behavior as shown in Figure IV-4 (p. 89) make it reasonable to assume the approach of Czarnecki and White to account for the viscosity increase in the high shear rate range.

The effect of fiber length in the viscosity of fiber suspensions has been the subject of very few studies. Maschmeyer and Hill (72) working with suspensions of glass fibers in high viscosity silicone oils, showed that a small amount of long fibers could produce a noticeable increment in the viscosity at constant overall fiber concentration. Crowson and Folkes (22) studied the effect of fiber length in the high shear rate range viscosity of short glass-fiber filled polypropylene melts. They found that at high rates of deformation (above about 100 sec^{-1}) there is very little change in viscosity with fiber length, but significant increments in viscosity can be expected at lower shear rates with longer fiber length distributions. This tendency is observed in our results for the two aramid-fiber filled PMMA melts shown in Figure IV-4 (p. 89). Czarnecki and White (24) have also reported a similar effect on the low shear range viscosity of glass- and aramid-fiber filled PS melts as a result of fiber damage during mixing and

mastication. They have shown that fibers may be damaged during mixing into polymer melts or from subsequent mastication during processing. The character and extent of damage was shown to vary with polymer type and was found more severe for the glass fibers. Glass fibers broke down rapidly to small aspect ratios, while aramid (Kevlar 29) showed a kinked structure, with kinks every 100 μm. Thus, the effects on viscosity caused by fiber damage can be compared to those produced by an actual reduction in the fiber length distribution of the reinforcing fibers, and the viscosity of short fiber filled melts can be expected to decrease with reduction in fiber length distribution along the whole shear rate range, this reduction being larger at the low shear rate end and showing little variation with shear rate at high deformation rates.

Principal Normal Stress Difference

As pointed out previously, no data were obtained in the low shear rate range for the fiber-filled systems investigated in this study. Measurements of the principal normal stress difference could be carried out only for the pure melt and within a limited shear rate range because of flow instabilities in the gap between cone and plate, which caused the melt to exit the gap. Results of these measurements are plotted on Figure IV-5 (p. 92) as a function of shear stress σ_{12}. They show that N_1 increases with both

shear rate and shear stress and are similar to those reported by Czarnecki and White (24) for a PS melt.

In spite of the lack of success in measuring normal stress effects in our two aramid-fiber-filled PMMA melts, reference has to be made to the results reported by Chan et al. (14), Czarnecki and White (24) and Knutsson, White and Abbas (62) regarding shear flow normal stresses in fiber filled melts. These investigators have found that shear flow normal stresses are increased by the presence of fibers in the polymer melt. Chan et al. have proposed a mechanism for the large nromal stresses observed in fiber-filled polymer melts. This mechanism is considered to be due to the additive (perhaps synergestic) effect of normal stress effects induced by the viscoelastic continuous phase, and the fiber induced phenomena described by Nawab and Mason (80), and others (71, 74) for suspension of fibers in Newtonian fluids. Czarnecki and White (24) have also correlated the principal normal stress difference N_1 for the glass-, aramid-, and cellulos-fiber filled polymer melts as a function of shear stress σ_{12}. Their plots are of great interest because they show the relative influence of the fibers on the principal normal stress difference and the shear stress and not the influence of N_1 alone. In these plots, it is seen that N_1 increases with both shear rate and shear stress. Mastication effects are shown to reduce N_1 more rapidly than σ_{12}.

Considering the similarities between our aramid (Kevlar 49)-filled melts and the aramid (Kevlar 29)-fiber filled PS melt investigated by Czarnecki and White (see preceeding section), it seems reasonable to expect that the influence of the fibers on the principal normal stress difference and the shear stress will be similar in all three systems. However, actual experimental data is required to confirm those assumptions.

CHAPTER V

CALIBRATION OF WAXS TECHNIQUE FOR FIBER ORIENTATION IN COMPOSITES

A. DETERMINATION OF THE X-RAY LINEAR ABSORPTION COEFFICIENT OF MATERIALS

A preliminary determination of the x-ray linear absorption coefficient μ of materials in our composite sytems was carried out using Equation III-25 and the density data given in Table III-1 (p. 56).

The chemical repeat units of the components are given by

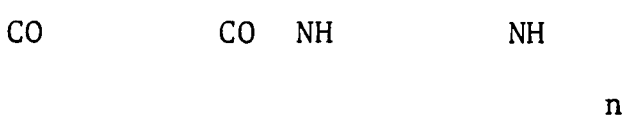

Kevlar 49

poly (p-phenylene terephthalamide)

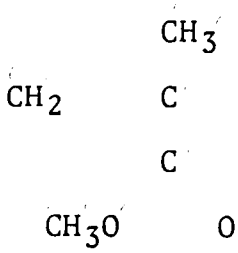

PMMA

polymethylmethacrylate

from which the x-ray linear absorption coefficients μ can be calculated as summarized in Table V-1.

Table V-1

Summary of Calculations of μ for Kevlar 49 and PMMA

Element	n	Atomic Weight, A	$(\mu/\rho)_i$	n_iA_i	m_i	$m_i(\mu/\rho)_i$
			Kelvar 49*			
C	14	12.011	4.60	168.154	0.706	3.247
H	10	1.008	0.435	10.080	0.042	0.018
O	2	16.000	11.5	32.000	0.134	1.545
N	2	14.008	7.52	28.016	0.118	0.884
				238.250	1.000	5.694
			PMMA**			
C	5	12.011	4.60	60.055	0.600	2.760
H	8	1.008	0.435	8.064	0.080	0.035
O	2	16.000	11.5	32.000	0.320	3.680
					1.000	6.475

*ρ = 1.44 gm/cm^3; μ = 8.20 cm^{-1}; (μ/ρ) = 5.694 cm^2/gm.

**ρ = 1.19 gm/cm^3; μ = 7.71 cm^{-1}; (μ/ρ) = 6.475 cm^2/gm.

Several of the intensity corrections described in Chapter III require us to know the μT of the specimen being investigated. An approximate value can be determined from the measured thickness and the results given in Table V-1 for μ; however, for accurate calculations, an experimental determination of μ was carried out by measuring the decrease in intensity of a monochromatic x-ray beam on passing perpendicularly through the specimen. The reflection from the cleavage planes (d = 2.82 Å) of a crystal of NaCl was used as the monochromatic beam. The value of μ for the reinforcing Kevlar 49 fibers, the amorphous PMMA matrix and the composite systems, respectively, was determined experimentally using samples prepared according to the procedures described in Chapter III. Results of these determinations are given in Table V-2.

The μ values for the amorphous standard and composite $(K\text{-}49\text{-}PMMA)_c$ were determined using several samples of almost identical thicknesses. Therefore, from the definition of linear absorption coefficient (98), it follows

$$\ln\frac{I_o}{I} = \mu T \qquad [V\text{-}1]$$

where I_o and I are the incident and transmitted intensities and T is the thickness of the specimen in centimeters.

Equation V-1 shows that a plot of $\ln(I_o/I)$ versus T should give a straight line with slope equal to μ. This

Table V-2

Experimental Values of μ for Materials

Material	Observations	μ cm^{-1}
Kevlar 49	Fiber Standard T = 0.090 cm	6.251
PMMA	Amorphous Standard (Several samples)	7.224
$(K\text{-}49\text{-}PMMA)_C$	Composite ϕ = 0.20 (Several samples)	7.319
$(K\text{-}49\text{-}PMMA)_S$	Composite Standard (Fiber Standard + Amorphous Standard Window) ϕ = 0.484 T = 0.186 cm	6.761

can be observed in Figures V-1 and V-2 where the excellent correlations obtained account for the careful experimental procedures followed in determining μ.

B. FIBER CHARACTERIZATION

A knowledge of the structure and degree of orientation of the Kevlar 49 fibers used as crystalline reinforcement in our systems was a necessary requirement before any other study could be carried out.

Northolt (84) has reported an x-ray study of poly (p-phenylene terephthalamide) fibers. He found that all the reflections observed in x-ray diffraction photographs of well-oriented fibers could be satisfactorily indexed by assuming a monoclinic (pseudo-orthorhombic) unit cell with dimensions a = 7.87 Å, b = 5.18 Å and c (fiber axis) = 12.9 Å, γ being approximately 90°. Northolt classified 44 reflections as being above background and was able to determine their intensities visually. These reflections are listed in Table V-3, along with their respective indices and values of $\sin^2\theta_{hkl}$ calculated by means of the following equation (49) for an orthorhombic system:

$$\sin^2\theta_{hkl} = \frac{\lambda^2}{4a^2} h^2 + \frac{\lambda^2}{4b^2} k^2 + \frac{\lambda^2}{4c^2} l^2 \qquad [V-2]$$

which can be written as

$$\sin^2\theta_{hkl} = Ah^2 + Bk^2 + Cl^2 \qquad [V-3]$$

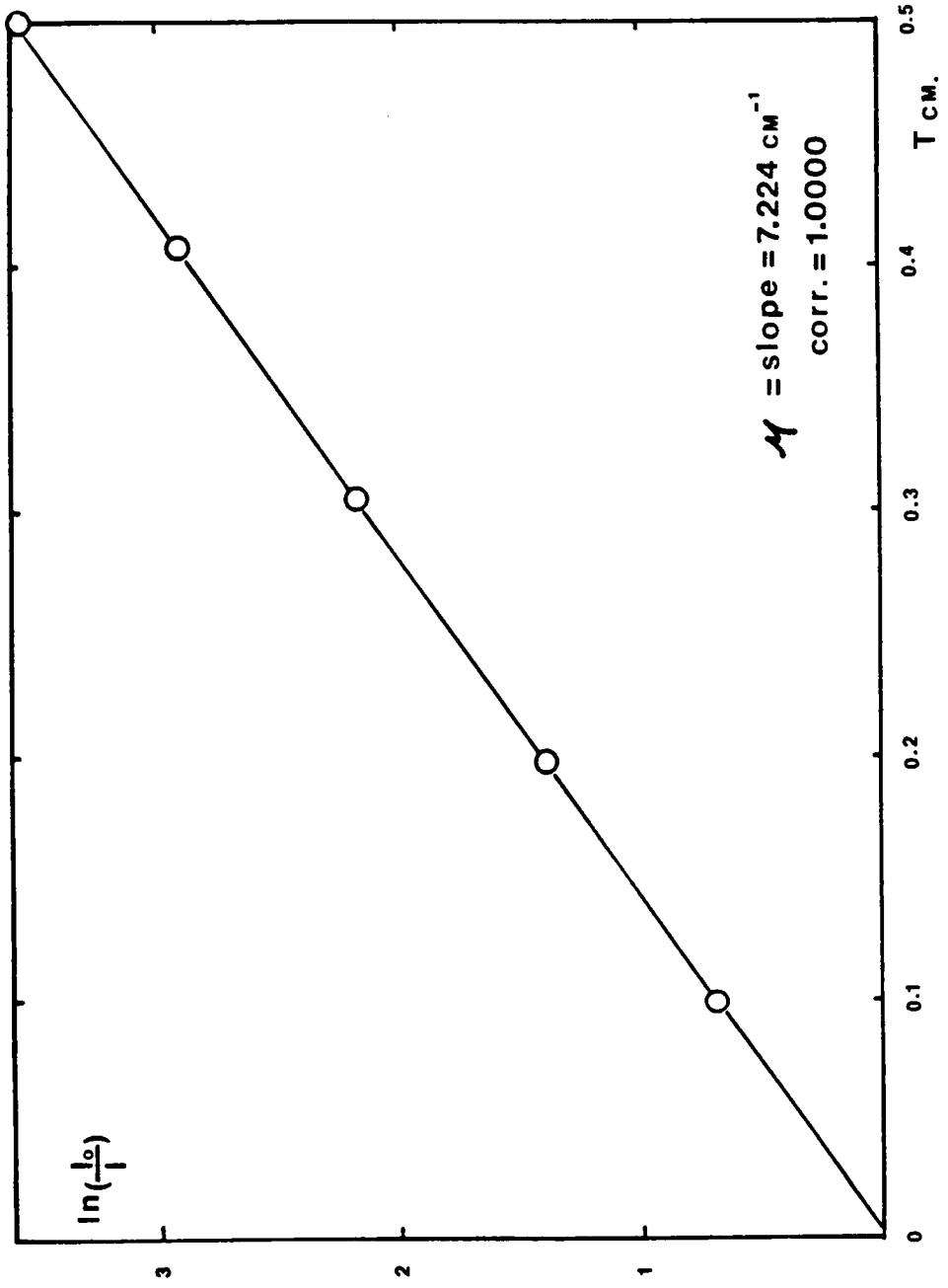

Figure V-1. PMMA x-ray linear absorption coefficient (μ) PMMA.

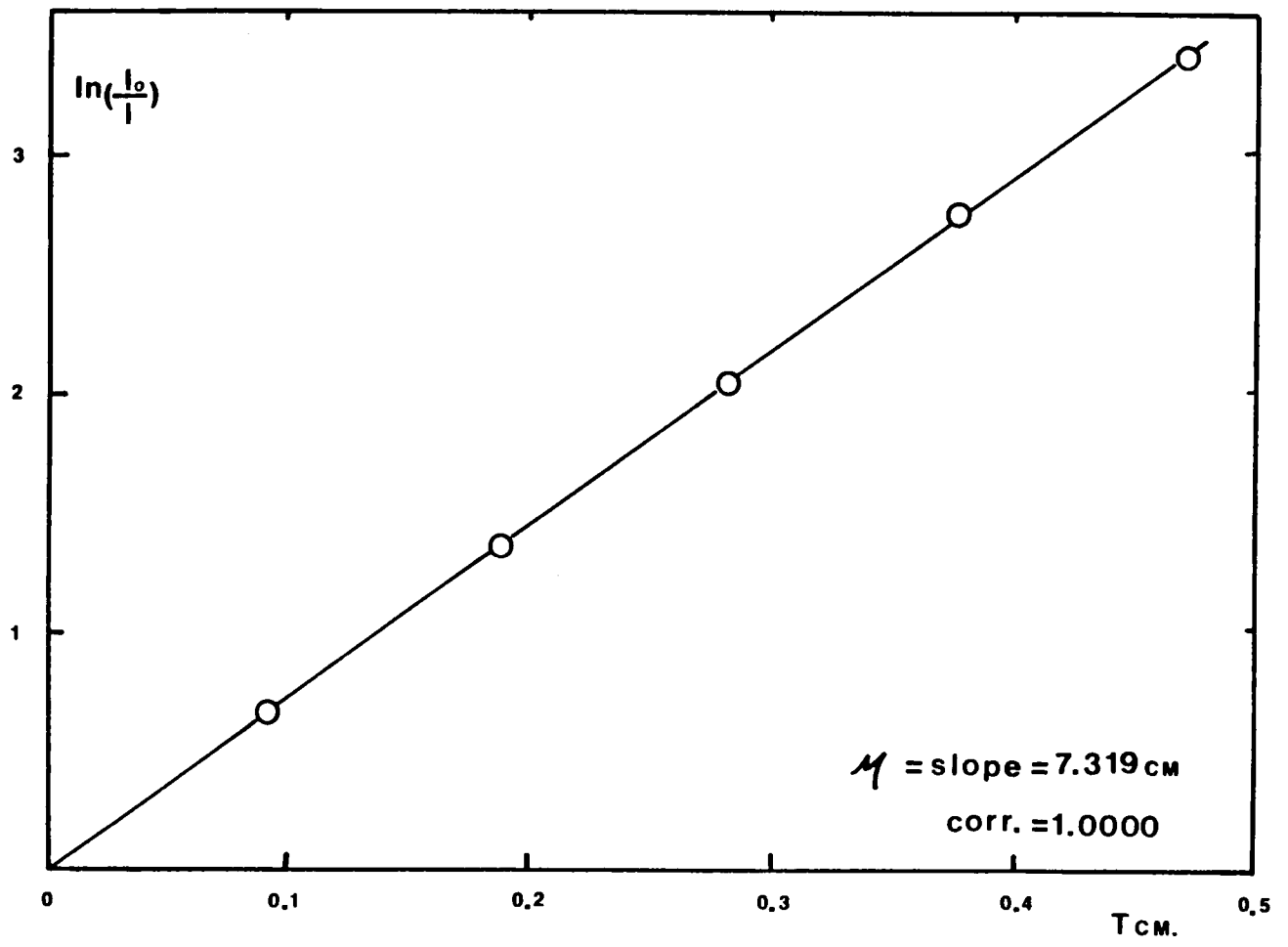

Figure V-2. PMMA-K49-ϕ = 0.20, x-ray linear absorption coefficient $(\mu)_{comp}$.

Table V-3

List of Observed Reflections for Poly (p-Phenylene Terephthalamide) Fibers [after Northolt (117)]

hkl*	I^{**}_{obs}	$\sin^2\theta_{hkl}$	hkl*	I_{obs}	$\sin^2\theta_{hkl}$
002	m	0.0144	020	vw	0.0884
004	s	0.0576	021	w	0.0920
005	vw	0.0900	022	m	0.1028
006	s	0.1296	023	w	0.1208
104	w	0.0672	024	w	0.1460
106	s	0.1392	025	vw	0.1784
011	vw	0.0257	121	w	0.1016
012	vw	0.0365	310	m	0.1085
013	w	0.0545	311	vw	0.1121
014	w	0.0797	220	w	0.1268
015	w	0.1121	221	w	0.1304
016	w	0.1517	222	w	0.1412
110	vs	0.0317	223	vw	0.1592
111	s	0.0353	224	vw	0.1844
112	w	0.0461	400	w	0.1536
113	w-m	0.0641	402	w	0.1680
114	w	0.0893	321	w-m	0.1784
116	vw	0.1613	132	w	0.2229
200	vs	0.0384	420	w-m	0.2420
202	w	0.0528	510	vw	0.2621
211	s	0.0641	330	vw	0.2853
213	w	0.0929	620	w	0.4340

*I(hkl) and I($\bar{h}$kl) are taken together.

**Visually estimated intensities: vs = very strong; s = strong; m = medium; w = weak; vw = very weak.

where A = 0.0096, B = 0.0221 and C = 0.0036 for an orthorhombic unit cell having the dimensions given by Northolt (84) and using CuK_α radiation λ = 1.5418 Å.

A flat-film fiber pattern, Figure V-3, was prepared using the Kevlar 49 fiber standard and the procedure described in Chapter III with a sample-film distance of 2.660 cm. Measurements were carried out on this pattern to calculate values of $\sin^2\theta_{hkl}$ for each of the reflections observed. The experimental results are summarized in Table V-4, along with the values expected from Equation V-2 for the indices assigned. A good agreement is observed between experimental and expected values.

As a next step in the characterization procedure, 2θ x-ray diffractometer scans were carried out with the fiber standard in the range 2θ = 10-50°. These 2θ scans were taken at fixed values of the azimuthal angle φ (or x), which was increased 10 degrees at a time from 0° to 90° in order to explore the whole sphere of reflection. Figure V-4 shows the 2θ x-ray diffractometer scan for φ = 90°, where the main equatorial reflections (110) and (200) are well resolved. A careful analysis of these 2θ - φ x-ray scans allowed us to select the most suitable values of 2θ to determine background corrections and also the values of the aximuth φ that have to be aovided in order to eliminate interferences from reflections other than (110) and (200). These two equatorial reflections have been used to determine

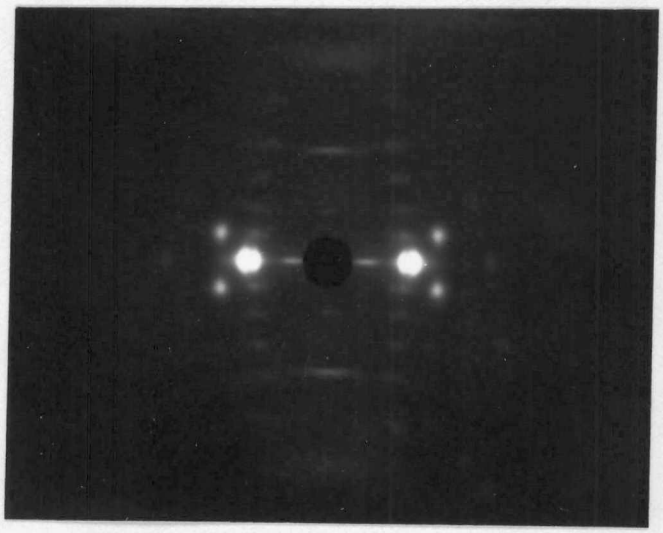

Figure V-3. Kevlar 49, x-ray flat-film fiber pattern.

Table V-4

Indexed Reflections for Kevlar 49
X-Ray Fiber Pattern

hkl	$Sin^2\theta_{hkl}$ (expected)	$Sin^2\theta_{hkl}$ (experimental)	hkl	$Sin^2\theta_{hkl}$ (expected)	$Sin^2\theta_{hkl}$ (experimental)
002	0.0144	0.0140	015	0.1121	0.1131
004	0.0576	0.0567	110	0.0317	0.0311
006	0.1296	0.1322	111	0.0353	0.0349
011	0.0257	0.0249	200	0.0384	0.0392
012	0.0365	0.0396	211	0.0641	0.0634
013	0.0545	0.0552	022	0.1028	0.1021
014	0.0797	0.0775	310	0.1085	0.1083

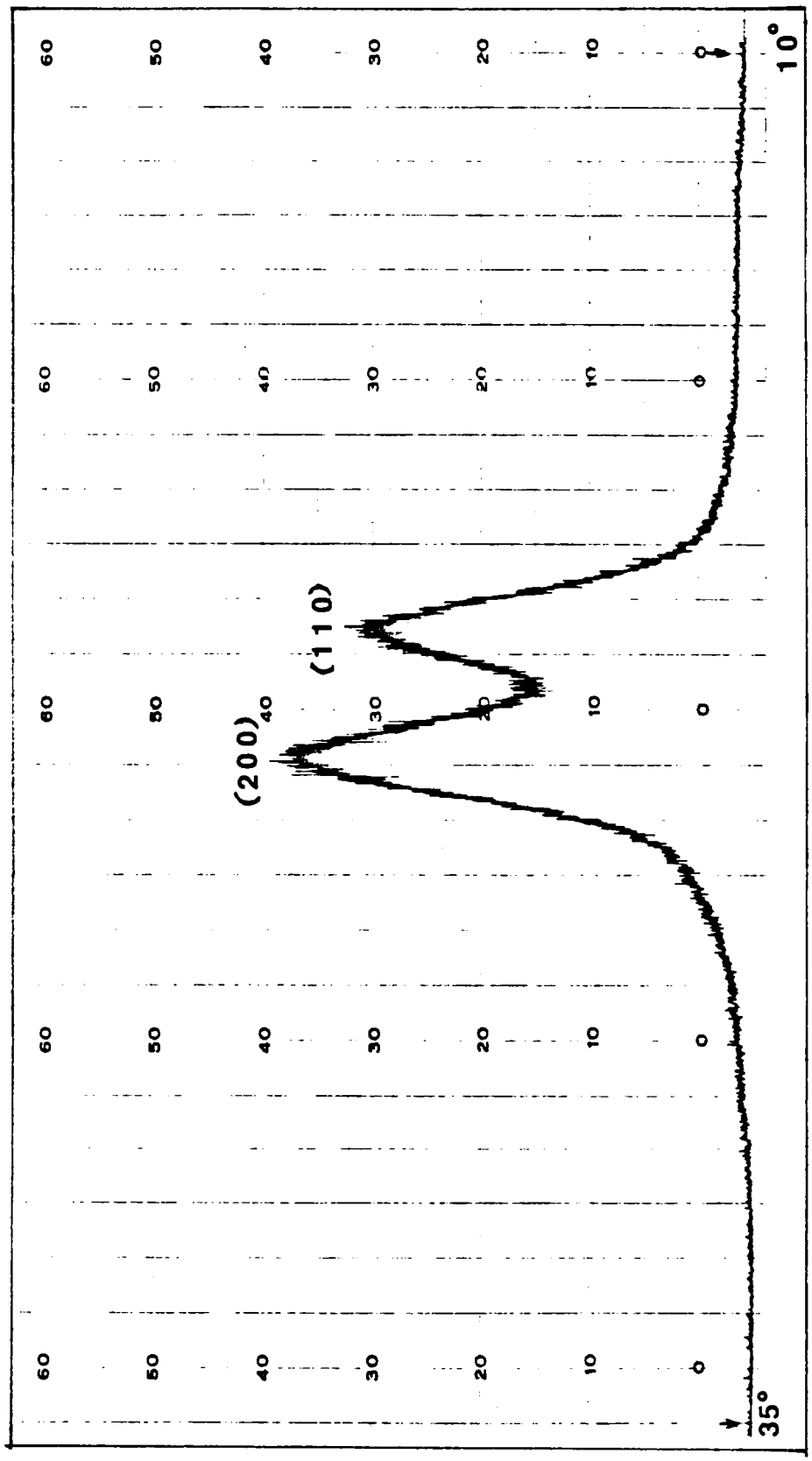

Figure V-4. Kevlar 49 main equatorial reflections (2θ diffractometer scan).

the Herman-Stein uniaxial orientation factor, f_c, following the procedure given by Stein (101). Table V-5 summarizes the selected values of 2θ and ϕ or χ, and the interferences expected at the omitted angles. A linear background is assumed at constant ϕ or χ. Then, all data is plotted as a function of ϕ or χ, for each value of 2θ, and the necessary data points are generated using Newton's Divided Difference Formula (119).

Air scattering curves for the two diffractometers used are given in Figures V-5 through V-7. Figure V-6 is interesting because it shows the anomalous air scattering curve obtained for the Single Crystal Orienter due to improper shielding of the receiving slit assembly. This effect was corrected by a proper shield with leaded paper as it is shown in Figure V-7.

Intensity data were recorded in both apparatus for the fiber standard at the selected angular values reported in Table V-5, and corrected by use of Equation III-18. Figures V-8 and V-9 show the corrected fiber background intensities for each equipment at the selected angular values. Figures V-10 and V-11 give the final corrected fiber background curves generated from the selected values by means of Newton's interpolation formula.

Figures V-12 through V-15 give the final corrected fiber intensities (after correcting for fiber background) as a function of the azimuth ϕ or χ for each of the two

Table V-5

Selected Values of 2θ and ϕ for Intensity Measurements in Kevlar 49*

ϕ	2θ=10°	12°	20.55°	22.85°	32°	34°
0°	✓	x	✓	✓	x	x
5°			✓	✓		
10°	✓	✓	✓	✓	✓	x
15°			✓	✓		✓
20°	✓	✓	✓	✓	x	✓
25°			✓	✓		
30°	✓	✓	✓	✓	x	x
35°			✓	✓		
40°	✓	✓	✓	✓	x	x
45°			✓	✓		
50°	✓	✓	✓	x	x	x
55°			✓	x		
60°	✓	✓	✓	✓	✓	✓
65°			✓	✓		
70°	✓	✓	x	x	✓	✓
75°			✓	✓		
80°	✓	✓	✓	✓	x	x
85°			✓	✓		
90°	✓	✓	✓	✓	✓	x
	Background		(110)	(200)	Background	

Table V-5 (continued)

*Interferences:

(002) $2\theta = 13.7°$, $\phi = 0°$

(004) $2\theta = 27.8°$, $\phi = 0°$

(005) $2\theta = 34.8°$, $\phi = 0°$

(014) $2\theta = 32.7°$, $\phi = 31.9°$

(114) $2\theta = 34.7°$, $\phi = 36.7°$

(113) $2\theta = 29.3°$, $\phi = 44.8°$

(012) $2\theta = 22.0°$, $\phi = 51.2°$

(213) $2\theta = 35.5°$, $\phi = 53.9°$

(112) $2\theta = 24.8°$, $\phi = 56.1°$

(111) $2\theta = 21.7°$, $\phi = 71.5°$

(211) $2\theta = 29.4°$, $\phi = 76.3°$

(021) $2\theta = 35.4°$, $\phi = 78.6°$

(020) $2\theta = 34.6°$, $\phi = 90°$

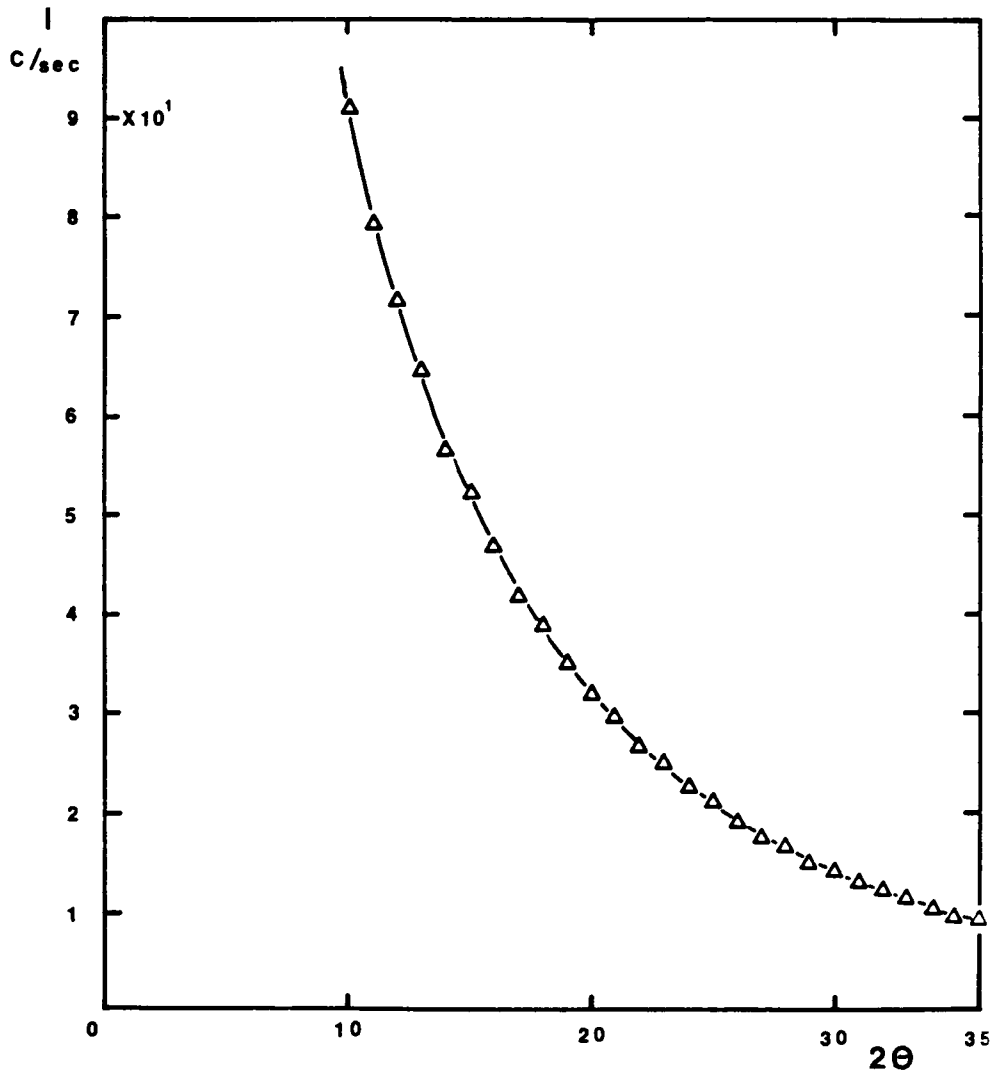

Figure V-5. Norelco diffractometer air scattering curve.

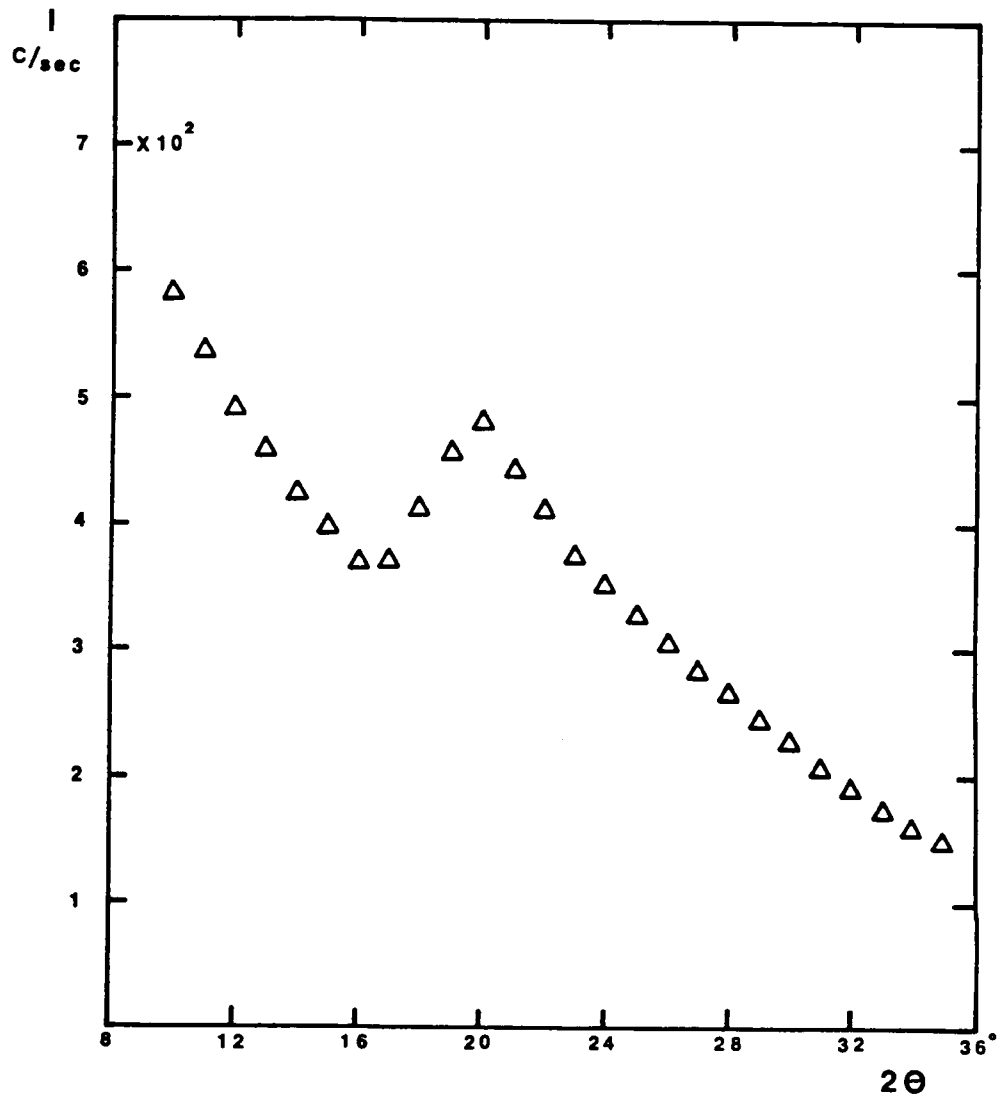

Figure V-6. Single crystal orienter air scattering curve (anomalous).

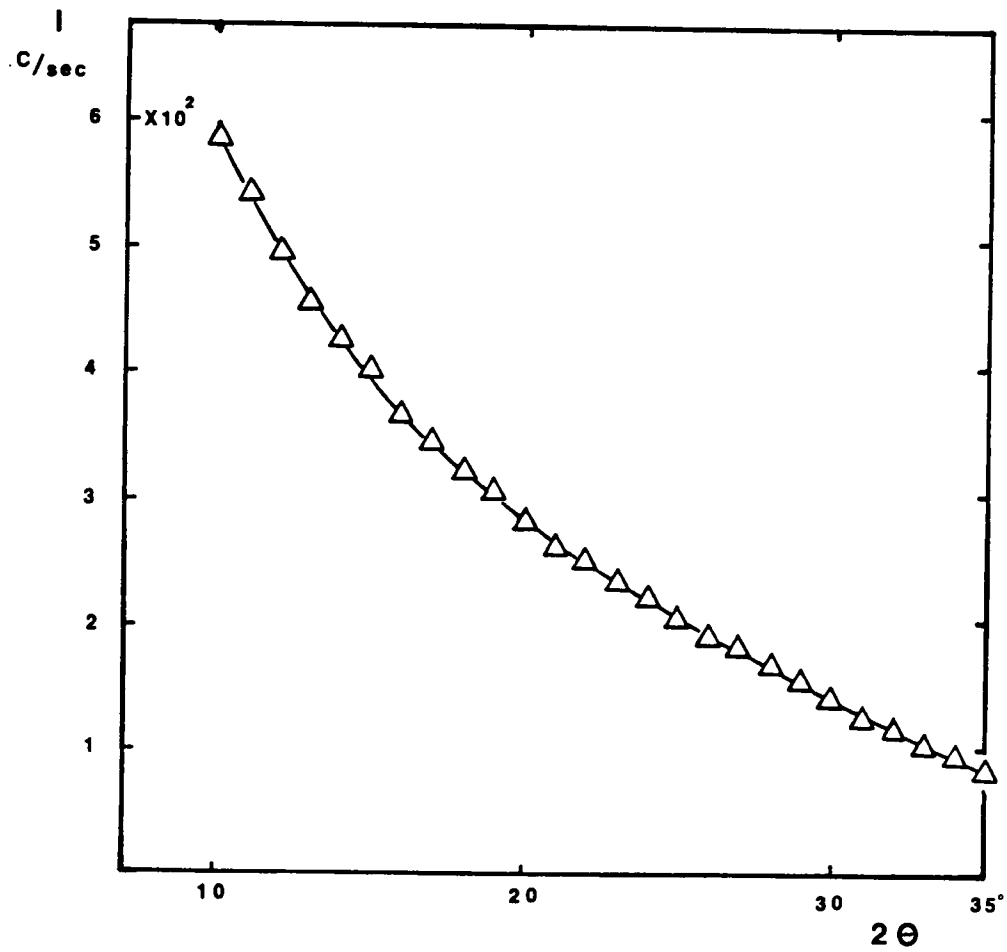

Figure V-7. Single crystal orienter air scattering curve (corrected).

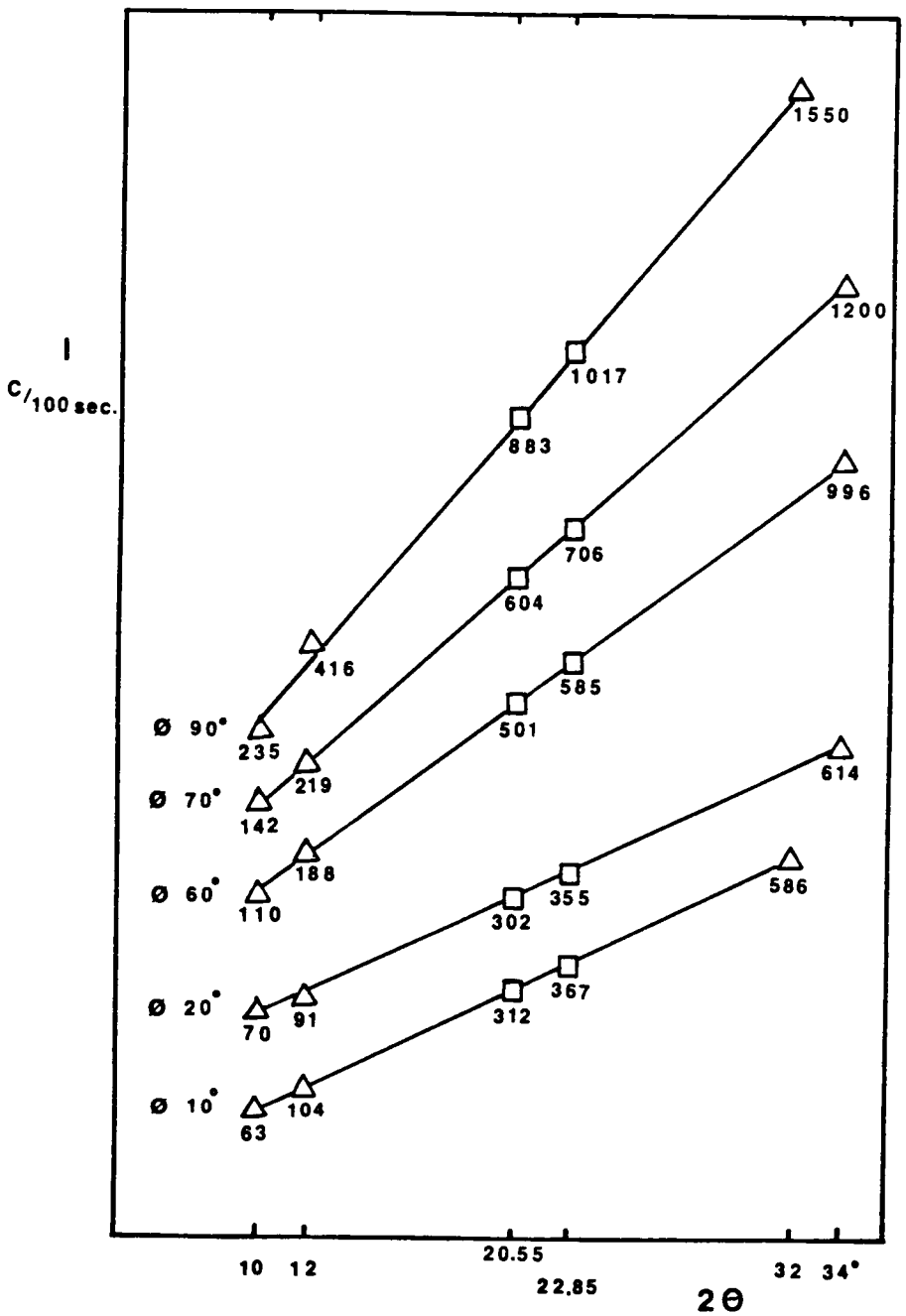

Figure V-8. Kevlar 49 corrected background intensities at selected angular values (Norelco diffractometer).

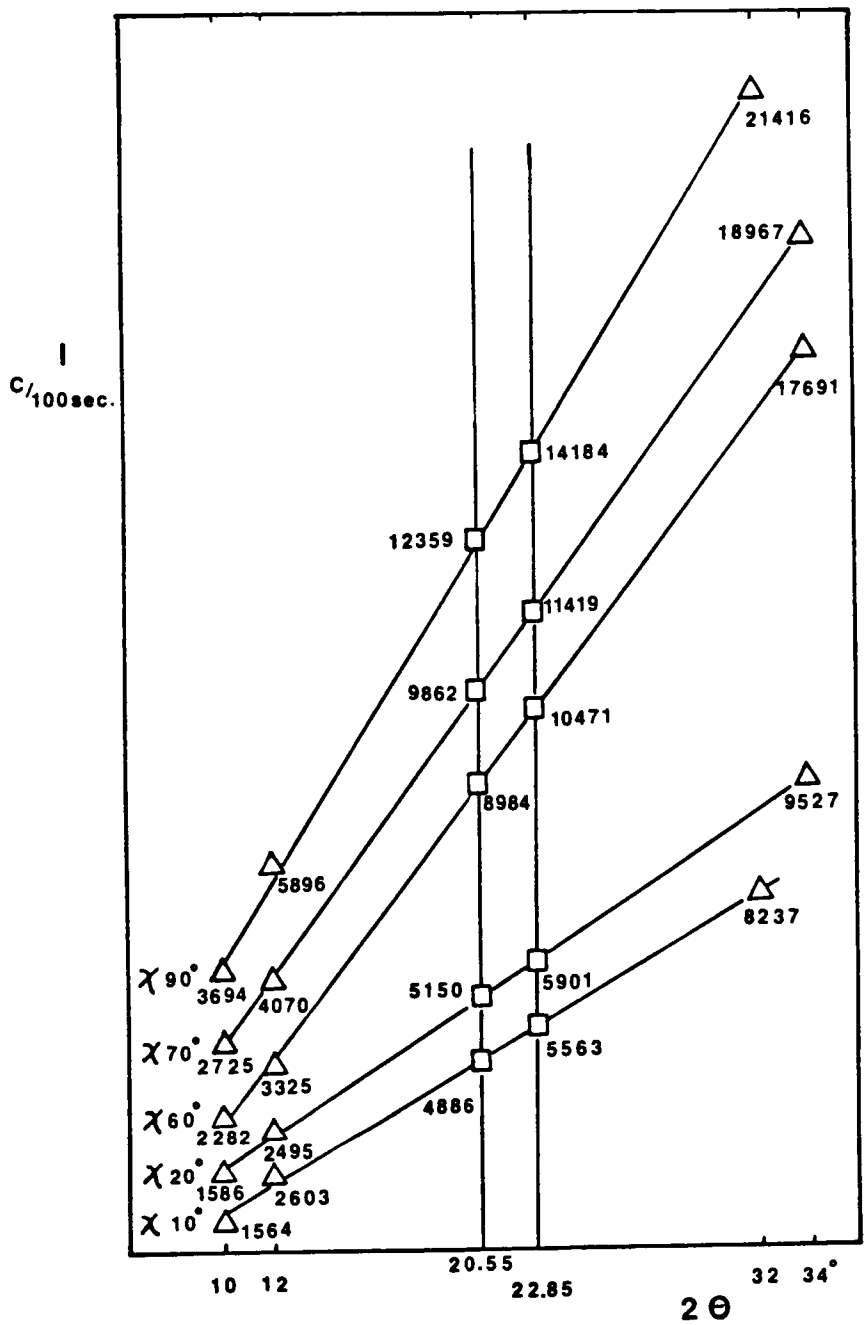

Figure V-9. Kevlar 49 corrected background intensities at selected angular values (Single Crystal Orienter).

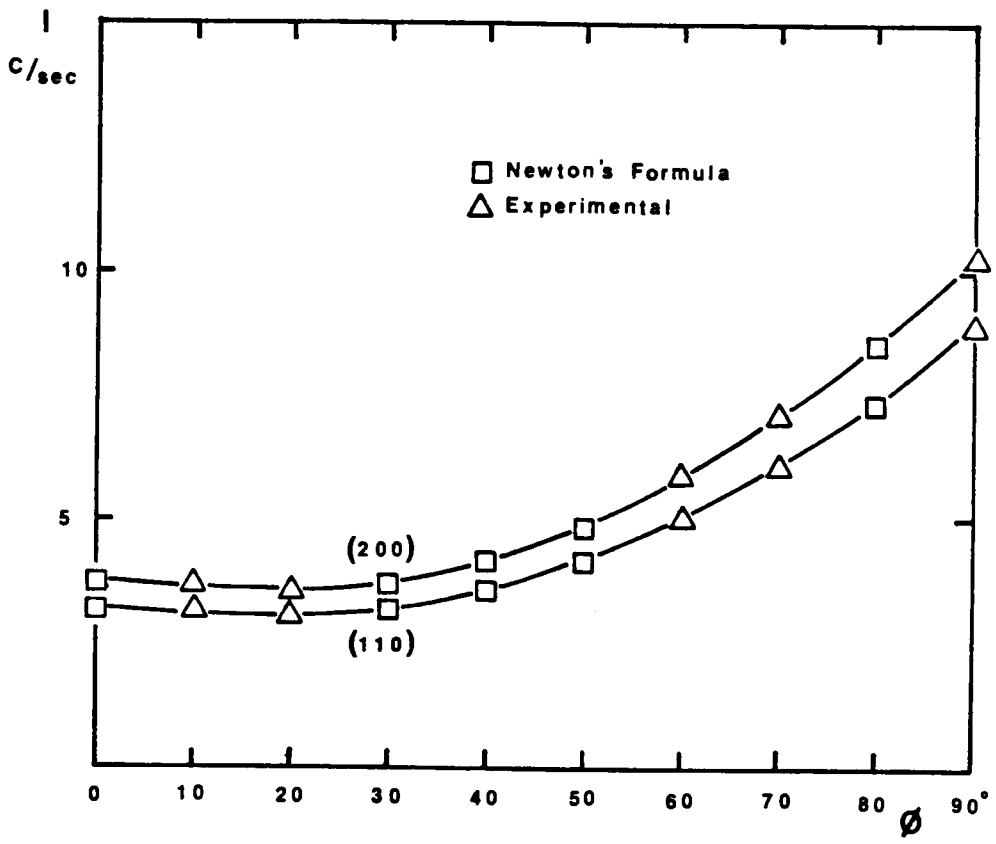

Figure V-10. Kevlar 49 corrected background intensity curves (Norelco diffractometer).

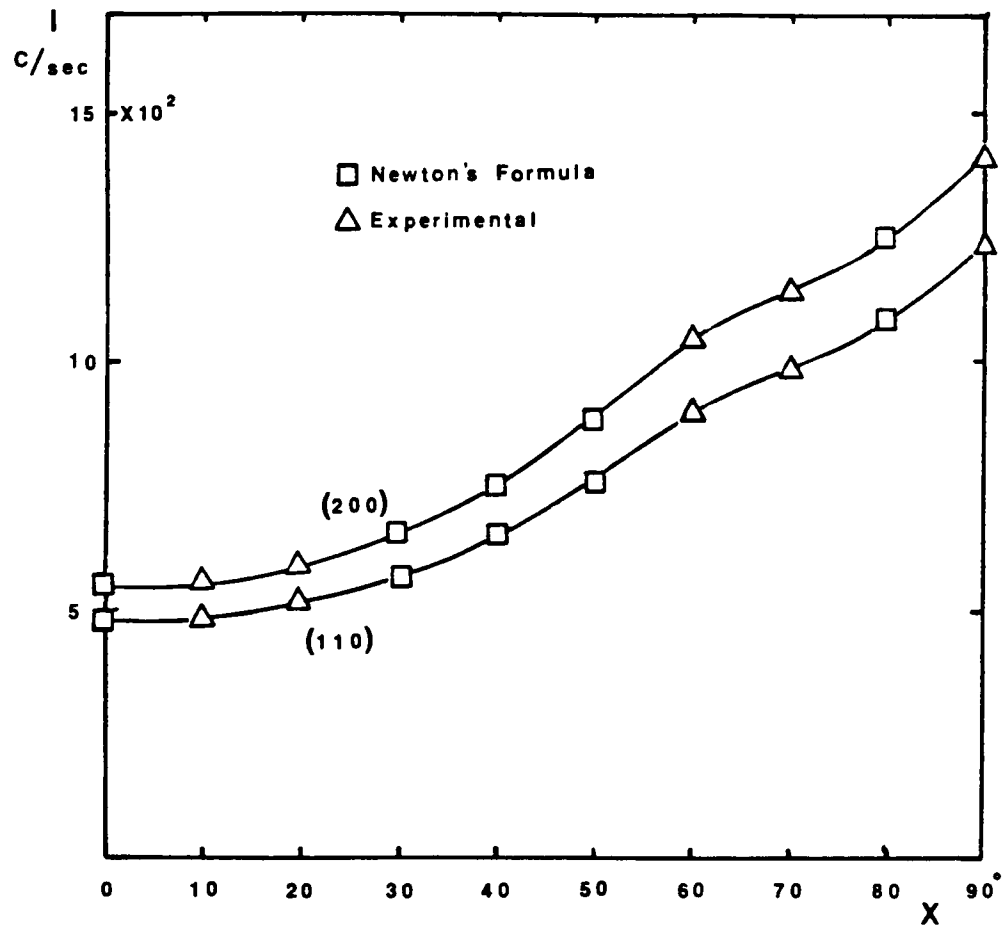

Figure V-11. Kevlar 49 corrected background intensity curves (Single Crystal Orienter).

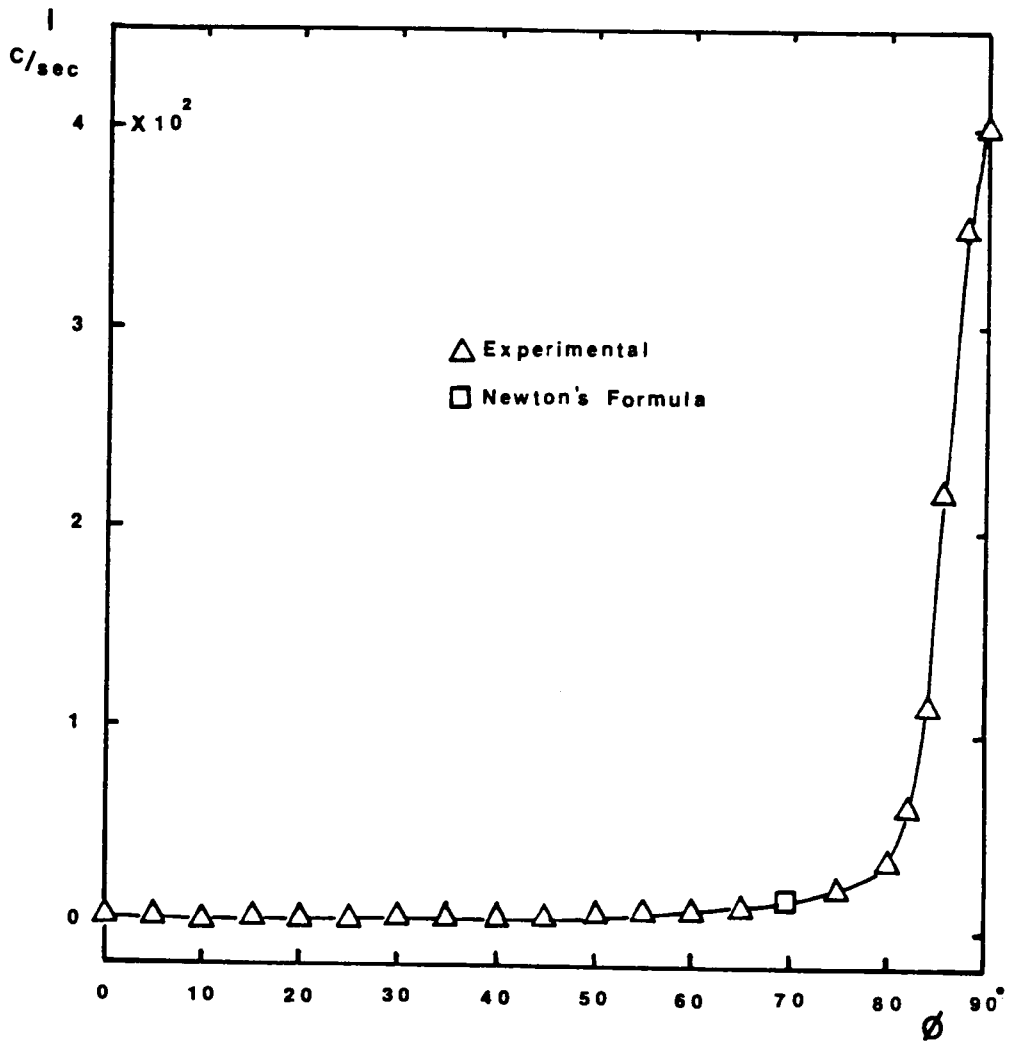

Figure V-12. Kevlar 49 fully corrected intensity curve for the (110) plane poles as a function of the azimuthal angle ϕ in the Norelco diffractometer.

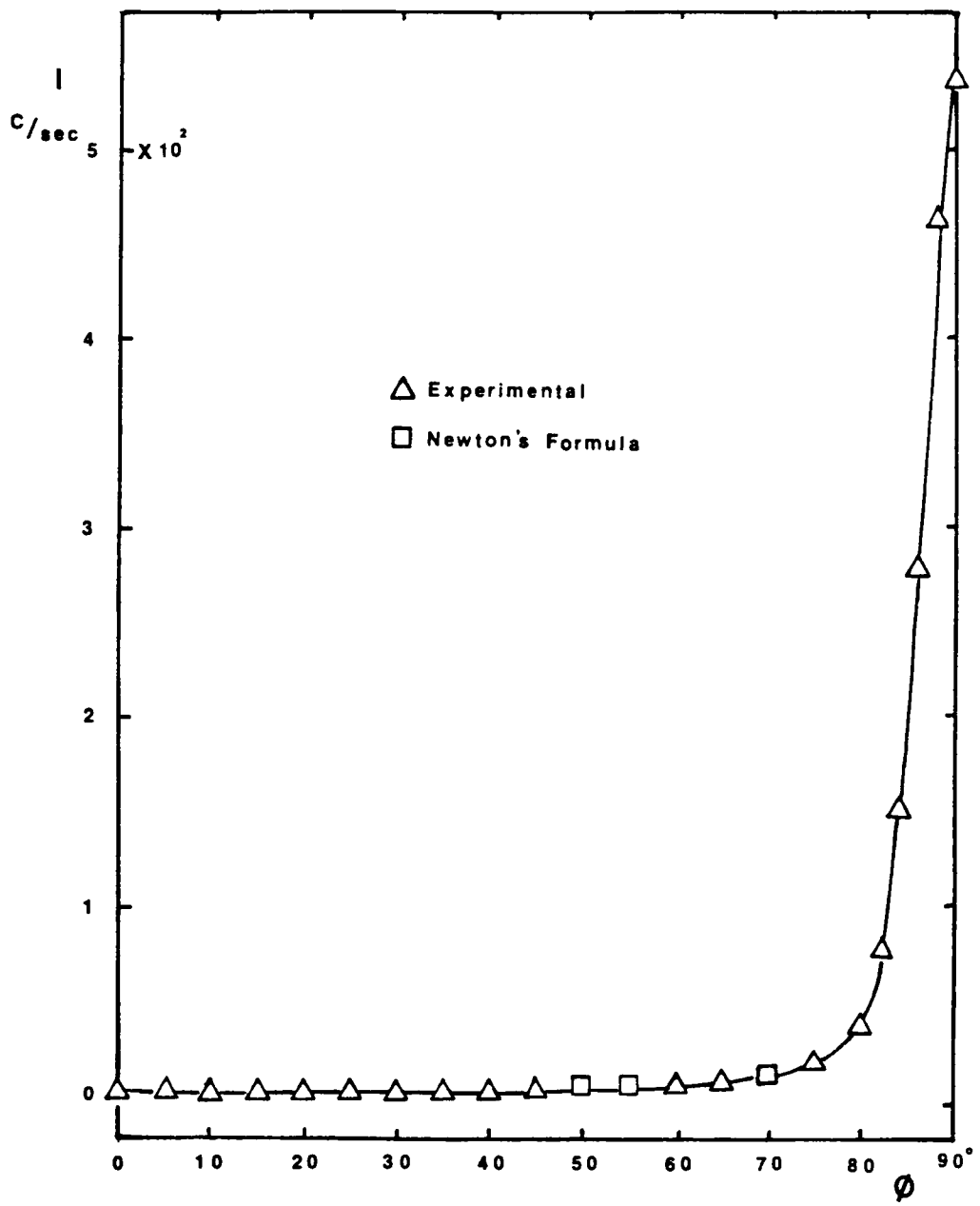

Figure V-13. Kevlar 49 fully corrected intensity curve for the (200) plane poles as a function of the azimuthal angle ϕ in the Norelco diffractometer.

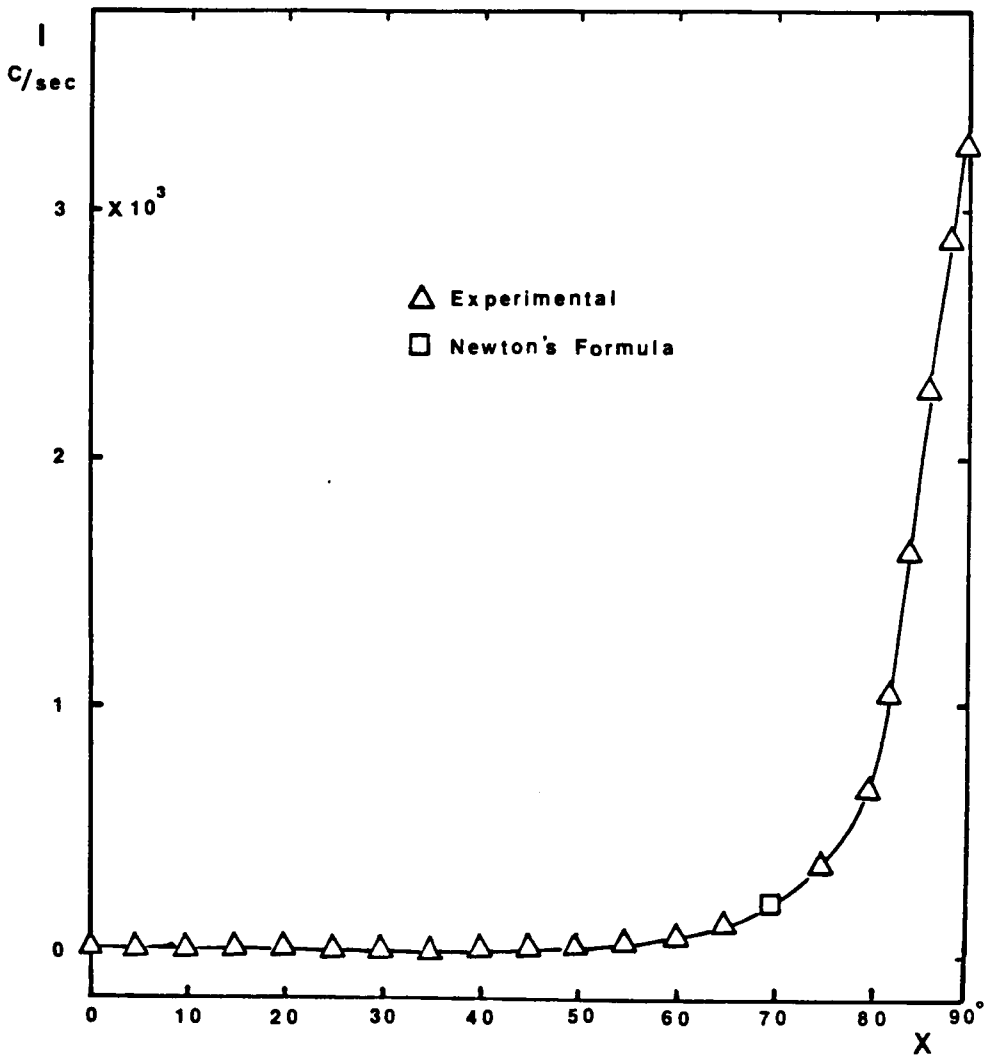

Figure V-14. Kevlar 49 fully corrected intensity curve for the (110) plane poles as a function of the azimuthal angle χ in the Single Crystal Orienter.

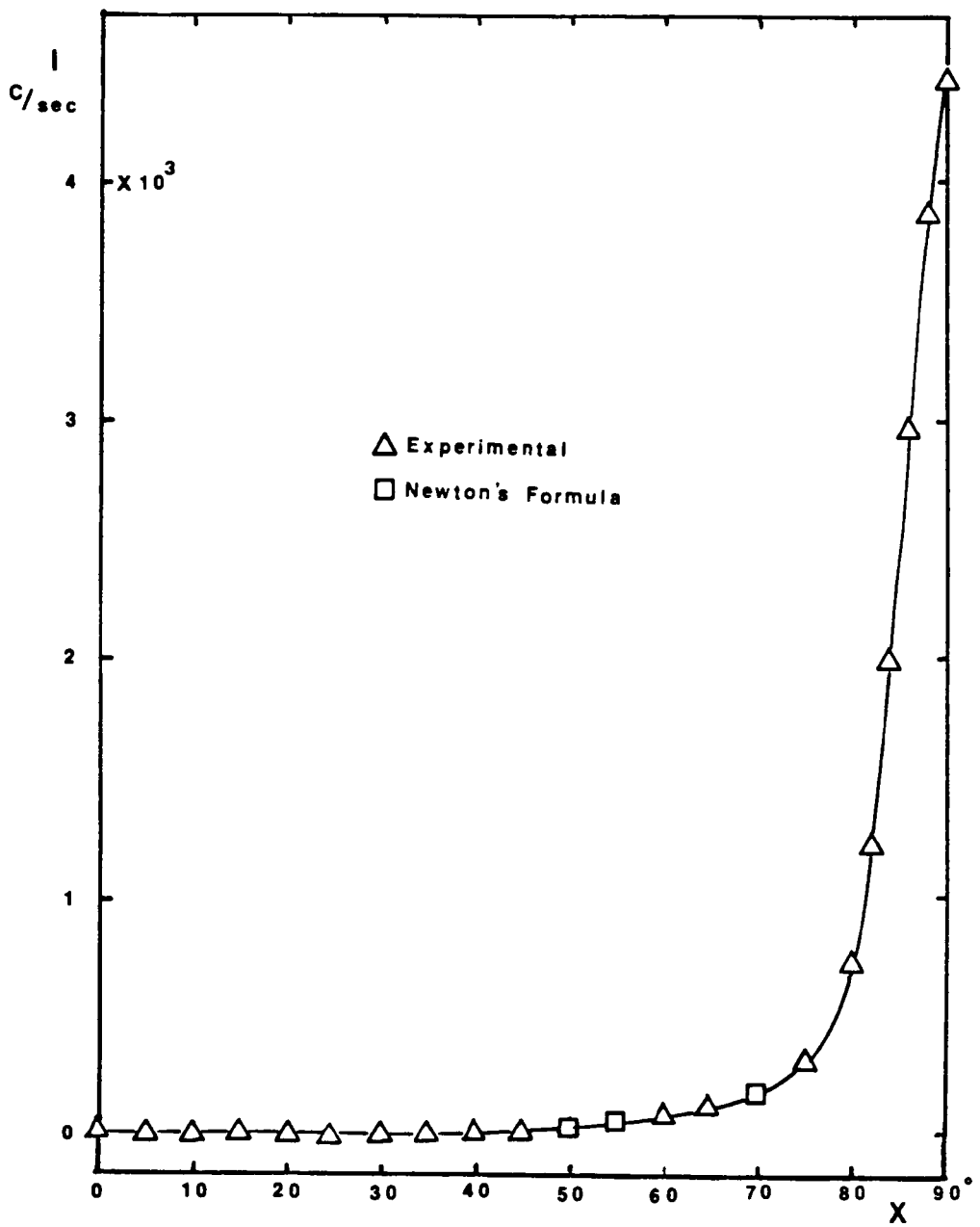

Figure V-15. Kevlar 49 fully corrected intensity curve for the (200) plane poles as a function of the azimuthal angle χ in the Single Crystal Orienter.

main equatorial reflections recorded in each piece of apparatus. From these plots, intensity values were read off at 2° intervals to obtain a reasonable approximation to the integrals of Equation II-37 as follows:

$$\overline{\cos^2\phi_{hkl}} = \frac{\sum_{0^\circ}^{90^\circ} I(\phi) \sin\phi \cos^2\phi}{\sum_{0^\circ}^{90^\circ} I(\phi) \sin\phi} \qquad [V\text{-}4]$$

Also, for an orthorhombic unit cell and hk0 planes, we can write (118)

$$\overline{\cos^2\phi_{hk0}} = e^2 \overline{\cos^2\phi_{v,z}} + f^2 \overline{\cos^2\phi_{v,z}} \qquad [V\text{-}5]$$

and

$$\overline{\cos^2\phi_{u,z}} + \overline{\cos^2\phi_{v,z}} + \overline{\cos^2\phi_{c,z}} = 1 \qquad [V\text{-}6]$$

where e and f are the direction cosines of a unit vector $\overline{N}$ in the direction of N (the normal to the set of planes being considered), and u and v are cartesian coordinate axes which, in this particular case of orthorhombic symmetry, coincide with the crystallographic axes a and b, respectively.

From the geometry of the unit cell for Kevlar 49, it is easily found that the direction cosines for the two equatorial reflections are given by

(110) $e = 0.5498$ $f = 0.8353$

(200) $e = 1.0000$ $f = 0.0000$

and using Equations V-4 and V-5

$$\overline{\cos^2\phi_{110,z}} = 0.3023\ \overline{\cos^2\phi_{u,z}} + 0.6977\ \overline{\cos^2\phi_{v,z}} \quad [V\text{-}7a]$$

$$\overline{\cos^2\phi_{200,z}} = \overline{\cos^2\phi_{v,z}} \quad [V\text{-}7b]$$

$$\overline{\cos^2\phi_{c,z}} = 1 - \overline{\cos^2\phi_{u,z}} - \overline{\cos^2\phi_{v,z}} \quad [V\text{-}7c]$$

Solving Equations V-6a, b, c simultaneously for $\overline{\cos^2\phi_{c,z}}$ gives

$$\overline{\cos^2\phi_{c,z}} = 1 - \overline{\cos^2\phi_{200,z}} - \left[\frac{\overline{\cos^2\phi_{110,z}} - 0.3023\ \overline{\cos^2\phi_{200,z}}}{0.6977}\right] \quad [V\text{-}8]$$

Using the intensity data from Figures V-11 through V-14 (pp. 122-125) and Equations V-4, V-7a, b, c, and II-15, the results obtained are shown in Table V-6.

C. COMPOSITE STANDARD CHARACTERIZATION

A composite standard was prepared in order to determine the experimental feasibility (calibration) of the procedure developed in Chapter III (Section C) to resolve the PMMA amorphous contribution to the background. This composite standard consisted of the Kevlar 49 fiber standard and PMMA amorphous standard sheet. Figure V-16 shows the corrected diffractometer intensities for the amorphous standard as a

Table V-6

Cosine Squared Values and Orientation Functions for Kevlar 49 Fiber Standard

Norelco Diffractometer	Single Crystal Orienter
$\overline{\cos^2\phi_{111,z}} = 0.0178$	$\overline{\cos^2\phi_{110,z}} = 0.0273$
$\overline{\cos^2\phi_{200,z}} = 0.0143$	$\overline{\cos^2\phi_{200,z}} = 0.0232$
$\overline{\cos^2\phi_{c,z}} = 0.9664$	$\overline{\cos^2\phi_{c,z}} = 0.9477$
$f_c = 0.950$	$f_c = 0.922$

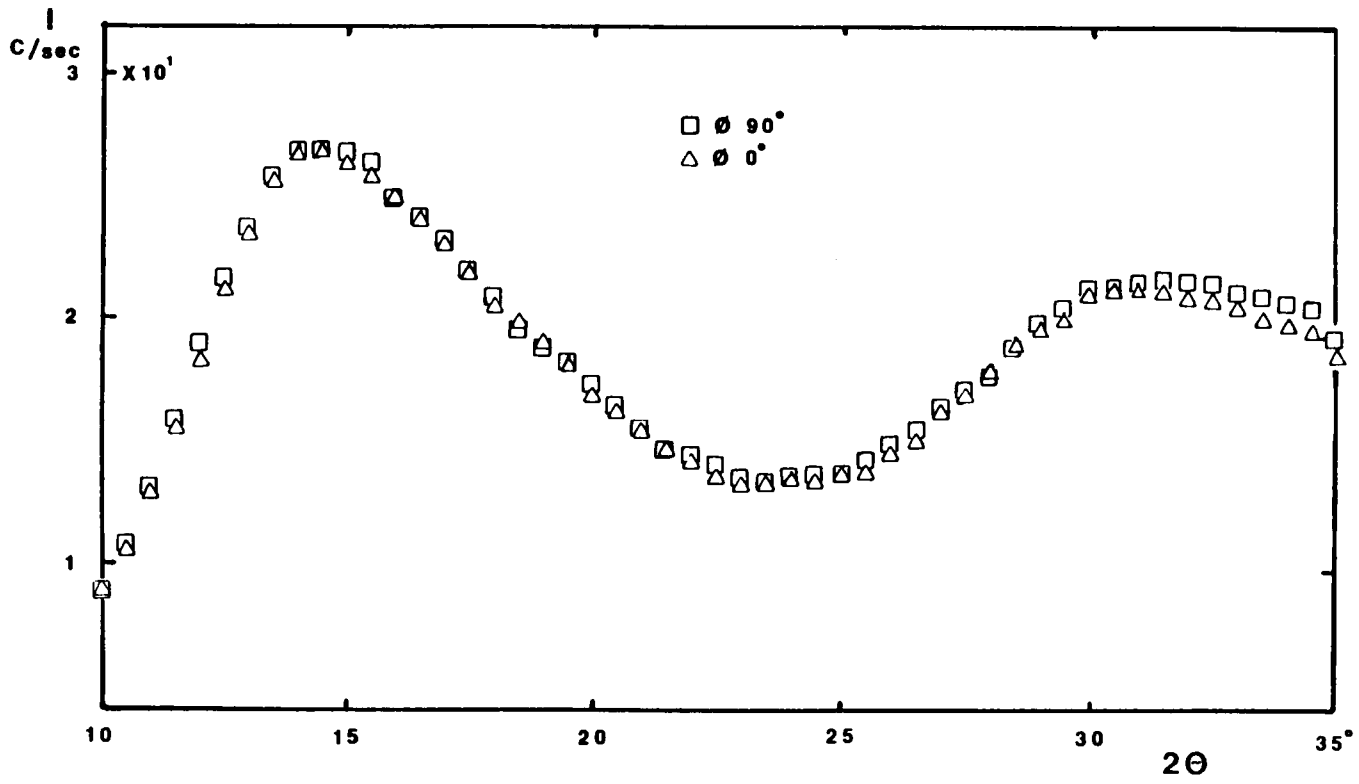

Figure V-16. PMMA amorphous standard corrected intensities. (2θ diffractometer scans at $\phi = 0°$ and $\phi = 90°$.)

function of 2θ at the two extremes of the aximuthal range ($\phi = 0°$ and $\phi = 90°$). Superposition of intensity data for the two azimuthal settings is evident from data on Figure V-16, and the true amorphous nature of our standard is confirmed.

Intensity measurements were then carried out for the composite and PMMA standards under exactly the same conditions and angles as those used for the Kevlar 49 fiber standard in the previous section. Both x-ray apparatus were used in these measurements. Table V-7 shows the characteristics of the composite standard and summarizes the steps followed to determine the PMMA amorphous contribution in both apparatus.

In order to compare the absolute magnitude of the calculated corrected fiber intensity $(I_c\phi)_F$ from Table V-7, with the respective experimental values of the fiber standard as reported in Figures V-11 through V-14 (pp. 122-125), the

$$(I_c\phi)_F/\exp(-\mu T)_F$$

values obtained by the procedure of Table V-7, at each value of 2θ and ϕ, are multiplied by $\exp(-\mu T)_F$ and corrected for fiber background as the fiber standard. The resulting calculated fully corrected fiber intensities are then plotted in the same graph with the experimental values from the fiber standard. Figures V-17 through V-20

Table V-7

Composite Standard: Characteristics and Analysis

Norelco Diffractometer*	Single Crystal Orienter*
T_{PMMA} analyzed = 0.100 cm	T_{PMMA} analyzed = 0.096 cm
$(\mu T)_{comp}$ = 1.2576	$(\mu T)_{comp}$ = 1.2576
$(\mu T)_{Fiber}$ = 0.5626	$(\mu T)_{Fiber}$ = 0.5626
$(\mu T)_{PMMA}$ = 0.7224	$(\mu T)_{PMMA}$ = 0.6935
Procedure	Procedure
1) Determine $(I_c\phi)_{comp}$ for each 2θ setting.	1) Determine $(I_c\phi)_{comp}$ for each 2θ setting.
2) Determine $(I_c\phi)_{PMMA}$ for each 2θ setting.	2) Determine $(I_c\phi)_{PMMA}$ for each 2θ setting.
3) Normalize $(I_c\phi)$ values dividing by the respective $[\exp(-\mu T)]$ term.	3) Normalize $(I_c\phi)$ values dividing by the respective $[\exp(-\mu T)]$ term.
4) Calculate $(I_c\phi)_F/\exp(-\mu T)_F$ using Equation III-28 point by point, as follows:	4) Calculate $(I_c\phi)_F/\exp(-\mu T)_F$ using Equation III-28 point by point, as follows:
$[(I_c\phi)_F/\exp(-0.5626)]$ =	$[(I_c\phi)_F/\exp(-0.5626)]$ =
$\left[\frac{(I_c\phi)_{comp}}{\exp(-1.2576)} - \frac{(I_c\phi)_{PMMA}}{\exp(-0.7224)}\right] \times \frac{0.096}{0.100}$	$\left[\frac{(I_c\phi)_{comp}}{\exp(-1.2576)} - \frac{(I_c\phi)_{PMMA}}{\exp(-0.6935)}\right]$

*Composite Thickness, T_{comp} = 0.186 cm
Fiber Thickness, T_F = 0.096 cm
PMMA Sheet Thickness, T_{PMMA} = 0.096 cm

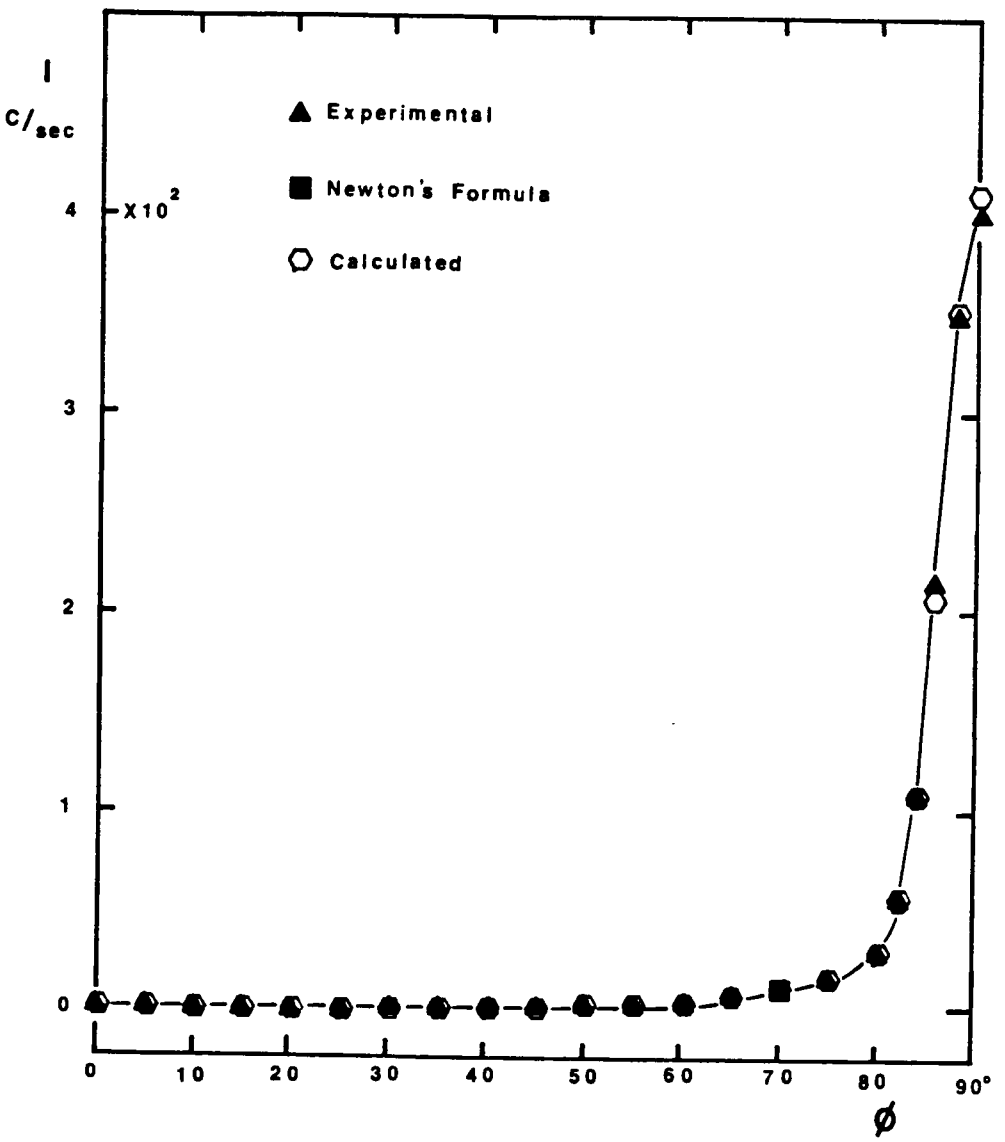

Figure V-17. Kevlar 49 fully corrected intensity curves for the (110) plane poles as a function of the azimuthal angle ϕ (experimental and calculated values from the Norelco diffractometer).

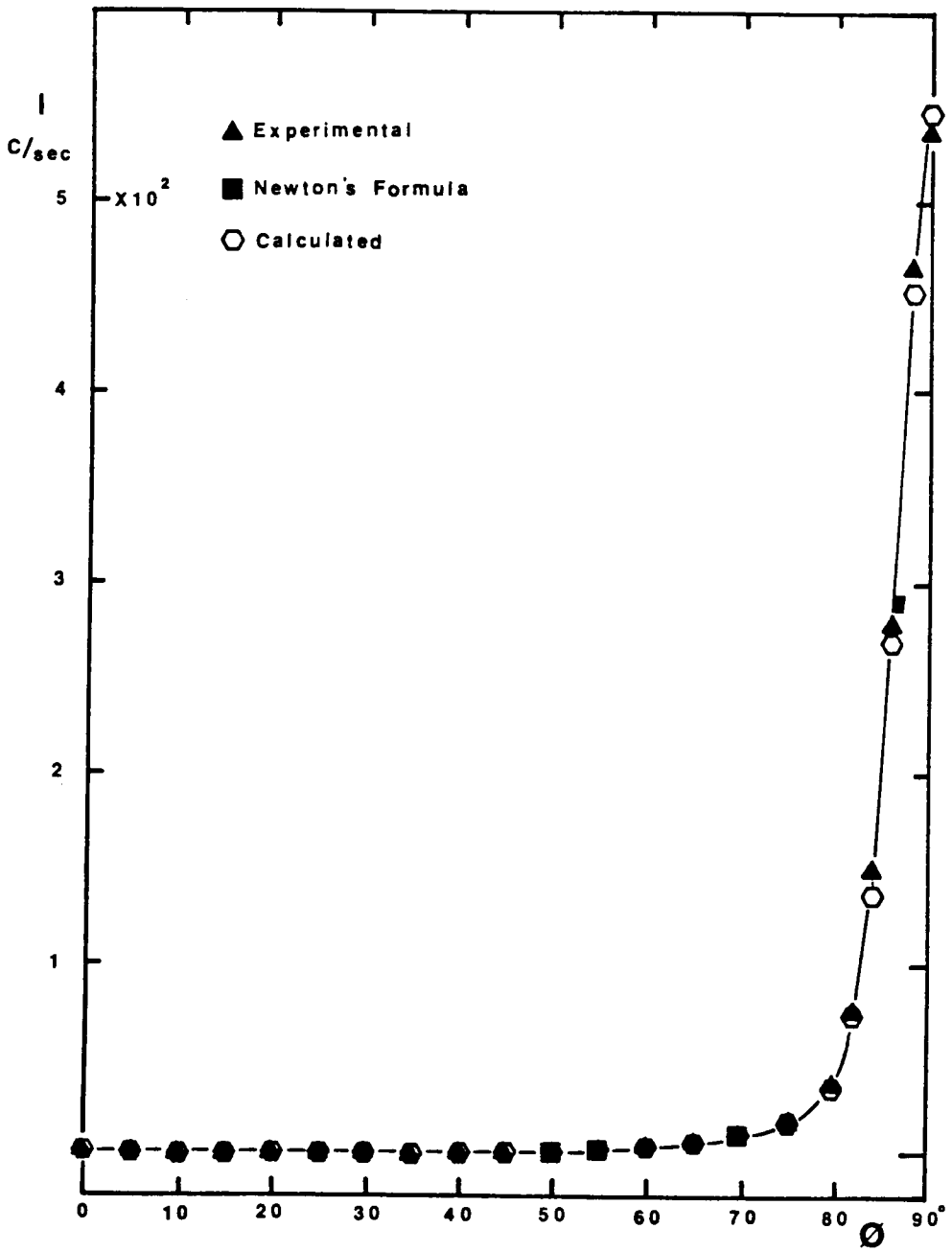

Figure V-18. Kevlar 49 fully corrected intensity curves for the (200) plane poles as a function of the azimuthal angle ϕ (experimental and calculated values from the Norelco diffractometer).

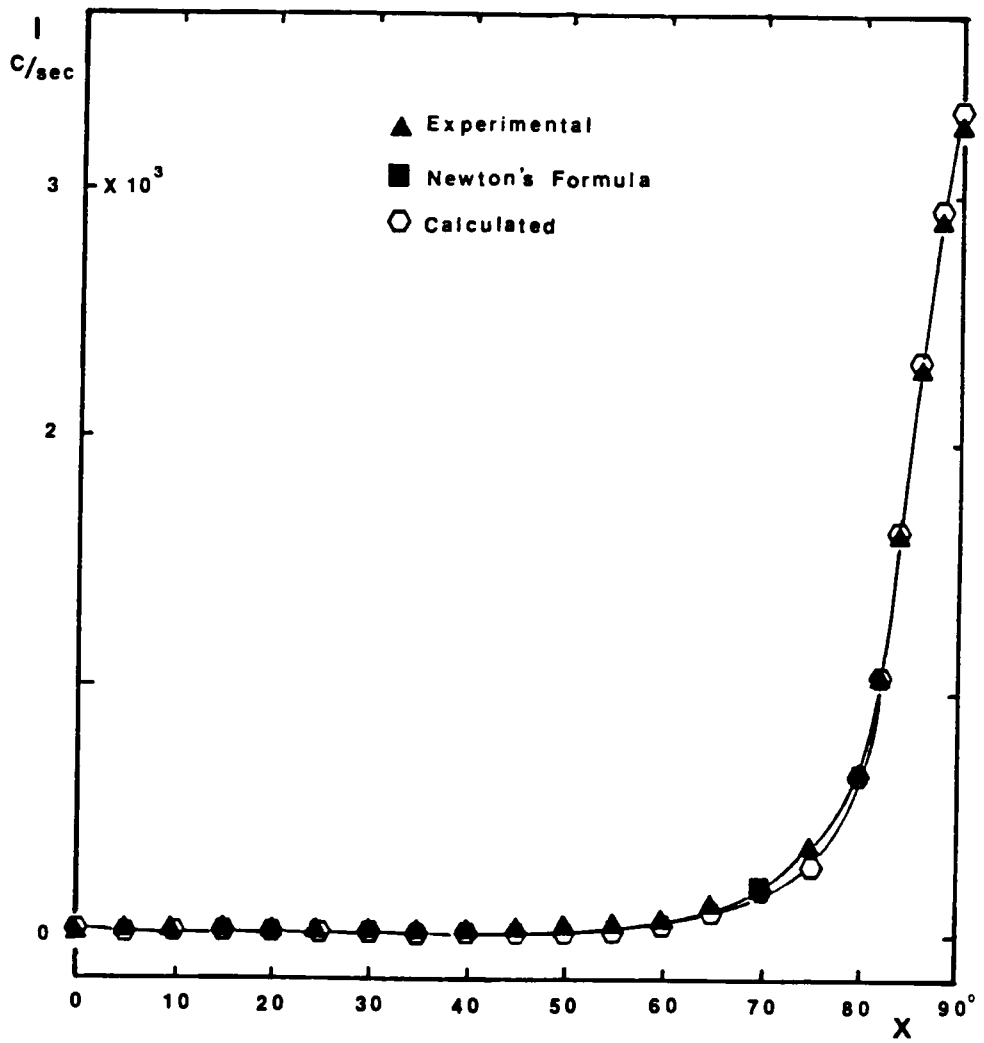

Figure V-19. Kevlar 49 fully corrected intensity curves for the (110) plane poles as a function of the azimuthal angle χ (experimental and calculated values for the Single Crystal Orienter).

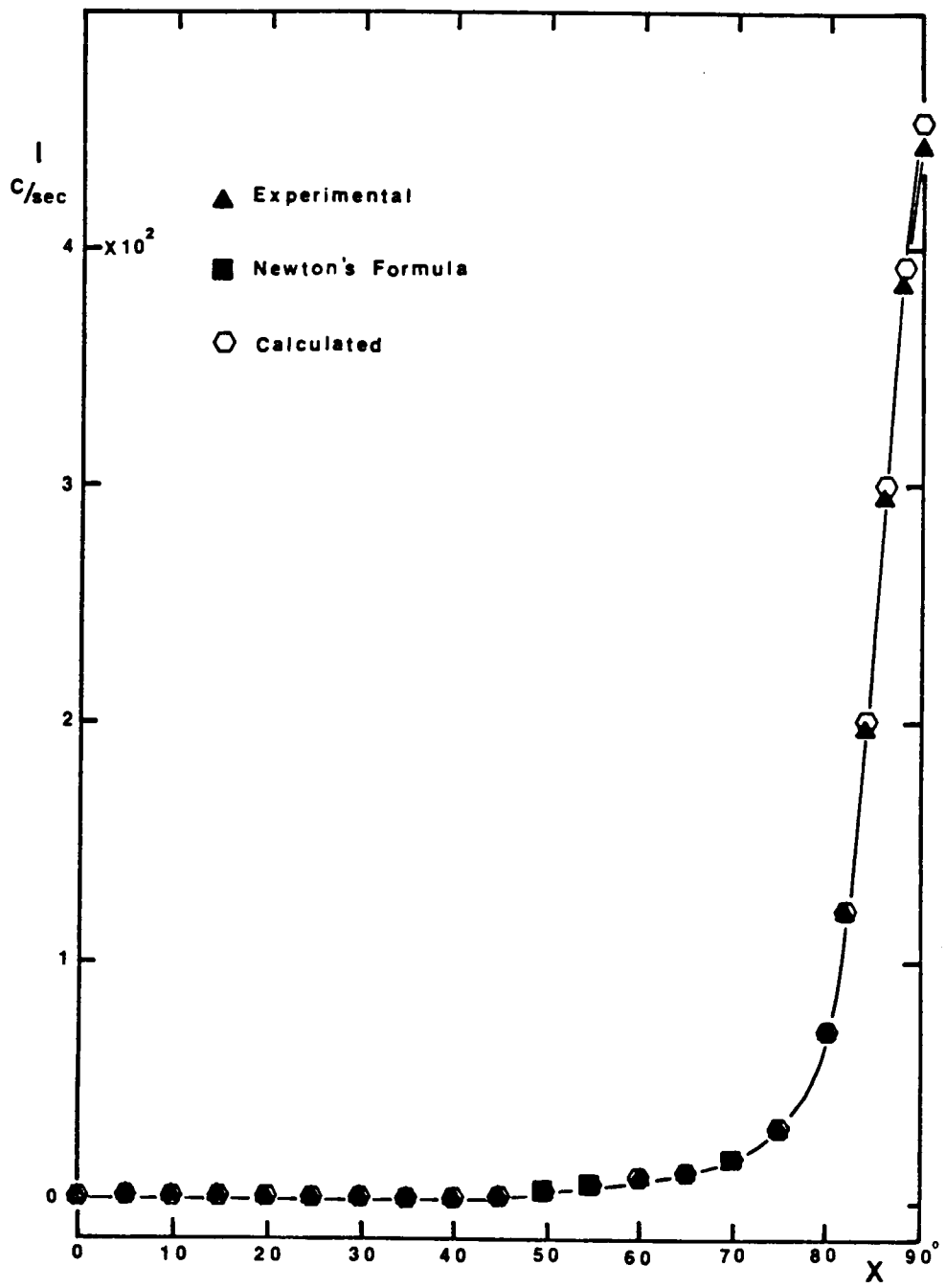

Figure V-20. Kevlar 49 fully corrected intensity curves for the (200) plane poles as a function of the azimuthal angle χ (experimental and calculated values for the Single Crystal Orienter).

show the respective plots for the two main equatorial reflections of Kevlar 49 obtained in each apparatus.

Finally, Herman-Stein orientaiton functions were determined and the results compared with those of the fiber standard given in Table V-6 (p. 129). All results are summarized in Table V-8.

D. DISCUSSION OF RESULTS

X-Ray Linear Absorption Coefficient Measurements

Results reported on these measurements showed an excellent linear behavior for both the unfilled and fiber filled matrix. Although only one determination was carried out in the fiber standard for μ_F, the special characteristics of our standard should be emphasized because of the procedure followed in its preparation. Instead of the traditional fiber standard whose thickness depends on the pressure exerted on it due to the empty space between layers caused by the samll frame used, our fiber standard is more like a fiber-slab, very handly and uniform. No distortions are introduced because of the winding procedure as probably occurs in a small frame, and the fiber patterns obtained show noticeable improvement when compared to those obtained from the same material prepared in the traditional manner. However, the proposed procedure requires a much larger amount of fiber than the standard

Table V-8

Cosine Squared Values and Orientation Functions for Kevlar 49 Fibers: Results from the Fiber and Composite Standard

Function	Norelco Diffractometer	Single Crystal Orienter
	Fiber Standard	Fiber Standard
$\overline{\cos^2\phi_{110,z}}$	0.0178	0.0273
$\overline{\cos^2\phi_{200,z}}$	0.0143	0.0232
$\overline{\cos^2\phi_{c,z}}$	0.9664	0.9478
f_c	0.950	0.922
	Composite Standard	Composite Standard
$\overline{\cos^2\phi_{110,z}}$	0.0152	0.0226
$\overline{\cos^2\phi_{200,z}}$	0.0124	0.0221
$\overline{\cos^2\phi_{c,z}}$	0.9712	0.9551
f_c	0.957	0.933

method but it is worth it when fiber supply is not a problem.

Fiber Characterization

A detailed and careful analysis was carried out on the fiber standard to determine and explain the nature of the reflections found within the 2θ range selected as more suitable for background calculations. Interferences were identified and the angle settings (2θ and ϕ) recorded in order to avoid taking intensity data at this angular values. The intensity curves obtained reflect this effort and clearly show the influence of equipment characteristics as noted in the fiber intensity curves from the Single Crystal Orienter, Figures V-14 and V-15 (pp. 125, 126) where a slight broadening is observed as compared to those from the Norelco diffractometer, Figures V-12 and V-13 (pp. 123, 124).

The fiber orientation functions calculated in both x-ray apparatus, as described in Section B, are reproducible and can be used with confidence. The differences observed in the magnitude of these functions are due to instrumental effects such as peak broadening, which arise due to the differences in the geometrical arrangement of the x-ray equipment used.

Composite Standard Characterization

The procedure proposed in Chapter III to determine the amorphous contribution to background in a short-crystalline-fiber filled amorphous-plastic is by no means a unique approach. It is, however, an attempt to attack the problem in a practical manner and obtain reliable enough results so as to use the approach in routine work.

The assumptions made in the derivation of Equation III-30 have given very reasonable results as can be seen from the calculated intensity data plotted in Figures V-17 through V-20. The calculated orientation functions reported on Table V-8 agree very well for the Norelco diffractometer. However, the results from the Single Crystal Orienter show the effect of lower resolution and peak broadening upon the intensity calculation as compared to those of the Norelco equipment. In spite of this, the agreement between experimental and calculated fiber orientation function in the Single Crystal Orienter is considered good.

In evaluating Herman-Stein orientation functions, Equation II-27 shows that all correction factors multiplying the recorded intensities cancel each other during the averaging procedure to obtain the mean-squared consines, and therefore they can be deleted. From the expression given for the corrected intensity, Equation III-20, it can be seen that the absorption correction factor and the

Lorentz-Polarization factors can be neglected from the calculations. However, the other terms, involving air correction, intensity fluctuations and cosmic background, do not cancel each other and therefore it is necessary to determine their relative influence in the values of f_c when they are neglected. Cosmic background corrections are too small (less than 1 percent) to produce any effect on the calculations when omitted. The K factor, Equation III-10, varies from 1 to 3 percent and needs to be considered only in very accurate studies or comparative experiments. The air correction is rather large at low angles (more than 10 percent of the recorded intensity) and decreases rapidly with increases of the scattering angle. If neglected, it will produce small effects in the calculated values for the orientation function. Thus, a value of f_c of 0.93 for the fiber standard becomes 0.91 when the air correction is omitted in the Single Crystal Orienter.

Regarding the effect of the corrections in calculating the orientation functions for the composite material, it should be noted that the form of Equation III-30 also allows us to neglect the absorption and Lorentz-Polarization factors. However, the air scattering corrections are large enough to affect notably the calculations involved in Equation III-30, and thus the results for the orientation functions of composite materials. The derivation of Equation III-30 is based in the corrected intensities from

each component and although many of the corrections can be neglected, this should be done only after a careful evaluation of the effects in the resulting intensity values for the fibers. Equation III-30 is the critical relationship that allows us to account for the rather large amorphous contribution to the total recorded intensity, ranging from 8 to 80 percent in the composite standard as a function of ϕ, and thus the use of corrections is highly recommended. Differences of 20 percent or more can be expected in the calculated intensities of the fibers as compared to the experimental values when the corrections are omitted throughout the procedure. In this case, any orientation function calculations will be unreliable.

CHAPTER VI

CHARACTERIZATION OF FIBER ORIENTATION IN THERMOPLASTIC COMPOSITES

A. INTRODUCTION AND PERSPECTIVE

The great commercial importance of fiber reinforced thermoplastics is based on both their advantageous physical properties as compared with the unfilled materials and their economic processing methods. The strong dependence of physical properties on the fiber orientation is a critical parameter which has been the subject of several studies. However, it is the flow induced orientation during processing which remains in the final product, the most important parameter to investigate in order to relate processing conditions and geometry with final physical properties. As pointed out previously, fiber orientation due to flow has been studied by a limited number of researchers in a generally qualitative approach. Therefore, it has been the purpose of this study to carry out a quantitative evaluation of the degree of orientation due to flow of short-crystalline-fibers suspended in an amorphous polymer melt as a result of varying processing conditions and geometry by means of wide angle x-ray diffraction techniques. To achieve this, an experimental procedure was proposed in Chapter III of this study to remove the amorphous matrix

contribution to the diffracted x-ray intensity, thus allowing the determination of the fiber orientation function as a quantitative evaluation of fiber orientation development due to flow. The proposed technique has been already calibrated against a composite standard as described in Chapter V, with encouraging results given the assumptions made in its development. In this chapter, a further step has been taken by applying the technique to actual composite specimens obtained under very well defined conditions for rheologically characterized systems.

B. EXTRUDATES

Two composite systems, as described in Table III-2 (p. 55), have been considered. All composite and reference amorphous specimens are extrudates and have been prepared in accordance to the procedures given in Chapter III.

Scanning Electron Microscope (SEM) Technique

Specimens for scanning electron microscopy were prepared following the procedure described in Chapter III. Results are shown in Figures VI-1 and VI-2 for the specimens prepared with commercial Kevlar 49 staple fiber. In all the photographs, the central portion of the cross section shows a high degree of fiber disorder with many of the fibers being longitudinally sectioned or having elliptical cross sections. On the other hand, the remaining area around this central portion shows a great proportion of

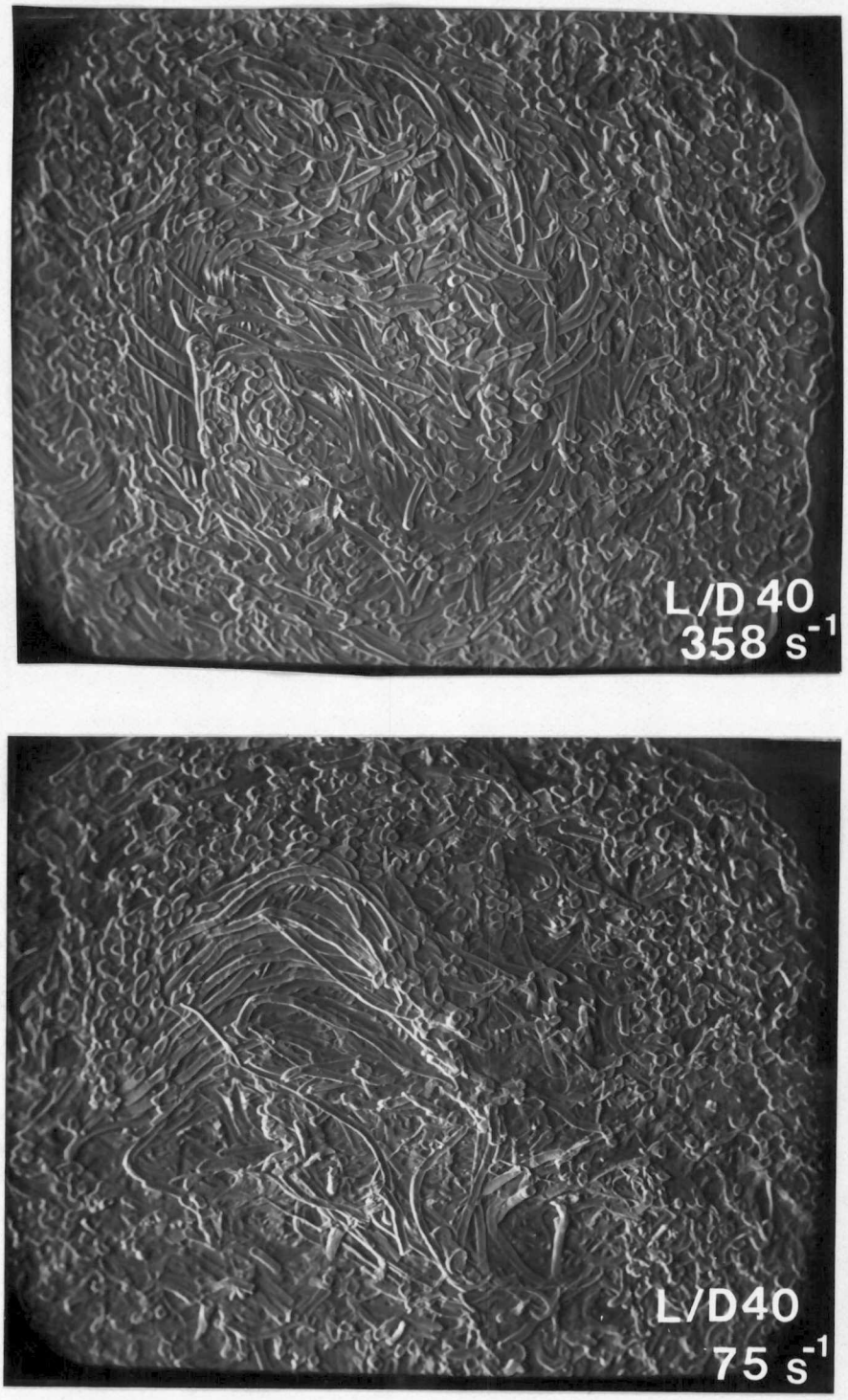

Figure VI-1. SEM photographs of composite samples reinforced with commercial staple fiber (cross section of extrudate samples at different shear rates).

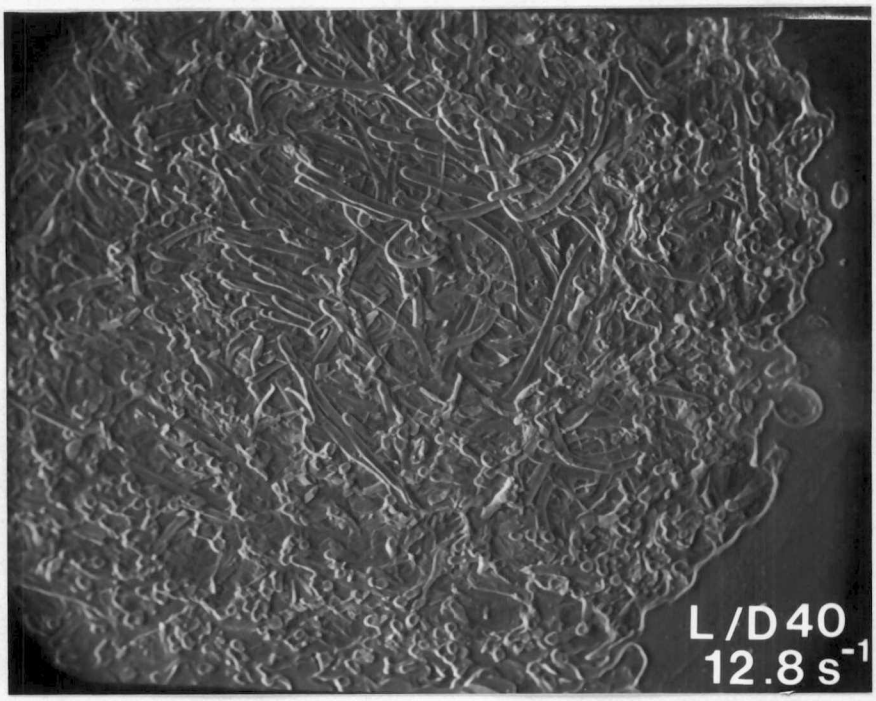

Figure VI-2. SEM photograph of composite sample reinforced with commercial staple fiber (cross section of extrudate sample).

fiber alignment (circular fiber cross sections are clearly observed) which seems to vary with the sample (different shear rate or different L/D ratio), although no final conclusion regarding this observation can be reached from these photographs.

Figures VI-3 and VI-4 show the SEM photographs of representative composite specimens prepared with the short Kevlar 49 fibers from the continuous yarn, corresponding to the x-ray photographs given in Figure VI-5. In these photographs, the fiber distribution is more homogeneous. There are fibers longitudinally sectioned or misaligned, but they are distributed all over the cross sectional area of each specimen. The overall proportion of aligned fibers seems larger to the eye than that observed in the other composite samples and, in fact, accounts for the differences in orientation observed in the x-ray photographs of both composite systems.

X-Ray Flat-Film Photographs

This technique was intended as a first source of qualitative information regarding the fiber orientation development due to flow in processed composite samples. X-ray flat-film photographs of extrudate composite samples prepared from the system reinforced with commercial Kevlar 49 staple fiber are shown in Figure VI-5. Although representative results are shown only for the longer die length (L/D = 40) at three different shear rates, the actual

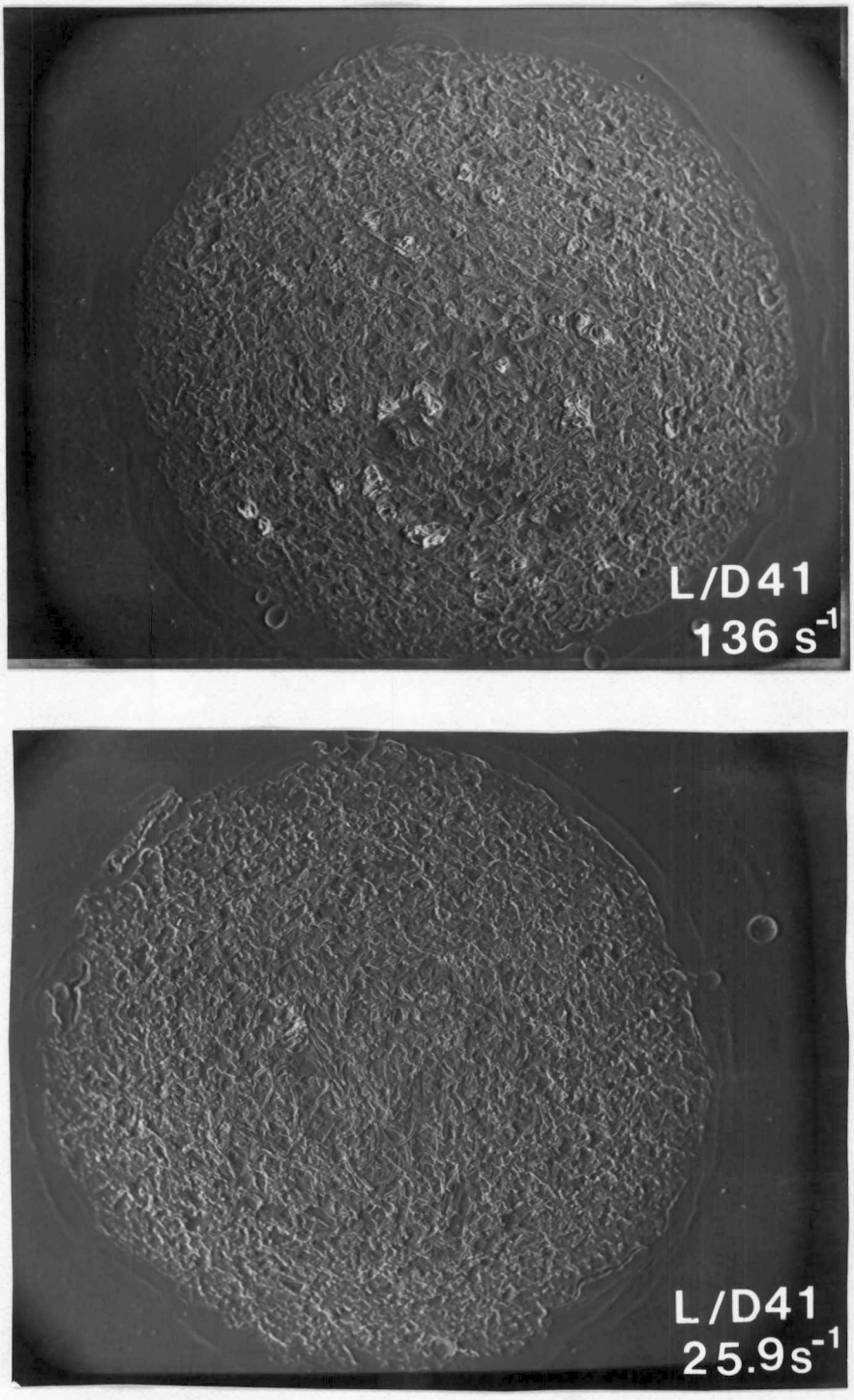

Figure VI-3. SEM photographs of composite samples reinforced with short fibers from the yarn (cross section of extrudate samples at different shear rates).

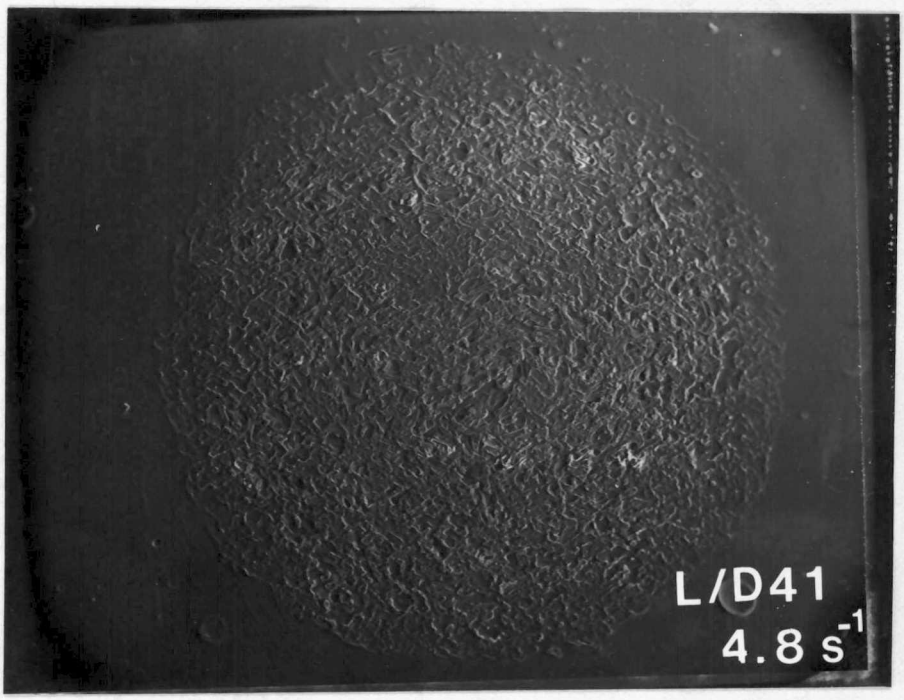

Figure VI-4. SEM photograph of composite sample reinforced with short fibers from the yarn (cross section of extrudate sample).

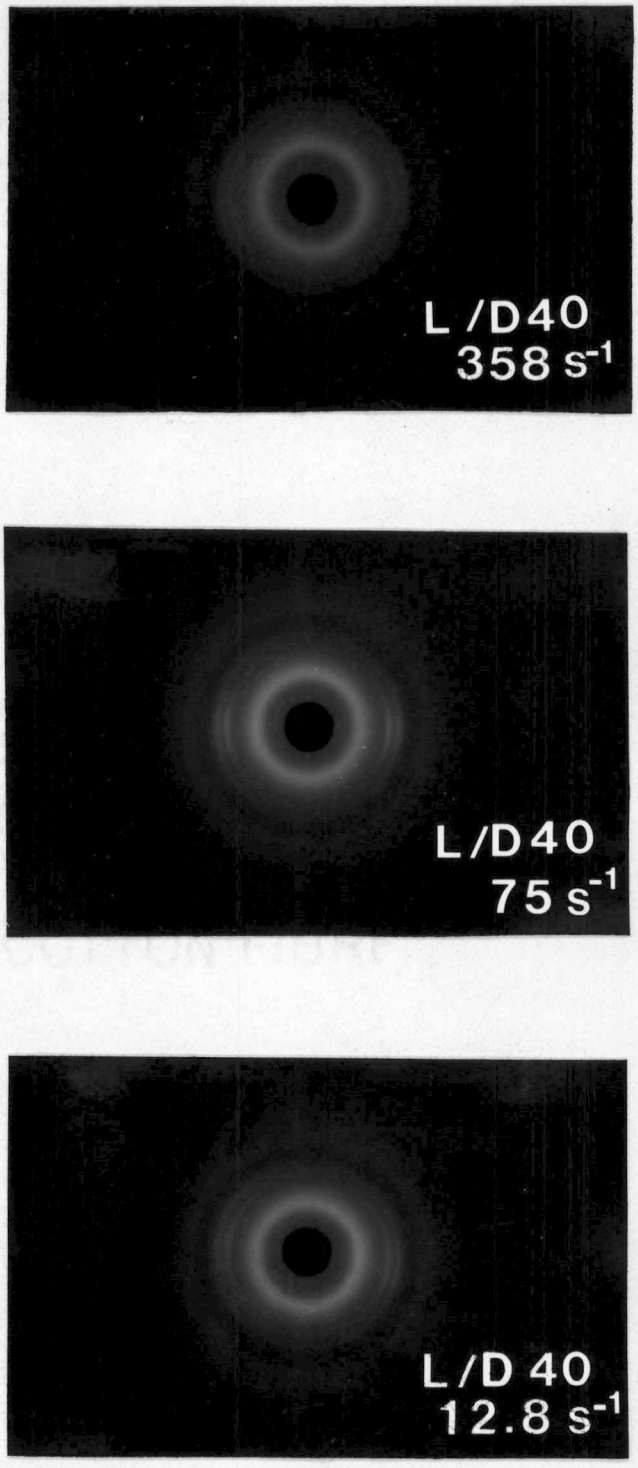

Figure VI-5. X-ray flat-film photographs of composite samples reinforced with commercial staple fiber (extrudate samples at different shear rates).

studies were carried out using three different die lengths at five different shear rates. However, there is little evidence of fiber orientation development in any of the photographs as it was expected for the fiber filled melt under shear flow.

Figure VI-6 shows x-ray flat-film photographs from a set of samples prepared from the composite reinforced with the short Kevlar 49 fibers obtained from the yarn. A slight orientation development can be observed in each of the three photographs which looks a little more developed at the higher shear rate.

Any further interpretation of the results observed in the x-ray photographs above requries additional investigation. SEM techniques are then applied to obtain an actual image of the fiber distribution over the cross section of each specimen in an attempt to clarify the unexpected results above.

Orientation Function Determinations

In light of the results obtained in the previous sections, it was decided to carry out orientation function determinations only in the specimens obtained from the short fiber reinforced composite, where some degree of fiber orientation development was detected. In order to obtain the overall fiber orientation distribution for each specimen by the method proposed in Chapter III, it was necessary to use samples having the same diameter as the extrudates

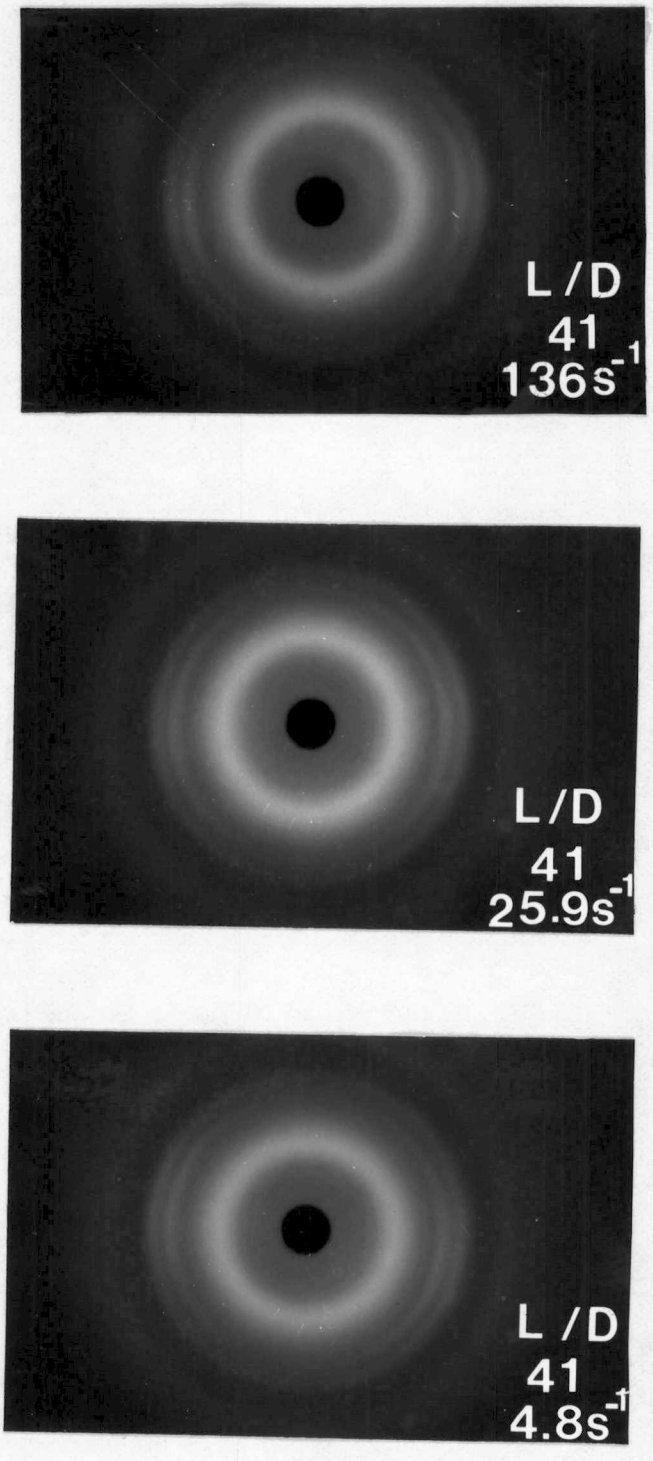

Figure VI-6. X-ray flat-film photographs of composite samples reinforced with the short fibers from the yarn (extrudate samples at different shear rates).

(>2 mm). These sample dimensions require proper absorption corrections which cannot be neglected. Thus, because of these restrictions, it was necessary to use spherical samples which allow carrying out the required corrections when the specimen is totally bathed by the x-ray beam for all the angular positions in the goniometer. This latter condition and the sample size rules out the use of the Norelco diffractometer (small beam dimensions). Therefore, all orientation function determinations in composite samples were carried out in the Single Crystal Orienter, following the steps given in Table V-7 (p. 132) for the composite standard and using the respective value of A_{o}° for spherical samples (53), instead of [exp(-μT)] in Equation III-30. All composite and amorphous reference samples were prepared in accordance to the procedures given in Chapter III.

C. COMPOSITE EXTRUDATES

Figure VI-7 shows the orientation function values f_c for extrudates obtained at different volumetric flow rates in a capillary having a L/D ratio of 41.0 and a diameter of 2.00 mm. Values of f_c are plotted as a function of the shear rate at the capillary wall. Values of f_c are of the order 0.3 to 0.38. We have also plotted the die swell ratio:

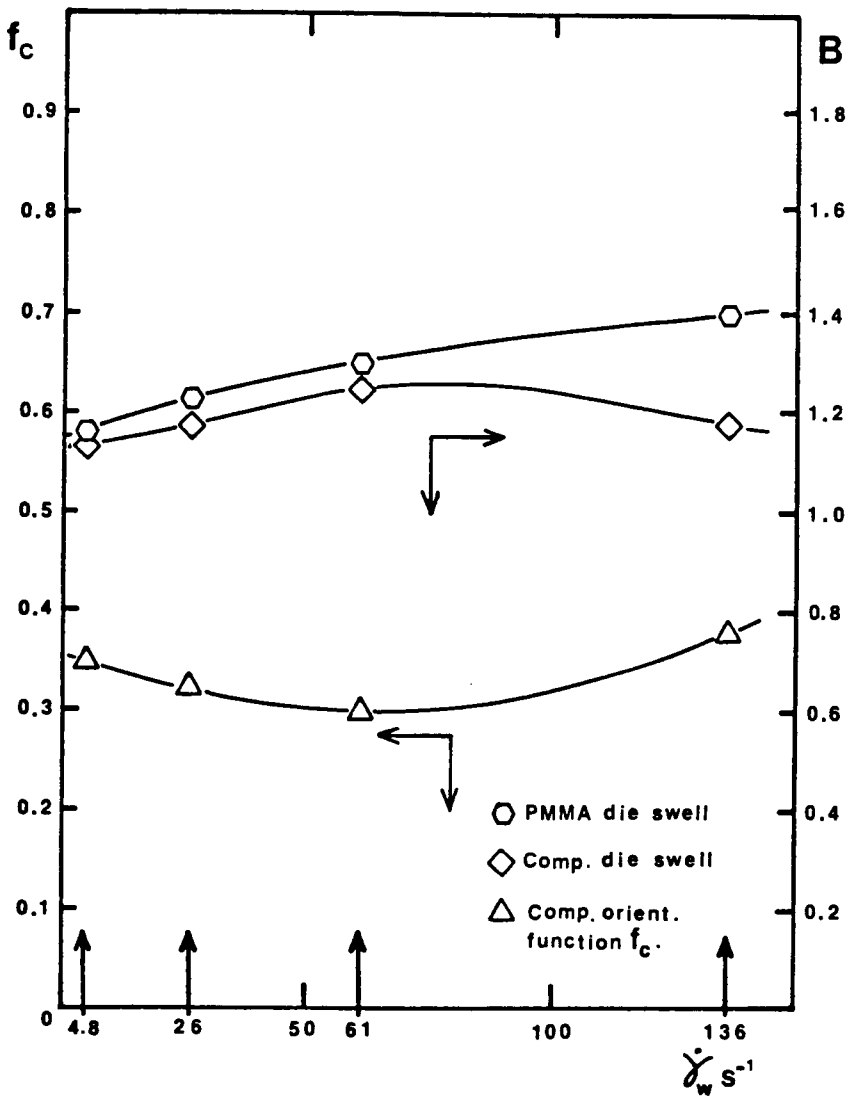

Figure VI-7. Orientation function for extrudate samples as a function of shear rate.

$$B = \frac{d_{ext}}{D_{die}}$$

as a function of the shear rate at the capillary wall. Differences in the value of the orientation function reported in Figure VI-7 are quite small.

D. HISTORY OF A FIBER-FILLED MELT EXTRUDED THROUGH A DIE

The results obtained in the preceding section led to the preparation of another set of samples which were taken from the frozen material remaining inside the capillary die after cooling in order to study the process of fiber orientation development along the length of the die. This study had to be done with a die of L/D = 25.7 (D = 2.00 mm) due to the difficulties in taking the frozen material out of the longer die.

Scanning Electron Microscope (SEM) Technique

Preparation of specimens for SEM analysis was carried out as described in the respective section of Chapter III. The resulting SEM photographs are shown on Figures VI-8 and VI-9. From these photographs, it can be seen that, as already observed with this composite system, the fiber distribution is rather homogeneous all over the cross sectional area having only aligned or misaligned fibers, as those observed in the system reinforced with the commercial staple fiber. There is, however, a clear difference

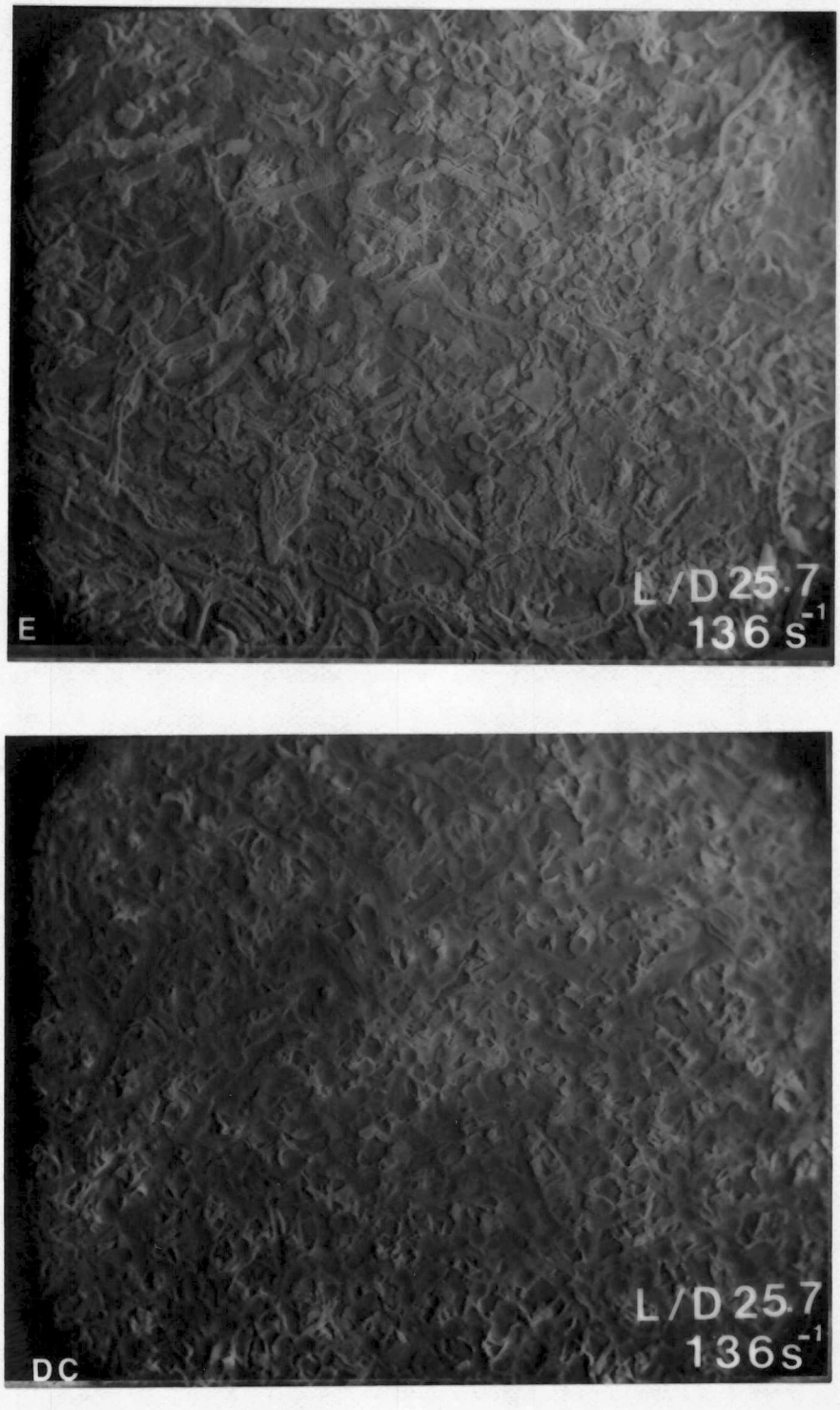

Figure VI-8. SEM photographs of composite samples reinforced with the short fiber from the yarn (samples taken from the frozen material inside the die). DT = Die-Top and DC = Die-Center (cross sections).

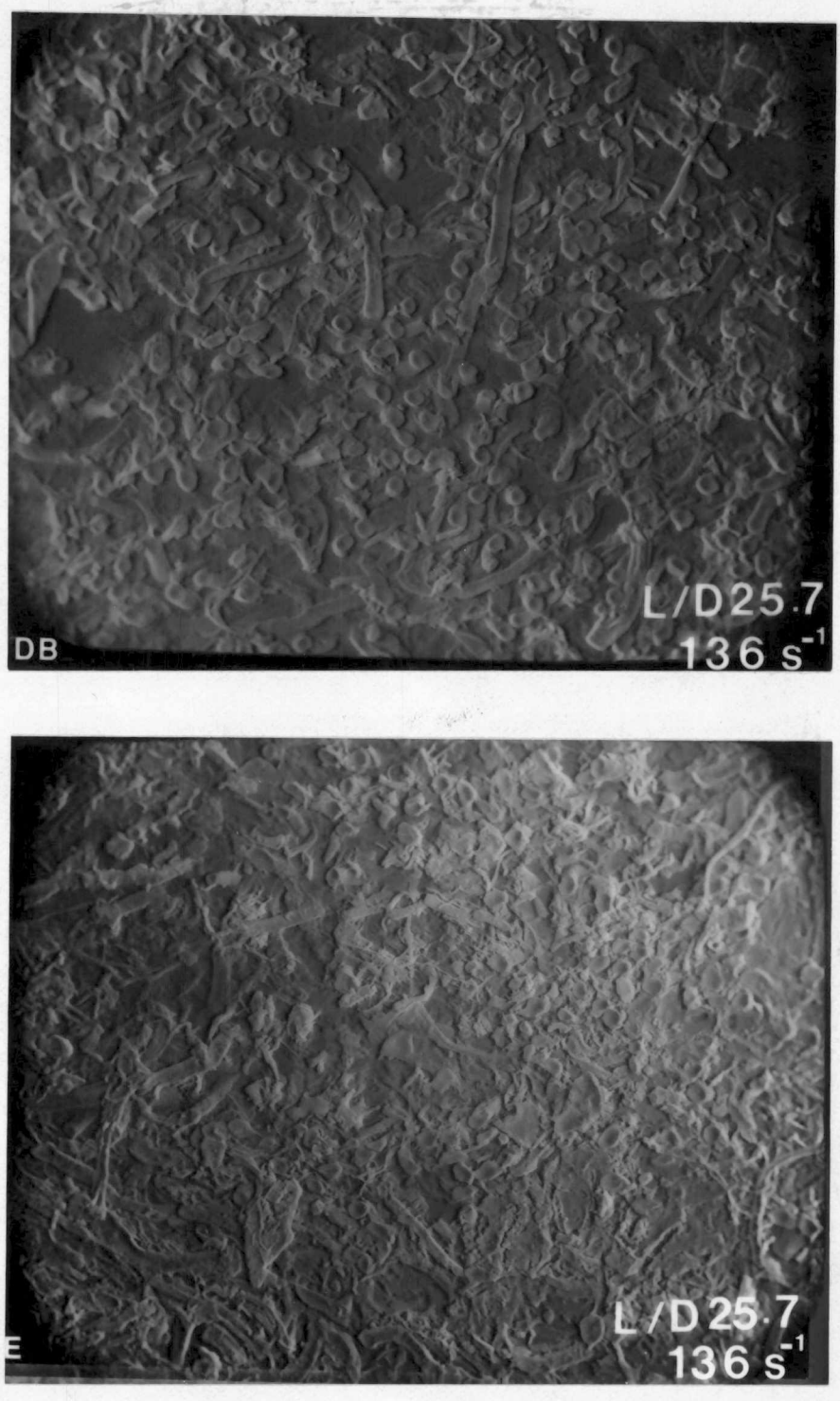

Figure VI-9. SEM photographs of composite samples reinforced with the short fibers from the yarn (sample taken from the frozen material inside the die and extrudate). DB = Die-Bottom and E = Extrudate (cross sections).

between the degree of fiber alignment observed in the samples taken from the material frozen inside the die and that observed in the extrudate sample which accounts for the differences detected in the x-ray photographs.

X-Ray Flat-Film Photographs

X-Ray flat-film photographs of the set of samples taken from the frozen material inside the die are shown in Figures VI-10 and VI-11, along with a sketch of the location of each sample inside the capillary. Although a slightly higher degree of fiber orientation development can be seen in the samples from inside the die as compared to that observed in the extrudate sample, no judgment can be done regarding the change in fiber orientation, if any, along the die length.

Orientation Function Determinations

Figure VI-12 illustrates the fiber orientation development as measured by the orientation function f_c with position along the extrusion process. Samples taken from the rheometer barrel above the die entrance, inside the die at different positions, and from the extrudate material, were analyzed. The frozen material inside the die was carefully extracted and divided into three equal portions, a sample was then prepared from the central part of each portion. Amorphous reference standards were prepared following the same procedure and analyzed. Orientation

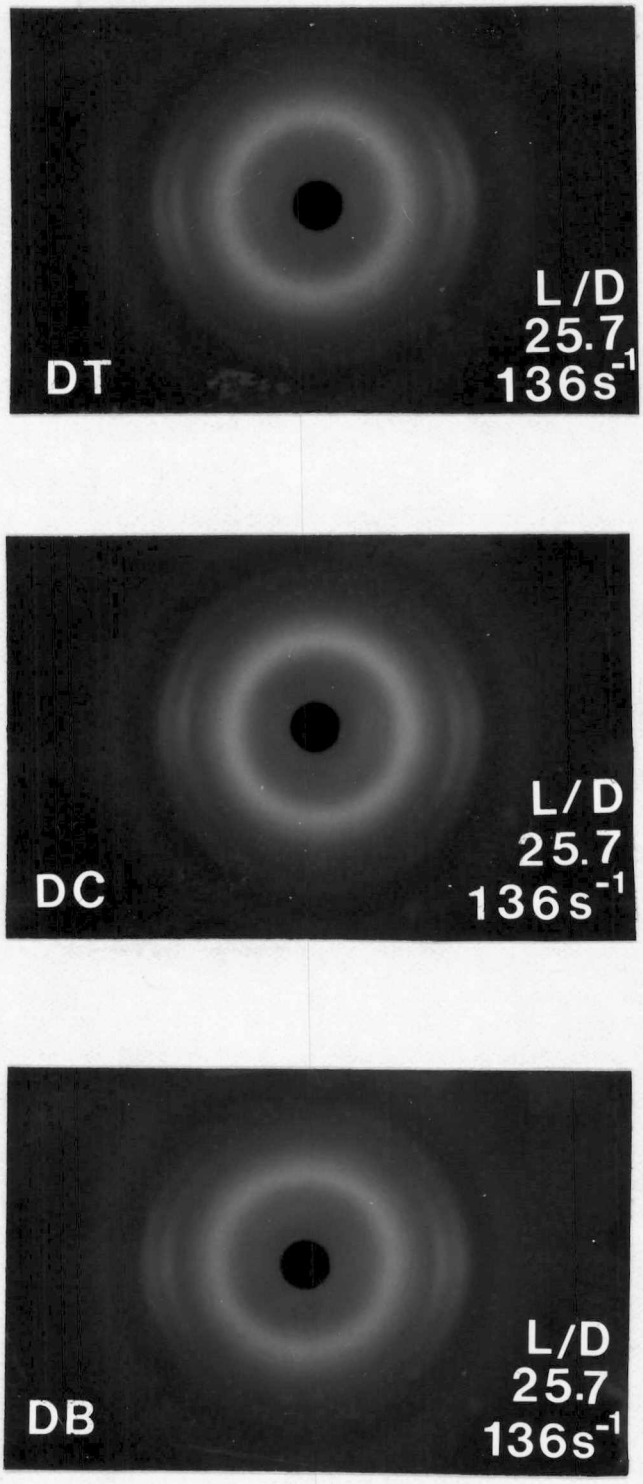

Figure VI-10. X-ray flat-film photographs of composite samples reinforced with the short fibers from the yarn. Samples taken from the frozen material inside the die DT = Die-Top, DC = Die-Center and DB = Die-Bottom.

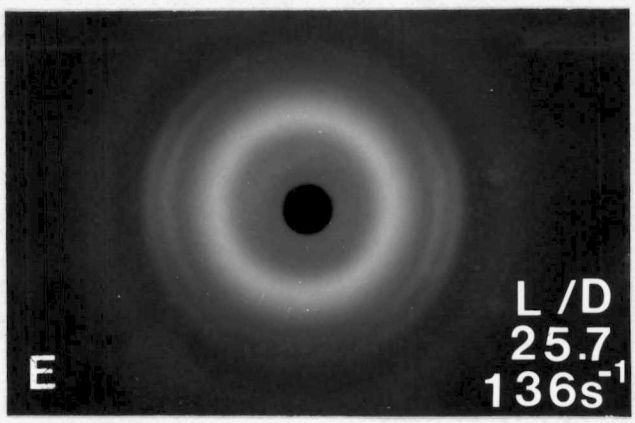

Figure VI-11. X-ray flat-film photographs of composite reinforced with the short fibers from the yarn (extrudate sample).

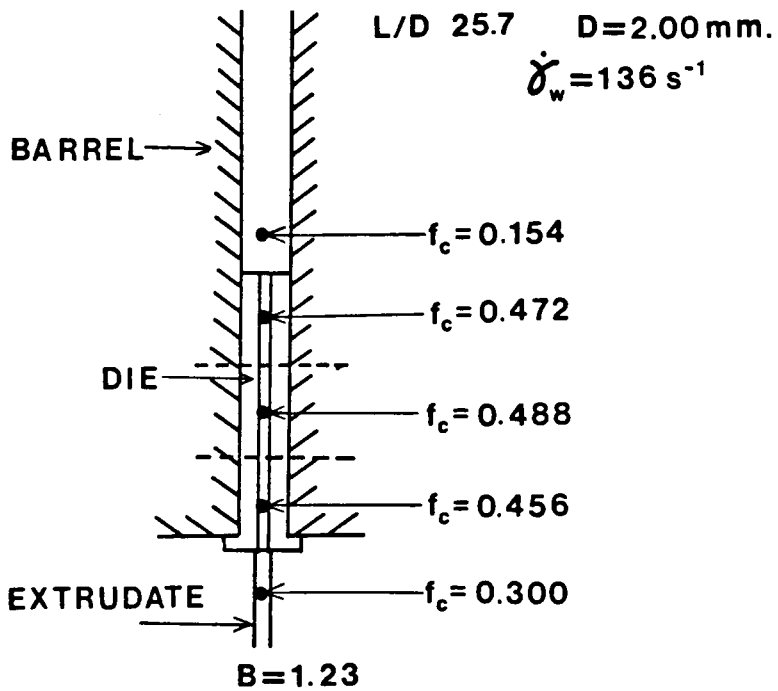

Figure VI-12. Fiber orientation development during the capillary extrusion process.

functions were then calculated using the proposed technique, being the results those given in Figure VI-12. From these results, it is seen that the fiber orientation development takes place along the capillary length and it is somehow reduced by the die swell in the extrudate sample. It should be noted that die swell effects in the composite material are of much less magnitude than those usually found in the unfilled melt. However, they affect the value of the orientation function in the extrudate samples and must be taken into account.

The results observed in the preceeding sections will be discussed below.

D. DISCUSSION OF RESULTS

In order to characterize fiber orientation in composite samples, it was expected to have samples with a high degree of orientation development to work with. However, results from the x-ray photographic analysis in samples prepared from the composite filled with the commerical Kevlar 49 staple fiber were disappointing. Four different capillary lengths and nine different shear rates in the range 0-350 sec^{-1} did not induce any significant fiber orientation development in our samples as we could see from the x-ray photographs. However, a conclusion regarding these results could not be drawn only on the basis of the x-ray results. X-ray photographs are very helpful when the degree of

orientation development is very high. However, very low orientation effects are difficult to be seen in an x-ray photograph. Differences in film blackening due to low orientation effects require careful microdensitometer measurements in the film to be detected. Furthermore, no information regarding the actual fiber distribution in the non-oriented sample can be obtained from the x-ray film. Therefore, the use of SEM techniques complements that of x-ray analysis in the case of very low orientation effects.

SEM results shown in Figures VI-1 and VI-2 (pp. 145 146) for the composite samples reinforced with the commercial staple fiber were very helpful in explaining the results from the x-ray photographic analysis. The fiber disorder observed in the central portion of the SEM photographs from the composite specimens accounts for the absence of orientation effects in the x-ray photographs. To explain the origin of this high degree of fiber disorder, it is necessary to recall three facts of the system being analyzed: first, the composite is reinforced with commercial staple fibers having a modal length of 6.35 mm; second, the diameter of the capillary dies used in our experiments is only 1.47 mm; and third, the melt behavior is highly pseudoplastic as it is seen from its viscosity function reported on Figure IV-2 (p. 86). Therefore, at the die entrance, fibers not aligned in the flow direction will bend as they enter the die producing a high degree

of fiber disorder. Inside the die, the pseudoplastic flow behavior of the melt causes the shear rate to decrease rapidly towards the center of the die, and thus fiber alignment because shear flow takes place only in the proximity of the capillary wall, while the central portion of the flow front is very little affected by the shear field and the bent fibers remain in a high state of disorder.

In the case of the composite system reinforced with the short fibers from the yarn, x-ray photographs showed a low degree of fiber orientation development. This observation was confirmed by the SEM photographic analysis of the samples. For this system, the modal length of the reinforcing fibers is only 1.18 mm, as compared with the 2 mm diameter of the capillary used in our experiments. Thus, fiber bending was not a problem and the SEM photographs showed a rather uniform distribution of aligned and misaligned fibers over the whole cross sectional area of the sample (see Figures VI-3 and VI-4, pp. 148, 149), and there is not a well defined boundary between aligned and disaligned fibers as in samples from the other composite system. Viscosity functions are similar in both systems. Analysis of Figure IV-2 (p. 86) shows a small difference in viscosity favorable to the system being discussed along the shear rate range measured, but a similar pseudoplastic behavior is observed in both systems. Therefore, the difference in the ratio

Fiber length/Capillary diameter

is the principal parameter affecting the results regarding fiber orientation development due to flow in the two composite systems investigated. A fiber length smaller than the capillary diameter allows rotational fiber motion. A kind of motion that has been observed for fibers suspended in a polymer melt (23) under shear flow, which could have affected the fiber orientation development if it occurred in our system reinforced with the small fibers from the yarn.

Orientation function values determined by the proposed procedure in composite samples are reported in Figure VI-7 (p. 154) as a function of the shear rate. Die swell values for the samples are also plotted in the same graph. The change observed in the values of the orientation function with the shear rate does not seem to correlate with each other. However, an analysis of the die swell measured in each sample allows an explanation of the apparent lack of correlation observed and points out the influence of die swell in the values of the calculated orientation functions. Die swell has been reduced by the presence of fibers, as reported by several investigators (14, 23, 107), but it is not eliminated. It seems that the elastic recovery associated with the die swell effect distorts the fiber alignment developed along the capillary die. This effect can be seen on Figure VI-7 (p. 154), where the die swell effect is

reflected on the orientation function curve. However, a judgment of the effect of the die swell alone upon the fiber orientation development cannot be done on the basis of the data reported on Figure VI-7 (p. 154), because of the influence of the shear rate which, therefore, cannot be isolated either. However, points 2 and 4 of the data plotted have practically the same die swell and, being the 40 ratio the same for both, the difference in the value of the orientation function observed in each sample can be attributed only to the shear rate. Thus, increase in shear rate produces an increase in the fiber orientation development, other things being equal.

The effect of die swell on the fiber orientation is clearly established from the results reported on Figure VI-12 (p. 161). A set of five samples taken at different positions along the capillary die together with samples from above the die (Instron barrel) and extrudate. The sample taken from the melt in the rheometer barrel (after cooling) has a low degree of orientation development which can be expected from a sample in the center of the barrel where, given the pseudoplastic flow behavior, shear effects are minimal. The result for the sample taken from the top part inside the die shows a rather large increase in the orientation function value and can be explained by the fiber alignment due to the converging flow at the die entrance. This value increases slightly in the next sample

and shows a decrease towards the end section of the die. However, the differences involved in these three samples are rather small and can be questioned on the basis of the accuracy of the measurements and the assumptions made in the determination of the orientation functions. In favor, we can say that all intensity measurements were carried out with extreme care regarding sample dimension, preparation and mounting; counting statistics; and experimental procedure. The errors due to assumptions made in the background correction procedure should be similar in all three samples and thus, the relative differences observed, although small, should be caused by the flow inside the capillary. Therefore, the small increase and following decrease in the value of the orientation function for samples 3 and 4 inside the capillary should be effects of the shear flow and need to be explained. A possible interpretation of this fluctuation in fiber orientation development along the capillary length could be given in light of the qualitative observations of Crowson, Folkes and Bright (23) on capillary flow of glass-fiber filled polypropylene melts. Using the contact microradiography (CMR) technique in frozen samples taken out of the capillary die, they found that the high degree of fiber alignment due to convergent flow at the die entrance is reduced by subsequent shear flow along the capillary die, the effect being more pronounced at low flow rates than at high flow rates. In

our samples, it could be considered that the fiber alignment at the die entrance due to convergent flow is slightly enhanced by the development of shear flow inside the die which further align the fibers in the direction of flow. However, as the fully developed flow front travels towards the die exit, the effects of the shear field tend to reduce the fiber alignment as found by Crowson et al. This shear related effect might be the observed rotational motion induced on the fibers by the shear field and reported by Crowson and coworkers.

Analysis of an extrudate sample confirmed the effect of die swell on the value of the orientation function. A rather high decrease is observed in the degree of fiber orientation distribution, as given by the orientation function, which can be undoubtedly related to the die swell.

Although the experimental data presented for discussion have been limited, some relevant conclusions can be made regarding the development and measurement of fiber orientation development due to flow in capillary extrusion experiments. Four basic parameters should be considered regarding the determination of fiber orientation functions in extrudate samples of short fiber-filled melts, as follows:

1. Ratio of fiber length to capillary diameter
2. L/D ratio for the capillary

3. Shear rate

4. Die swell.

Each effect can be isolated in actual experimental work and, thus, a better understanding of the influence of each one upon the fiber orientation development process can be obtained in further experimental research. The explanations attempted in this section for the observed results are intended as a first approach, but more experimental data is necessary to confirm, reject or modify the given approaches.

CHAPTER VII

CONCLUSIONS AND RECOMMENDATIONS

A. CONCLUSIONS

Studies of both rheological properties and fiber orientation development due to flow of two thermoplastic composite systems are described. These systems are mechanical mixtures of an amorphous polymethylmethacrylate (PMMA) matrix with short crystalline aramid (Kevlar 49) reinforcing fibers in a proportion 80/20 in volume. As rheological properties, only shear viscosity (η) could be measured because of experimental difficulties or flow instabilities. The fiber orientation development due to flow was quantitatively characterized by means of Herman-Stein orientation functions in extrudate and frozen in situ specimens by using a wide angle x-ray technique proposed in this research.

The main results are:

(1) Addition of aramid fibers with diameters of 12 μm results in an increase in viscosity, but does not modify the basic character of the viscosity shear rate behavior of the polymer melt.

(2) There is little change in viscosity with fiber length at high rates of deformation, but significant

increments in viscosity can be expected at lower shear rates with longer fiber length distributions.

(3) In the system where the fiber length exceeded the die diameter pressure fluctuations occurred during flow, and a core-skin effect was observed in all of the extrudate samples analyzed,

(4) Fiber length larger than die diameter is found to affect the linearity of the Bagley plot (ΔP versus L/D) used to correct for end effects in capillary flow.

(5) A wide angle x-ray technique is proposed to determine the amorphous matrix contribution to the total diffracted intensity. This technique has been calibrated against a standard composite specimen with good results for two different x-ray diffractometers.

(6) Orientation functions determined in composite specimens prepared by capillary extrusion are dependent on both shear rate and die swell.

(7) Fiber orientation development in processing is found to take place inside the capillary die and is affected by the exiting of the extrudate. This is so in spite of the reduced die swell effect observed in the filled material as compared to that occurring in the pure melt.

B. RECOMMENDATIONS

The following recommendations for future study of the fiber orientation development due to flow in short crystalline-fiber filled amorphous-plastics under varying processing conditions and geometry are made:

(1) Experimental studies on composite systems with different fiber content and fiber aspect ratio should be carried out in order to obtain a better understanding of the effect that these parameters have upon both the rheological behavior of the system and the fiber orientation developed under varying processing conditions and geometry.

(2) Experimental studies regarding the application of proposed technique to determine biaxial orientation functions in composite specimens processed by injection molding, biaxial extension, and similar processes should be attempted. The new x-ray equipment available will allow further exploration of the possibilities of the proposed technique in these more complex processes with the advantages of high resolution and automation.

(3) Finally, it is up to the investigator to decide whether the procedure proposed to determine the amorphous contribution to background should be carried out as indicated or it could be simplified regarding the characteristics of both specimen and x-ray equipment.

LIST OF REFERENCES

LIST OF REFERENCES

1. Alexander, L. A., "X-Ray Diffraction Methods in Polymer Science," Wiley Interscience, New York (1969).

2. Bagley, E. B., J. Appl. Physics, 28, 624 (1957).

3. Bagley, E. B., Trans. Soc. Rheol., 5, 355 (1961).

4. Bark, F. H. and H. Tinoco, J. Fluid Mech., 87, 321 (1978).

5. Batchelor, G. D., J. Fluid Mech., 46, 813 (1971).

6. Bell, J. P., J. Comp. Mat., 3, 244 (1969).

7. Bowyer, W. H. and M. G. Bader, J. Mat. Sci., 7, 1315 (1972).

8. Brody, H. and I. M. Ward, Polym. Eng. Sci., 11, 139 (1971).

9. Brunn, P., J. Fluid Mech., 82, 529 (1977).

10. Casale, A., R. C. Penwell and R. S. Porter, Rheol. Acta, 10, 412 (1971).

11. Cessna, L. C., Jr., U. S. Patent 3,651,187 (1969).

12. Cessna, L. C., Jr., 28th ANTEC of the S. P. E., Section 25, 527 (1970).

13. Cessna, L. C., Jr., J. B. Thomson and R. D. Hanna, S. P. E. Journal, 25, 35 (1969).

14. Chan, Y., J. L. White and Y. Oyanagi, J. Rheology, 22, 507 (1978).

15. Charrier, J. M. and J. M. Rieger, Fiber Sci. Technol., 7, 161 (1974).

16. Chen, P. E., Polym. Eng. Sci., 11, 1, 51 (1961).

17. Coleman, B. D. and W. Noll, Rev. Mod. Phys., 33, 239 (1961).

18. Coleman, B. D. and H. Markowitz, J. Appl. Phys., 35, 1 (1964).

19. Coleman, B. D., H. Markowitz and W. Noll, "Viscoelastic Flow of Non-Newtonian Fluid," Springer Verlag, New York (1966).

20. Coran, A. Y., P. Hamed and L. A. Goettler, Rubber Chem. Technol., 49, 1167 (1976).

21. Cox, H. L., Brit. J. Appl. Phys., 3, 72 (1952).

22. Crowson, R. J. and M. J. Folkes, Polym. Eng. Sci., 20, 934 (1980).

23. Crowson, R. J., M. J. Folkes and P. V. Bright, Polym. Eng. Sci., 20, 925 (1980).

24. Czarnecki, L. and J. L. White, J. Appl. Polym. Sci., 25, 1217 (1980).

25. Darlington, M. W. and P. L. McGinley, J. Mat. Sci., 10, 906 (1975).

26. Davis, J. H., Plastics and Polym., 39, 140 (1971).

27. Donald, H. J., U. S. Patent 3,279,501 (1966).

28. Duvdevani, I. and I. Klein, S. P. E. 13th ANTEC, Tech. Papers, p. 445 (1967).

29. Eisenschitz, R., B. Rabinowitsch and K. Weissenberg, Mitt. Dtsch. Materialpruefungsanst, Sonderh, 9, 91 (1929).

30. Einsten, A., Ann. der Phys., 19, 289 (1906).

31. Endo, H., T. Fujimoto and M. Magasawa, J. Polym. Sci., A-2, 9, 345 (1971).

32. Engstrom, A., "Physical Techniques in Biological Research," Vol. 3, Academic Press, New York (1956).

33. Ergun, S., "Chemistry and Physics of Carbon," Vol. 3, Marcel Deckker, New York (1968).

34. Ferry, J. D., "Viscoelastic Properties of Polymers," Wiley, New York (1966).

35. Forgacs, O. L. and S. G. Mason, J. Colloid Sci., 14, 457, 473 (1959).

36. Fox, T. G. and P. J. Flory, J. Amer. Chem. Soc., 70, 2384 (1948).

37. Fox, T. G. and P. J. Flory, J. Phys. Chem., 21, 581 (1950).

38. Gauthier, F., H. L. Goldsmith and S. G. Mason, Rheol. Acra., 10, 344 (1970).

39. Goddard, J. D., J. Non-Newt. Fluid Mech., 1, 1 (1976).

40. Goddard, J. D., J. Fluid Mech., 78, 177 (1976).

41. Goddard, J. D., J. Rheology, 22, 615 (1978).

42. Goettler, L. A., Soc. Plastic Ind., 25th Annual Tech. Conf. Reinf. Plast. Section 14A, 1 (1970).

43. Goettler, L. A., Modern Plastics, 140 April (1970).

44. Goettler, L. A. and A. J. Lambright, U. S. Patent 4,057,591 (1977).

45. Goettler, L. A. and A. J. Lambright, U. S. Patent 4,057,610 (1977).

46. Goldsmith, H. L. and S. G. Mason, Trans. Soc. Rheol., 10, 571 (1966).

47. Graesley, W. W. and L. Segal, AICHE J., 16, 261 (1970).

48. Han, C. D., J. Appl. Polym. Sci., 18, 821 (1974).

49. Henry, N. F. M., H. Lipson and W. A. Wooster, "The INterpretation of X-Ray Diffraction Photographs," McMillan and Co., Ltd., London (1960).

50. Hermans, P. H. and P. Platzek, Kolloid Z., 88, 68 (1939).

51. Hermans, J. J., P. H. Hermans, D. Vermaas and A. Weidinger, Rec. Tran. Chem., 65, 427 (1946).

52. Hermans, J. J., P. H. Hermans, D. Vermaas and A. Weidinger, J. Polym. Sci., 3, 1 (1947).

53. International Tables for X-Ray Crystallography,, Vol. II, Kynock Press, Birmingham, England (1963).

54. Jeffery, G. B., Proc. Roy. Soc., A-102, 161 (1922).

55. Kakudo, M. and N. Kasai, "X-Ray Diffraction by Polymers," Kodansha Ltd., Tokio (1972).

56. Karnis, A. and S. G. Mason, Trans. Soc. Rheol., 10, 571 (1966).

57. Kawai, H., Proc. 5th Int. Rheol. Cong., 1, 97 (1969).

58. Kelly, A., "Strong Solids," Oxford University Press (1973).

59. Kerber, M. L., M. S. Akutin, M. Ya Valetskaya, T. P. Krawchenko and V. S. Tkacheva, translater from Mekhanika Polimeror, No. 2, 231 (1978).

60. Kimura, I., M. Kagiyama, S. Nomura and H. Kawai, J. Polym. Sci., 7, 709 (1969).

61. Klug, H. P. and L. E. Alexander, "X-Ray Diffraction Procedures," Wiley-Interscience, New York (1974).

62. Knutsson, B. A., J. L. White and K. A. Abbas, J. Appl. Polym. Sci., 26, 2347 (1981).

63. Krigbaum, W. R. and R. J. Roe, J. Chem. Phys., 41, 737 (1965).

64. Leal, L. G., J. Fluid Mech., 69, 305 (1975).

65. Leal, L. G., J. Non-Newt. Fluid Mech., 5, 133 (1979).

66. Lee, W. K. and W. H. George, Polym. Eng. Sci., 18, 146 (1978).

67. Lee, B. L. and J. L. White, Trans. Soc. Rheol., 18, 467 (1974).

68. Loveless, H. S. and D. E. McWilliams, Polym. Eng. Sci., 10, 3, 139 (1970).

69. McBrierty and I. M. Ward, Brit. J. Appl. Phys., 1, 1529 (1968).

70. McLuckie, C. and M. G. Rogers, J. Appl. Polym. Sci., 13, 1049 (1969).

71. Maschmeyer, R. O. and C. T. Hill, Adv. Chem. Series, 134, 95 (1974).

72. Maschmeyer, R. O. andC. T. Hill, Trans. Soc. Rheol., 21, 183, 195 (1977).

73. Masuda, T., K. Kitagawa, T. Inoue and S. Onogi, Macromolecules, 3, 116 (1970).

74. Mewis, J. and A. B. Metzner, J. Fluid Mech., 62, 593 (1974).

75. Middleman, S., J. Appl. Polym. Sci., 11, 417 (1967).

76. Minoshima, W., J. L. White and J. S. Spruiell, Polym. Eng. and Sci., 20, 1166 (1980).

77. Moghe, S. R., Rubber Chem. Technol., 47 1074 (1974).

78. Muller, F. H., Kolloid Z., 95 138 (1941).

79. Murty, K. M. and G. F. Modlen, Polym. Eng. Sci., 17, 848 (1977).

80. Nawab, M. A. and S. G. Mason, J. Phys. Chem., 62, 1248 (1958).

81. Nomura, S., H. Kawai, I. Kimura and S. Kagiyama, J. Polym. Sci., 5, 479 (1967).

82. Nomura, S., H. Kawai, J. Kimura and S. Kagiyama, J. Polym. Sci., A-2, 8, 383 (1970).

83. Nomura, S., N. Nakamura and H. Kawai, J. Polym. Sci., A-2, 9, 407 (1971).

84. Northolt, M. G., Europ. Polym. J., 10, 799 (1974).

85. Oda, K., J. L. White and E. S. Clark., Polym. Eng. Sci., 18, 25 (1978).

86. Onogi, S., T. Masuda and K. Kitagawa, Macromolecules, 3, 109 (1970).

87. Owen, M. J., D. H. Thomas and M. S. Found, Modern Plastics, 61, June (1978).

88. Oyanagi, Y. and Y. Yamaguchi, J. Soc. Rheol. Japan, 3, 64 (1975).

89. Patel, P. D., M. S. Thesis, The University of Tennessee, Knoxville (1980).

90. Patel, P. D. and D. C. Bogue, Polym. Eng. Sci., 2, 449 (1981).

91. Penwell, R. C. and R. S. Porter, J. Appl. Polym. Sci., 13, 2427 (1971).

92. Penwell, R. C. and R. S. Porter, J. Polym. Sci., A-2, 9, 463 (1971).

93. Pollet, W. P., J. Appl. Phys., 6, 199 (1955).

94. Ramsteiner, F. and R. Theyson, Composites, 111, April (1979).

95. Roe, R. J., J. Appl. Phys., 36, 2024 (1965).

96. Roe, R. J. and W. R. Krigbaum, J. Appl. Phys., 35, 2215 (1964).

97. Roe, R. J: and W. R. Krigbaum, J. Chem. Phys., 40, 2608 (1964).

98. Sack, R. A., J. Polym. Sci., 54 543 (1961).

99. Samuels, R. J., "Structured Polymer Properties," Wiley-Interscience, New York (1974).

100. Stein, R. S. and F. H. Norris, J. Polym. Sci., 21, 381 (1956).

101. Stein, R. S., J. Polym. Sci., 54, 543 (1961).

102. Stein, R. S., J. Polym. Sci., 31, 335 (1958).

103. Stein, R. S., J. Polym. Sci., 50, 339 (1961).

104. Stephenson, R. C., S. Turner and M. Whale, Composites, 153, July (1979).

105. Taylor, G. R. and S. R. Darin, J. Appl. Phys., 26, 1075 (1955).

106. Thomas, D. P. and R. S. Hagan, paper presented at the 21st Annual Meeting Reinforced Plastics Division of the Society of the Plastics Industry, Chicago (1966).

107. Thomas, D. P. and R. S. Hagan, Polym. Eng. Sci., 9, 164 (1969).

108. Thorton, P. R., "Scanning Electron Microscopy," Chapman and Hall, London (1968).

109. Tobolsky, A. V., "Properties and Structure of Polymers," Wiley, New York (1960).

110. Trevelyan, B. J. and S. G. Mason, J. Colloid Sci., 6, 354 (1952).

111. Vinogradov, G. V. and A. Ya Malkin, S. Polym. Sci., A-2, 4, 135 (1966).

112. Ward, I. M., Proc. Phys. Soc., 80, 1176 (1962).

113. Wegener, W. and K. H. Hausman, Plastrerarbeiter, 21, No. 5, 424 (1970).

114. White, J. L., L. Czarnecki and H. Tanaka, Rubber Chem. Technol., 53, 823 (1980).

115. White, J. L. and L. Czarnecki, J. Rheology, 24, 501 (1980).

116. White, J. L. and J. S. Spruiell, Polym. Eng. Sci., 21, 859 (1981).

117. Wilchinsky, Z. W., J. Appl. Polym. Sci., 7, 923 (1963).

118. Wilchinsky, Z. W., "Advances in X-Ray Analysis," Vol. 6, Plenum Press, New York (1963, p. 231.

119. Wylie, C. R. "Advanced Engineering Mathematics," McCraw-Hill, New York (1975), p. 119.

120. Yoshida, K., G. Budinam, Y. Okayama and T. Kitao, Sen-i-Gakkaishi, 31, T-335 (1975).

VITA

The author, Hernán R. Menéndez-Fernández, was born to Hernán R. Menéndez-Ortuno and the former Maricela Fernández-Durlantes in México City, México, on April 5, 1951. He was the second child of three, having an older sister Nora and a younger brother Ruy, who are both currently residing in Merida, Yucatán, México, as are his parents. He attended elementary school in México City, but continued his secondary education in the State of Yucatán, where he graduated from high school in June 1970. He went on to pursue a degree in Chemical Engineering at the University of the State of Yucatán and graduated as a Chemical Engineer in July 1975.

After five years of working in the Lab of Quality Control and New Product Development of Cordemex S. A. de C. U. Special Products Division (vinyl floor covering manufacturers), in September 1980 he came to the United States and entered the graduate program in Polymer Engineering at The University of Tennessee, Knoxville, from which he received his Master of Science degree in December 1982.

He is married to the former Anita Kay Sherrill, formerly of Millington, Tennessee, who is pursuing a Bachelor of Science degree in Nursing at The University of Tennessee, Knoxville.